TUDelft

Delft University of Technology

Particle Manipulation-on-chip
Using programmable hydrodynamic forcing in a closed loop

Kislaya, A.

DOI
10.4233/uuid:352be4dc-76ae-4fa2-945e-17fdae35e714

Publication date
2022

Document Version
Final published version

Citation (APA)
Kislaya, A. (2022). *Particle Manipulation-on-chip: Using programmable hydrodynamic forcing in a closed loop*. [Dissertation (TU Delft), Delft University of Technology]. https://doi.org/10.4233/uuid:352be4dc-76ae-4fa2-945e-17fdae35e714

Important note
To cite this publication, please use the final published version (if applicable).
Please check the document version above.

Particle Manipulation-on-Chip

Using programmable hydrodynamic
forcing in a closed loop

Ankur Kislaya

$\mathbf{u}_{Particle}$

$\mathbf{u}_{\infty}$

2022 | **TU**Delft

PARTICLE MANIPULATION-ON-CHIP

Using programmable hydrodynamic forcing in a closed loop

DISSERTATION

for the purpose of obtaining the degree of doctor
at Delft University of Technology
by the authority of the Rector Magnificus prof.dr.ir. T.H.J.J. van der Hagen
chair of the Board for Doctorates
to be defended publicly on
Friday 22 April 2022 at 12:30 o'clock

by

Ankur KISLAYA
Master of Science in Aerospace Engineering, Delft University of Technology, the Netherlands
born in Ranchi, India.

This dissertation has been approved by the promotors.

Composition of the doctoral committee:

Rector Magnificus	chairperson
Prof. dr. ir. J. Westerweel	Delft University of Technology, promotor
Dr. D. S. W. Tam	Delft University of Technology, promotor

Independent members:

Prof. dr. T. M. Schneider	École polytechnique fédérale de Lausanne
Prof. dr. ir. R.G.H. Lammertink	University of Twente
Prof. dr. ir. J. M. J. den Toonder	Eindhoven University of Technology
Prof. dr. ir. C. R. Kleijn	Delft University of Technology
Ir. P. Veenstra	Shell Technology Centre Amsterdam, other member
Prof. dr. ir. C. Poelma	Delft University of Technology, reserve member

Cover:	designed by Ilse Modder and Ankur Kislaya
Printed by:	GildePrint - Enschede

CONTENTS

SUMMARY

Microfluidics is the study of fluid motion with small volumes (from 1 millilitre down to 1 nanolitre) such as fluid collected with a nasal swab. The small-scale size of the micro-device allows small sample volumes, cost-effective and low-risk analysis for multiple purposes. Portable devices performing laboratory tasks, detecting samples, and chemical/biological research on a small scale is referred to as *lab-on-a-chip*. Various micro-devices have been widely investigated and developed for applications in several fields, stretching from inkjet printing to cell isolation in medical diagnostics to the drug delivery/discovery industry.

Most micro-devices have a fixed design tailored to carry out a specific task or manipulation activity. However, the fundamental ability of the microfluidic devices revolve around trapping, separating, sorting, and assembling particles or cells. Particle manipulation is done in microfluidics with various contact techniques, using micro-channel geometry, and non-contact techniques using laser fields, magnetic fields, acoustic forces, electrical fields, artificial cilia, and hydrodynamic forces.

The non-hydrodynamic methods, such as magnetic fields, acoustic forces, and electric fields, have complex control mechanisms. These control mechanisms rely on closely coupled interactions between physical fields like fluid flow field interaction with the particle properties such as electrical properties, chemical composition, acoustic properties, or refractive index of the particles. Hence, using only hydrodynamic forcing for manipulating and trapping micro-particles is an attractive alternative for non-contact trapping particles.

The goal of the thesis is to design a microfluidic device that has no real channels with physical walls, such as Y-junction or T-junction devices, instead have "virtual channels". These virtual channels are dynamic, flexible and can be used as multi-purpose channels on a single device to integrate various operations into one single chip. In this work, "virtual channels" are generated using hydrodynamic manipulation only. This approach can significantly improve the functionality of a single device by transporting the particle or cell to the desired locations.

Our device uses uniform flow in the flow chamber and three inlets perpendicular to the flow chamber to manipulate particles. These three inlets can inject or extract fluid in the flow chamber to deviate the streamlines. Since the depth-averaged velocity over the channel in a Hele-Shaw cell is irrotational, we use potential flow theory to predict the flow field for manipulating particles. The linearity of the potential flow theory is ideally suited to the fast computation times required by our application. The optimized particle trajectory that has small flow rate bounds and the least variation in the flow rate from the pump is determined *a*

priori using an optimization routine. This optimization routine is called as *a priori* particle manipulation algorithm. Our flow device benefits from the particle path prediction that provides the user an opportunity to integrate multiple functionalities such as trapping, separation, or sorting onto a single device. This approach is also beneficial for rapid prototyping in the early design stage. It allows to explore different micro-channel geometries and determines which one is best suited to a given application.

However, *a priori* particle manipulation algorithm is currently limited as it does not consider aspects such as surface roughness, particle density, and off-center particle position along the channel height. This would lead to errors in the particle trajectory that will accumulate over time, leading to a complete failure of the experiment. Therefore, it is essential to use feedback control schemes and mitigate aspects of the experiment uncertainty to achieve robust and repeatable experiment results for various experiments. With a feedback loop in an experiment, the error in the particle position can be determined with respect to the *a priori* optimized trajectory, and additional flow rates can be given to correct for the error. For this purpose, the performance of a Proportion-Integral-Derivative-based (PID) controller is investigated. The initial PID controller parameters for various experiments are determined using non-linear optimization.

This thesis demonstrates that a flow device with "virtual channels" can be fabricated and employed for diverse applications. Multiple pivotal experiment test cases such as sorting, trapping, separating, joining, and mixing are performed in the microfluidic device to support this claim. The success of these test cases shows the capability of the device for various applications in the field of microfluidics. The PID controller results show that the experimentally determined particle positions are in close agreement with the *a priori* optimized trajectory. The maximum error is on the order of one particle diameter at the end of the manipulation.

In the future, combining hydrodynamic forcing with acoustic/magnetic/electric fields or optical tweezers can make the flow device more versatile. In addition, the microfluidic device can be made smaller, making it more interesting for biological applications such as cell trapping and chemical applications such as droplet coalescence study. Also, adding more inlets would make the system more redundant for two-particle manipulation. Having more inlets will help to establish more stable streamlines. Moreover, a separate optimization can be done to find the optimum location of the inlets and configuration to facilitate the desired particle trajectories.

SAMENVATTING

Microfluïdica is de studie van vloeistofdynamica van kleine volumes (vanaf 1 nanoliter tot 1 milliliter) zoals vloeistof opgevangen met een neusuitstrijkje. De kleinschaligheid van de micro-apparaat maakt het mogelijk om kleine monstervolumes kosteneffectieve en risicoarme analyse uit te voeren voor meerdere doeleinden. Draagbare apparaten die laboratoriumtaken uitvoeren, monsters detecteren, en chemisch/biologisch onderzoek op kleine schaal verrichten worden lab-on-a-chip genoemd. Zulke micro-apparaten zijn ontwikkeld voor toepassingen op verschillende gebieden, van inkjetprinten tot cel isolatie in medische diagnostiek, medicijn toediening en onderzoek industrie.

De meeste micro-apparaten hebben een vast ontwerp dat is afgestemd op het uitvoeren van een specifieke taak of manipulatie activiteit. Echter, het fundamentele vermogen van een microfluïdische apparaat draait om het opvangen, scheiden, sorteren en samenvoegen van deeltjes of cellen. Deeltjesmanipulatie wordt gedaan in microfluïdica door verschillende contact technieken, zoals microkanaal geometrie en contactloze technieken zoals laservelden, magnetische velden, akoestische krachten, elektrische velden, kunstmatige trilhaartjes en hydrodynamische krachten.

De niet-hydrodynamische methoden, zoals magnetische velden, akoestische krachten en elektrische velden, hebben complexe controlemechanismen. Deze controlemechanismen zijn afhankelijk van nauw gekoppelde interacties tussen fysieke velden zoals vloeistofstroming interactie met de deeltjeseigenschappen zoals elektrische eigenschappen, chemische samenstelling, akoestische eigenschappen of de brekingsindex van de deeltjes. Daarom is het gebruik van hydrodynamische forcering voor het manipuleren en vangen van microdeeltjes een aantrekkelijk alternatief voor contactloze deeltjes opvang.

In dit proefschrift wordt het ontwerp van een microfluïdisch apparaat beschreven, die geen kanalen met fysieke muren heeft, zoals Y-junction of T-junction apparaten, maar in plaats daarvan "virtuele kanalen". Deze virtuele kanalen zijn dynamisch, flexibel en kunnen worden gebruikt als multifunctionele kanalen op een enkel apparaat om verschillende bewerkingen in één enkele chip te integreren. In deze studie, worden "virtuele kanalen" gegenereerd door alleen gebruik van hydrodynamische manipulatie. Deze aanpak kan de functionaliteit van een enkel apparaat aanzienlijk verbeteren door het deeltje of cel te transporteren naar de gewenste locaties.

Ons apparaat maakt gebruik van een uniforme stroom in de vloeistofkamer met drie loodrecht op de kamer gesitueerde inlaten om deeltjes te manipuleren. Door deze drie inlaten kunnen vloeistof worden geinjecteerd of geextraheerd uit de

vloeistofkamer om de stroomlijnen om te buigen. Aangezien de gemiddelde snelheid in de diepte over het kanaal in een Hele-Shaw-cel is rotatievrij, gebruiken we potentiële stromingstheorie om het stromingsveld voor het manipuleren van deeltjes te voorspellen. De lineairiteit van de potentiaalstromingstheorie is bij uitstek geschikt voor de snelle rekentijden die onze applicatie vereist.De geoptimaliseerde deeltjestraject met kleine stroomsnelheidsgrenzen en de minste variatie in de stroomsnelheid van de pomp wordt a priori bepaald met behulp van een optimalisatieroutine. Deze optimalisatie routine wordt een a priori algoritme voor deeltjesmanipulatie genoemd. Onze stroomapparaat geniet van de voordelen van de a priori deeltjespad voorspelling en biedt de gebruiker de mogelijkheid om meerdere functionaliteiten te integreren zoals opvangen, scheiden of sorteren op één apparaat. Deze aanpak is ook gunstig voor rapid prototyping in de vroege ontwerpfase. Het staat toe om verschillende microkanaalgeometrieën te verkennen en te bepalen welke het meest geschikt is tot een bepaalde toepassing.

Het a priori algoritme voor deeltjesmanipulatie is momenteel echter beperkt doordat er nog geen rekening wordt gehouden houden met aspecten zoals oppervlakteruwheid, deeltjesdichtheid en excentrische deeltjes positie langs de kanaalhoogte. Dit zou kunnen leiden tot fouten in het traject van de deeltjes die zich in de loop van de tijd zal ophopen, wat kan leiden tot een volledige mislukking van het experiment. Daarom is het essentieel om feedback controlemechanismen te gebruiken om zodoende onzekerheid in herhaalbare experimentresultaten te verminderen en de robustheid van de experimenten te verhogen. Met een feedback lus in de experiment, kan de fout in deeltje positie worden bepaald in relatie tot het a priori geoptimaliseerde traject, en additionele stroomsnelheden kunnen worden ingesteld om de fout te corrigeren. Voor dit doel is de prestatie van een Proportion-Integral-Derivative-based (PID) controller onderzocht. De initiële parameters van de PID-regelaar voor verschillende experimenten worden bepaald met behulp van niet-lineaire optimalisatie.

Dit proefschrift laat zien dat een stromingsapparaat met "virtuele kanalen" kan worden gefabriceerd en ingezet voor diverse toepassingen. Meerdere cruciale experimenttestgevallen zoals sorteren, vangen, scheiden, samenvoegen en mengen worden uitgevoerd in de microfluïdische apparaat om deze bewering te ondersteunen. Het succes van deze testgevallen toont het vermogen van de apparaat voor diverse toepassingen op het gebied van microfluïca. De resultaten van de PID-regelaar laten zien dat de experimenteel bepaalde deeltjesposities nauw overeenkomen met het a priori geoptimaliseerde traject. De maximale fout is in de orde grootte van één deeltje diameter aan het einde van de manipulatie.

In de toekomst, kan het micro-apparaat veelzijdiger worden door hydrodynamische forcering te combineren met akoestisch/magnetisch/elektrisch velden of optische pincetten. Tevens kan het micro-apparaat nog kleiner worden gemaakt, waardoor het interessanter wordt voor biologische toepassingen zoals cel opvang en chemische toepassingen zoals samenvloeiende druppel studie.Ook zou het toevoegen van meer inlaten het systeem meer redundant maken voor manipulatie van twee deeltjes. Het hebben van meer inlaten zal helpen om het

stromingsveld te stabiliseren. Bovendien kan een aparte optimalisatie worden gedaan om het optimum te vinden van de locatie van de inlaten en configuratie om de gewenste deeltjestrajecten te verkrijgen.

NOMENCLATURE

ACRONYMS

APS	American Physical Society
CAED	Computer Aided Engineering Drawing
CCD	Charge-Coupled Device
CF	Correction Factor
COVID-19	Coronavirus Disease 2019
DI	Deionized
DNA	Deoxyribonucleic Acid
DOC	Depth-of-Correlation
EDL	Electric Double Layer
FFT	Fast Fourier Transform
IW	Interrogation Window
MFCS-EZ	Microfluidic Flow Control System EZ
MSE	Mean Squared error
NMPC	Non-linear Model Predictive Control
PDMS	PolyDiMethylSiloxane
PID	Proportional–Integral–Derivative
PIV	Particle Image Velocimetry
PMMA	Poly(methyl methacrylate) / plexiglass
PTFE	PolyTetraFluoroEthylene
RBC	Red Blood Cells
RHS	Right Hand Side
RMS	Root Mean Square
sCMOS	scientific Complementary Metal Oxide Semiconductor
SNR	signal-to-noise-ratio

LIST OF SYMBOLS

Latin Symobls

Symbol	Description	Units
u	two-dimensional depth-average velocity field	ms^{-1}
p	prerssure	$\mathrm{Kgm}^{-1}\mathrm{s}^{-2}$
b	volumetric force	N
N	number of particles	—
M	number of inlets	—
$\underline{F}$	non-hydrodynamic interaction between particles	—
l	length	m
w	width	m
h	height	m
Wo	Womersely number	—
L	enterance length of the flow cell	m
Re	Reynolds number	—
a	particle radius	m
ΔX_m	maximum in-plane displacement	pixels
ΔX	in-plane displacement	pixels
N_{eff}	effective image density	—
N_I	image density of a single image pair	—
F_I	particle in-plane displacment	—
F_O	particle out-of-plane displacement	—
N_F	number of frames	—
F_Δ	in-plane displacement gradient	—
R	cross-correaltion magnitude	—
d_p	geometric particle diameter	m
d_τ	particle image diameter	pixels
r_{cyl}	radius of the 2D cylinder	m
g	location of 2D cylinder from the inflow	m
u_x	velocity at the surface of the 2D cylinder along x-axis	ms^{-1}
t	time scale	s
Q	volumetric flow rate	$\mathrm{m}^3\mathrm{s}^{-1}$
l_c	characteristic length scale	m
t_c	characteristic time scale	s

$\mathbf{u}_c$	characteristic uniform flow	ms^{-1}
l^*	non-dimensional length	$-$
w^*	non-dimensional width	$-$
h^*	non-dimensional height	$-$
$\mathbf{u}^*$	non-dimensional depth-average velocity field	$-$
Q^*	non-dimensional volumetric flow rate	$-$
A	influence matrix	$-$
T	pump response time	s
$r1$	input flow rate	m^3s^{-1}
c	output flow rate	m^3s^{-1}
X_{Pi}	non-dimensionalized particle position of the ith particle	$-$
t_0	time at initial particle position	s
t_f	time at final particle position	s
$\varepsilon(X_P)$	maximum deviation between experiment and pre-defined particle trajectories	%
K_p	proportional gain constant	m^{-1}
K_i	integral gain constant	$\text{m}^{-1}\text{s}^{-1}$
K_d	derivative gain constant	m^{-1}s
l_t	particle position error at time t	m
ΔQ	volumetric flow rate corrections	m^3s^{-1}
C	concentration	m^{-3}
D	diffussion coefficient	m^2s^{-1}

Greek Symobls

Symbol	Description	Units
∇	derivative	s
ν	kinematic viscosity	$\text{m}^2\text{s}{-1}$
μ	dynamic viscosity	$\text{Kgm}^{-1}\text{s}^{-1}$
ρ	fluid density	Kgm^{-3}
Θ	flow direction	degrees
Ψ	stream function	$-$
ϕ	valid detection probability	$-$
σ	volumetric flow rate per unit depth	m^2s^{-1}
α, β	arbitary constants for constrained optimization	$-$
κ_x, κ_y	correction factor in x- and y-direction	$-$

BACKGROUND

1.1 MICROFLUIDICS AT A GLANCE

Microfluidics is the study of fluid motion with small volumes (from, 1 millilitre down to 1 nanolitre) compared to large volumes (*e.g.* 1 litre) in a full-scale laboratory. Portable devices performing laboratory tasks, detecting samples, and chemical/biological analysis on a small scale are referred to as *lab-on-a-chip*. Microfluidics play an important role in platforms such as *lab-on-a-chip* for fast and accurate results compared to its full-scale laboratory counterpart. For example, the rapid antibody self-test for COVID-19 is classified as *lab-on-a-chip*. In recent years, various micro-devices have been widely investigated and developed for their applications in several fields, stretching from inkjet printing to cell isolation in medical diagnostics to drug delivery/discovery industry [1]. Advancements in micro-fabrication technologies such as 3D printing and laser cutting have also fueled rapid fabrication and the ease of implementation of micro-devices. The small-scale size of the micro-device allows small sample volumes, cost-effective and low-risk analysis for multiple purposes.

In the medical industry, particle manipulation is important in study related to particle synthesis [2, 3], bio-synthesis [4], cell-biophysics [5, 6], cell-drug response [7, 8], cell-cell interaction [9, 10], and tumor cell analysis in blood [11, 12]. In the oil and gas industry, research related to predicting the stability of emulsions through droplet coalescence [13], characterization of crude oil contents in samples [14], gas-oil equilibrium ratio measurement [15], and interfacial properties of crude-oil brine [16] are used in the field. The elementary tasks performed in all of these examples consist either of a single task or a combination of identification, trapping, separation, focusing, filtering, and sorting for cells, droplets, or particles. As the development and knowledge in particle and droplet manipulation continues, new control mechanisms are being developed for biological and physical processes to improve our understanding of particle dynamics, cell separation, coalescence, and mixing.

1.2 FLOW CONTROL TECHNIQUES

Generally, micro-devices have a fixed design tailored to carry out a specific task or manipulation activity. As discussed above, the fundamental ability of the microfluidic device revolves around trapping, separating, sorting, and assembling particles or cells. Particle manipulation is done in microfluidics with various contact techniques, using micro-channel geometry, and non-contact techniques using laser fields, magnetic fields, acoustic forces, electrical fields, artificial cilia, and hydrodynamic forces [17–21]. Microfluidic-based particle and droplet manipulation techniques can be broadly divided into passive and active techniques. Passive techniques rely on the geometry and topology of the micro-channel to carry the manipulation activity. In contrast, the active manipulation technique relyies on the physical properties of the specimen to be manipulated.

1.2.1 PASSIVE FLOW CONTROL TECHNIQUES

The passive method relies on channel geometry and the flow field to manipulate particles. The design of the channels varies depending on the application. In passive techniques, the manipulation is performed using the drag force generated by different geometries and topologies in the microchannels. Various passive methods used in practice are:

a) Deterministic lateral displacement: In this case, the particles are manipulated into different streamlines [22]. Such techniques have been used to isolate the cancer cells [23] and to separate parasites from human blood [24] by introducing specific arrangements of geometric features such as a network of micro-pillars.

b) Pinched flow fractionation: Introduction of a pinch segment, such as a contraction or expansion location in the micro-channel with a laminar flow profile, particles can be manipulated to follow a specific streamline. The particles are separated perpendicularly to the flow direction based on their sizes inside the micro-channel. This technique is used for continuous particle separation [25, 26].

c) Inertial microfluidics: At Reynolds number higher than 1, inertia becomes significant, and the particle experiences two types of inertial lift forces. One lift force is due to shear and acts towards the wall for a parabolic flow profile. The other lift force is originated from the wall-induced lift, which acts away from the wall. Due to the interaction of these forces, the particle reaches an equilibrium position in the channel cross-section. It is used for particle separation [27], focusing [28] and sorting [29].

1.2.2 ACTIVE FLOW CONTROL TECHNIQUES

In active manipulation techniques, the manipulation is carried out by applying external forces. Commonly used methods are:

a) Magnetic methods: The magnetic manipulation technique uses an external magnetic field generated by permanent magnets or electromagnets [30]. The gradient of the magnetic field is exerted on the particle-based on its size and magnetic properties. Applications such as the capture of tumor cell [31] and the removal of malaria-infected RBCs [32] have been reported using this technique.

b) Electrical methods: An electric field can be used for electro-osmotic flow, electrophoresis, and dielectrophoresis [33]. Electro-osmotic flow is the motion of the electrolyte solution under the influence of electrodes placed at the end of each micro-channel. A surplus of positively charged ions is formed near the channel walls because most channel materials such as glass and polydimethylsiloxane (PDMS) are negatively charged. This is called Electric Double Layer (EDL). Under the influence of an electric potential drop along the micro-channel, the excess positive charges in the EDL moves toward the negative electrode due to the electrostatic forces. Because of the viscosity dominated flow, the bulk liquid is propagated by the mobile layer of EDL. An application of electro-osmotic flow is in the removal of contaminants from underground water resources [34]. Electrophoresis and electro-osmotic flow are both caused by the electrostatic forces on the wall and EDL. For electro-osmotic flows, the fluid moves relative to a stationary charged surface whereas for electrophoresis, the charged surface of a particle moves relative to a stationary liquid. The migration rate of the particles depends on the electrical properties of the particle in the presence of an electrical field. An extensively used application of electrophoresis is the extraction of DNA fragments according to their size [35]. Dielectrophoresis uses a non-uniform electric field to exert force on the dielectric particles. For manipulation utilizing this technique, the particle need not to be a charged particle. The magnitude of the force exerted on the dielectric particle depends on the type of the working fluid, shape, size, and electrical properties of the particles. Dielectrophoresis has been widely used for trapping [36] and sorting [37].

c) Optical methods: An optical tweezer uses a focused laser beam. The laser beam generates a net force on the object that is oriented towards the center of the beam due to the gradient forces due to optical radiation pressure and traps the object close to the focal point. This technique was pioneered by Ashkin *et. al*. [38]. It has very high precision and has been used for single-cell manipulation [39], sorting [40] and to measure flow around cilia [41].

d) Acoustics methods: This method can be applied to any suspended particles with acoustic properties that differ from the fluid properties in which the particles are suspended. It relies on forming a standing acoustic wave between two parallel walls of the channel, where one wall is an ultrasonic transmitter, and the other wall is a reflector. This creates a pressure distribution in the fluid and the particle gets trapped in the velocity antinodes of the standing-wave acoustic field. Such techniques have been used to concentrate bacteria [42] and for size-based cell separation [43].

e) Artificial cilia: Cilia are hairlike projections present on the surface of certain cells and are primarily used for locomotion and feeding. For example, the network

of cilia in the respiratory tract helps in sweeping away particles and fluids. Similarly, artificial cilia are nature-inspired and use the asymmetric motion of the cilia to induce strong local flow that leads to hydrodynamic forces on particles [44]. This technique has been employed to transport water droplets [45] and for self-cleaning applications [46].

f) Hydrodynamic methods: Hydrodynamic traps are used to trap particles at the stagnation point of the fluid. A stagnation point is a point in a fluid flow field where the local fluid velocity is zero. This offers high-resolution trapping of single microscale and nanoscale particles [47]. Also, particles can be manipulated along the streamlines of the fluid. A streamline is a curve that is instantaneously tangent to the velocity vector of the fluid flow field. In unsteady flows, *i.e.* when the flow changes with time, the streamline pattern changes with time. Recently, further work has been done on using the streamlines of the flow to manipulate the particles [48–51]. This will be discussed in detail hereafter.

1.3 HYDRODYNAMIC METHODS

Generally, non-hydrodynamic methods, such as those using magnetic fields, acoustic forces, and electric fields, have complex control mechanisms. These control mechanisms rely on closely coupled interactions between physical fields like fluid flow field interaction with the particle properties such as particle electrical properties, chemical composition, acoustic properties, or refractive index. Therefore, using only hydrodynamic forcing for manipulating and trapping micro-particles is an attractive alternative for non-contact trapping particles [47]. In 1934, one of the pioneers, G.I Taylor trapped a drop at the center of the macroscopic scale four-roll mill. He invented this apparatus to investigate the deformation of a drop of one fluid in another fluid of the same density [52]. The diameter and the height of the cylindrical rollers were 3.81 cm and 2.39 cm, respectively. The drop was unstable along the extensional flow axis in the horizontal direction, and it would move arbitrarily along the horizontal direction. The position of the droplet was controlled by varying the roller speed of the right or left set of rollers. Controlling the position of the droplet by varying the roller speed was a complex task. In 1986, Bentley and Leal [53] improved the four-roll mill system to be controlled using a computer. This method keeps the droplet at the stagnation point, at the center between the four-roll mill. Recently, Schroeder and co-workers have extensively worked with hydrodynamic methods for particle trapping and manipulation. This work has led to the development of an automated four-channel cross-slot device to confine single particles in the device [54, 57–59].

Theoretical work has demonstrated that a sequential assembly algorithm can sequentially join particles and trap them in a seven-channel device. Using this technique, particles are arranged in the form of all the letters of the Latin alphabet
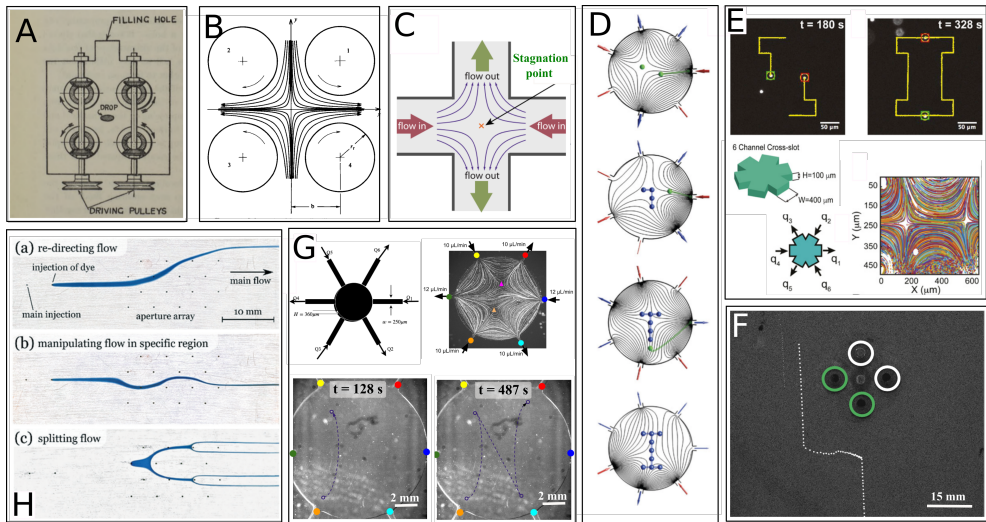
Figure 1.1: Starting from the left side (clockwise) in chronological order: (A) Schematic of the four-roll mill system developed by G.I. Taylor, used to trap objects with a fluidic stagnation point that opened up a new field of study aimed at characterizing polymers and cells by using stagnation point [52]. (B) Schematic of a computer-controlled four-roll mill (2.54 cm gap between rolls) to investigate the dynamics of a single viscous drop in another immiscible fluid. The computer control device tracks the disturbance of the trapped particle using a camera, which is transferred to a feedback system to counter such instabilities by adjusting the speed of the rolls independently [53]. (C) Schematic showing forces acting on particles at different positions within the vicinity stagnation point flow. In the compressional axis, the particle experiences an attractive force towards the stagnation point and a repulsive force in the extensional axis. The particle positioned at the stagnation point has a zero net force [54]. (D) A numerical sequential assembly algorithm was demonstrated to sequentially join particles trapped in a seven-slot channel microfluidic device to arrange particles in the form of Latin alphabet "I" in 2-D [55]. (E) Schematic of the six-channel cross-slot with relative magnitude and direction of the flow rates for generating the streamline topologies where two stagnation points are visible. Snapshots demonstrate the manipulation of the paths of two 2.2 mm beads to trace the letter "I". The yellow line is showing the spatial history of both particles [56]. (F) Time history of a $250\mu m$ bead during an experiment in a Hele-Shaw cell, where the flow was manipulated by controlling the flow rate of two ports (marked in green color) out of four ports and a uniform flow directed from bottom to top direction of the page [48]. (G) Schematic design of the microfluidic device similar to Stokes trap. However, this device uses the streamlines for particle manipulation instead of the stagnation point. The two stagnation points (magenta and orange triangles) are visible along with the streamlines in the figure. The image demonstrates manipulating a single particle by moving the particle along the streamlines to trace the letter "N" using the six inlets at the circumference of the device. The purple dashed line shows the spatial and time history of the particle [49]. (H) The device uses multiple inflection points to allow the virtual channel to manipulate the liquid stream (in blue ink) to specific regions of the flow cell [51].

in a 2D device [55]. In this approach, the time-dependent velocity field must satisfy mass conservation (equation 1.1) and the Stokes equation (equation 1.2).

$$\boldsymbol{\nabla} \cdot \boldsymbol{u} = 0 \tag{1.1}$$

$$-\boldsymbol{\nabla} p + \mu \nabla^2 \boldsymbol{u} + \rho \boldsymbol{b} = 0 \tag{1.2}$$

$$\underline{R}(\underline{x})\dot{\underline{x}} = \underline{\underline{M}}(x) \cdot \mathbf{Q} + \underline{F} \tag{1.3}$$

where $\mathbf{u}$ is the flow field, p is the pressure , μ is the fluid viscosity , ρ is the fluid density, $\mathbf{b}$ is the volumetric force, $\underline{x} = [x_1, x_2, ... x_N]$ is the position of N particles, $\mathbf{Q}$ represents the flow rates of M inlets, $\underline{F}$ corresponds to the non-hydrodynamic interaction between particles, $\underline{\underline{M}}_{jk} = K_j(x_1, x_2, ... x_N; \underline{\xi}_k)$, j denotes the particle for manipulation, ξ_k is the location of the M inlets ($k = 1, 2, 3, ... M$), $\underline{R}$ and K_j depend on the geometry of the flow cell [60].

Using the linearity of the Stokes equation, the velocity of the particles in the flow domain varies linearly with the flow rates (equation 1.3) [55]. To calculate the flow rates for a given desired particle trajectory, the matrix $\underline{M}$ must be invertible. Thus, for $\underline{M}$ to be invertible, the number of independently controlled parameters must be greater than the number of degrees of freedom of the particle. For a 2D domain, this implies that at least 2N+1 inlets are required for N particles. Shenoy *et. al.* [56] introduced a novel method for trapping particles in the stagnation point of the fluid flow field, known as the Stokes trap. Using the Stokes trap, they were able to trap two particles, each in a stagnation point simultaneously, and manipulate their path using a model predictive control [50], and particle orientation of anisotropic particles [61]. Recently, Taylor *et. al.* [51] presented a concept to guide the flow of a reagent inside a microfluidic flow cell along a reconfigurable trajectory and coined them as "virtual channels[1]".

Meanwhile, our previous work has included particle manipulation in a macroscopic Hele-Shaw cell (300×100×0.5 mm) [48], a circular device (10×0.36 mm) [49] and particle manipulation algorithm [62, 63] to manipulate particle trajectories using streamlines. In addition, our work has provided insight into a device that uses hydrodynamic forcing to move the particle in the desired trajectory.

1.4   OBJECTIVE AND SCOPE OF THE RESEARCH

The goal of the thesis is to design a microfluidic device that has no real channels with physical walls, such as Y-junction or T-junction devices, but instead have "virtual channels". These virtual channels are dynamic, flexible and can be used as multi-purpose channels on a single device to integrate various operations into one

---

[1] In the meantime, at a conference talk at the American Physical Society (APS) 2018, I coined the exact phrase in my abstract and the conference talk [62].

single chip. This approach can significantly improve the functionality of a single device by transporting the particle or cell to the desired locations. In this work, hydrodynamic manipulation is used to create such virtual channels. Such a device benefits from *a priori* particle path prediction that provides the user an opportunity to integrate multiple functionalities such as trapping, separation, or sorting onto a single device. This approach is also beneficial for rapid prototyping in the early design stage, as it allows to explore different micro-channel geometries and determine which one is best suited to a given application. In this work, "virtual channels" are generated using hydrodynamic manipulation only. Our technique uses an *a priori* estimation of the particle trajectory to optimize the particle trajectory with stable streamlines using an optimization routine. For accuracy and precision during the experiments of particles following the *a priori* optimized path, feedback control is implemented using Proportional Integral Derivative (PID) control. A PID controller is used to reduce the particle positional error between experimentally measured and pre-computed particle location by modifying the flow rate. The current work is restricted to particles in the absence of Brownian motion. The particles used for manipulation in this work have particle diameters of tens of micrometers and use water as the working fluid. Furthermore, the potential flow theory is used to model Hele-Shaw flow and predict the flow field for manipulating particles. The reasons for this are discussed in the next section.

1.5 HELE-SHAW FLOW CELL - AN INTRODUCTION

The Hele-Shaw flow cell is named after its inventor Henry Selby Hele-Shaw (1854–1941), who was an English mechanical and automobile engineer. He developed several important inventions such as variable-pitch propeller, streamline filters, and the Hele-Shaw flow cell [64]. Hele-Shaw flow is a laminar flow between two parallel plates. The two plates of length l and width w are separated by a distance h along the z-direction (see Figure 1.2). The Hele-Shaw condition only applies when the in-plane dimension l is much greater than the channel height h *i.e.* $l \gg h$. The Hele-Shaw condition becomes valid at an in-plane distance of $\sim h$ from the boundary of the flow domain. The velocity profile is parabolic in the z-direction due to the pressure gradient in the *(x,y)* plane:

$$\boldsymbol{u} = -\frac{1}{2\mu}(h - z)z\boldsymbol{\nabla}p \quad \text{with:} \quad 0 \leq z \leq h, \tag{1.4}$$

where $\mathbf{u}$ is the velocity field in the *(x, y)*- direction, h the channel height, z the coordinate along the wall-normal direction, μ the viscosity and $\boldsymbol{\nabla}p$ the pressure gradient. From equation 2.1, the velocity field $\mathbf{u}$ can be fully determined from the depth-averaged velocity field. A simplified notation is used here, and we refer to $\mathbf{u}$ = (u,v) as the two-dimensional depth-average velocity field in the *(x,y)*-plane. For a Hele-Shaw cell, the depth-averaged velocity field $\mathbf{u}$ is a potential flow, and the velocity potential can be identified as the pressure field; see equation 1.4. Assuming
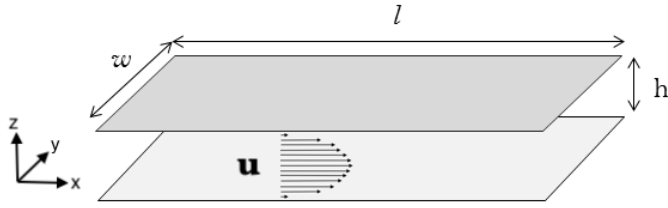
Figure 1.2: Schematic of a Hele-Shaw cell with the length l, width w, and height h. The flow is uniform in the x-direction and has a parabolic distribution over the height in the z-direction. The depth-averaged velocity in the x-direction is denoted as **u**.

the depth-averaged velocity field to be a potential flow, one can further deduce the depth-averaged velocity field from the direction field as the velocity field.

In the past, the Hele-Shaw flow cells have been extensively used to visualize flow patterns using dye injection and hydrogen bubbles around a cylinder or an airfoil. It has been an essential tool in providing qualitative insight, establishing flow models as a basis for mathematical models, and explaining fluid motion. In this thesis, the flow cell is designed such that the length of the flow cell is larger than the width of the flow cell. Moreover, the width of the flow cell is an order of magnitude larger than the channel height. Thus, the Hele-Shaw approximation of the flow field is valid. Hence, this thesis uses the Hele-Shaw approximation to develop a mathematical model that uses time-varying streamline patterns for various applications such as trapping, sorting, and separating particles. A cautionary note: the parabolic flow profile obtained from the Hele-Shaw approximation is valid in a stationary flow. The Womersley number (defined as $Wo = h\sqrt{2\pi/\nu T}$, where h is the channel height, ν is the kinematic viscosity, and T is the time scale of the oscillation) is used to determine the time scales below which the flow has not fully developed into a parabolic flow profile. A parabolic flow profile can be assumed for time scale T such that $Wo \ll 1$. Given the channel heights and the fluids used in this thesis, the parabolic profile is distorted for time scales ≈ 0.8 seconds. For laminar flow, $L = 0.05 \cdot Re \cdot h$, where L is the entrance length, $Re = uh/\nu$ is the Reynolds number and u is the flow velocity in x- or y-direction, so for the Re (≈ 0.03) used in the experiments described in the thesis, L is negligible.

1.6 OUTLINE OF THE THESIS

The following four chapters of this thesis are divided as follows. In Chapter 2, a new measurement technique, Psi-PIV, is introduced. It was developed to mitigate certain problems related to the measurement of unsteady flow in microfluidic devices. The algorithm is explained and validated by comparing it with the simulated PIV data. The velocity field corresponding to the flow around a cylinder and a developing

Rankine half-body (*i.e.* superposition of uniform flow and source flow in a potential flow) are studied and assessed using the Psi-PIV and PIV algorithms.

The development of the *a priori* particle manipulation algorithm and the experiments are detailed in Chapter 3. The device is a Hele-Shaw cell with multiple ports which are used to inject or extract small volumes of the working liquid. First, the device design is validated by comparing the location of stagnation point of the Rankine half-body obtained from the experimentally measured data with the location obtained from COMSOL simulations and from a potential flow solver. Secondly, the characteristics of the particle manipulation algorithm are assessed numerically. Furthermore, experiments are performed with particles in the microfluidic device for different test cases such as single-particle deflection, single-particle trapping, moving two-particles away from each other, bringing two particles close to each other and switching two particles.

In Chapter 4, a Proportional–Integral–Derivative (PID) control loop is introduced to improve the repeatability and accuracy of the above-mentioned manipulations. The device design and the *a priori* use of a particle manipulation algorithm remains unchanged. The PID controller is used to correct the spatial error between the particle position that is determined from the *a priori* particle manipulation algorithm and the experimental particle position. The PID controller is tuned by an optimization routine where the cost function finds an optimal value of PID controller constants that are valid for all the desired manipulations. The benefit of a feedback loop is assessed for single-particle experiments by comparing with the particle position error from the no-feedback test cases. Moreover, an additional investigation with pollen grain is done, where a pollen grain is randomly selected and trapped for a pre-defined duration.

The work is concluded in Chapter 5, where the conclusions from the thesis are presented, and an outlook on possible future research in the field of hydrodynamic flow manipulation is discussed.

# PSI(Ψ)-PIV: A NOVEL FRAMEWORK TO STUDY UNSTEADY MICROFLUIDIC FLOWS

In microscopic particle image velocimetry (micro-PIV), correlation averaging over multiple frames is often required, leading to a loss in temporal resolution, therefore limiting the measurement accuracy for unsteady flows. Here, a new PIV method is presented that is suitable to study steady and unsteady laminar flows between parallel plates (i.e. Hele-Shaw flow), which is a standard flow configuration in microfluidic applications. Our method reduces the effective seeding density and yields similar if not higher signal-to-noise-ratio (SNR) compared to conventional micro-PIV. This algorithm is termed as Ψ-PIV. Ψ-PIV requires a much smaller number of frames to reach the same SNR compared to the widely used correlation averaging method. This leads to a significant improvement of the temporal resolution. The Ψ-PIV algorithm is used in an experimental investigation of steady and unsteady flows in a Hele-Shaw cell. Our experiment shows that Ψ-PIV reduces the number of required frames by 8 times and 30 times compared to the frames required by conventional PIV for steady and unsteady laminar flow. In this study, PIV and Ψ-PIV use a single-pass cross-correlation to present the underlying difference between the two approaches.

2.1   INTRODUCTION

Microscopic particle image velocimetry (micro-PIV) differs from conventional PIV in two main aspects [65–67]: (i) the image density is usually much lower, $N_I \leq 1$ and (ii) the entire measurement volume is illuminated, rather than a thin light sheet. The low image density is usually compensated by performing correlation-averaging [68], *i.e.* the spatial correlation for a given interrogation domain over several image pairs. Typically, the correlation-averaging over 10-20 frame pairs is required to reach a sufficient effective image density of around 10 [68, 69]. In addition, the use of volume illumination also increases the number of frames N_F required. In correlation-averaging, N_F helps in building up the spatial correlation by the superimposition of the correlation data from the image density of each pair multiplied by the number of frames in the recording sequence. A volume illumination implies that the measurement domain is limited by either the depth-of-correlation (DOC) [70] or the physical edges of the measurement section. When the depth-of-correlation is small with respect to the depth of the flow

(a) Uniform flow   **(b)** Poiseuille flow
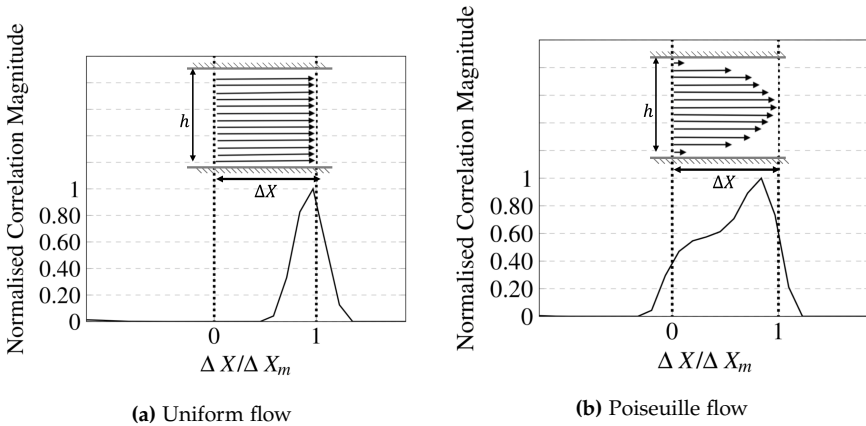
Figure 2.1: Correlation average over the channel height h for 50 frames for uniform flow and Poiseuille flow. The synthetic images are created with particle image size, d_τ = 3 pixels, maximum in-plane displacement ΔX_m = 8 pixels.

domain, there is a little variation in the velocity of the tracer particles (other than the variation due to Brownian motion). However, when the depth-of-correlation is not small with respect to the depth of the flow domain, or even exceeds the dimension of the flow domain, there is a substantial variation of the tracer velocities [71]. Such is the case for the flow in a Hele-Shaw cell, for which the distance between the two flat plates h is smaller than the depth-of-correlation. In this case, the displacement-correlation peak (see Figure 1) is substantially broadened because of the Poiseuille flow profile between the plates. In the figure, displacements ΔX are normalized by the maximum centerline displacement ΔX_m. In addition, the detection of the displacement peak leads to a bias in the measured

velocity [71]. As a consequence, a much larger number of frame pairs is needed to obtain a sufficient signal-to-noise-ratio to detect the displacement-correlation peak. In the case of a Hele-Shaw flow cell where the measurement volume includes the full height of the cell and the variation of the velocity spans the full parabolic velocity profile, it is necessary to use much more than 100 frame pairs for the correlation-averaging [72]. This makes it very difficult to apply micro-PIV to unsteady microfluidic flows.

In conventional micro-channels the channel width is on the order of the channel height, but in this work, the focus is on microfluidic flows where the width of the channel is much larger than the channel height. In these cases the Hele-Shaw condition applies. Such test cases are of interest when studying particle manipulation in a microfluidic chip [56, 73], density-driven flows [72, 74–77], flow behavior of power-law fluids [78], magnetic-field-driven instabilities [79], Marangoni effects [80, 81] and flow around a cell [82, 83]. In practice, for micro-PIV measurements with a large field-of-view, the DOC is also large [71]. For small DOC, only the particles in the thin measurement plane are in focus and hence more image frames are required to get an effective image density of 10-20 particles. In this chapter, a novel approach is presented that makes it possible to obtain reliable results for the estimation of the flow field in a Hele-Shaw cell-like geometry, for which the velocity of the tracers varies significantly over the depth of the measurement domain.

It was theoretically shown by Ho and Leal [84] that the particles migrate to an equilibrium position at a migration length, $X = 36\pi h(h/a)^3/Re$ and $Re = uh/\nu$, where h is the channel height, a is the particle radius, u is the velocity in length-wise direction and ν is the kinematic viscosity. For a generic microfluidic condition: $h = 100~\mu m$, $a = 10~\mu m$, $Re = 1$, the migration length required for the particles to reach equilibrium is approximately 11 m. This makes it challenging to manipulate the particles into their equilibrium position. The Ψ-PIV method requires less than 10 frame pairs, even considering the effect of uniform particle concentration in the Poiseuille flow. The method is explained in section 2.2, while in section 2.3 the method is validated using synthetic data. In section 2.4, an experimental validation of Ψ-PIV is presented for the flow around a 2D cylinder in a Hele-Shaw cell. Section 2.5 details the experimental setup and results from an investigation of unsteady flow around a developing Rankine half-body. The advantages and limitations of our method are discussed in section 2.6.

2.2 Ψ-PIV PRINCIPLE & WORK-FLOW

A laminar flow is considered between two parallel plates, i.e. a Hele-Shaw flow. The two plates of length l and width w are separated by a distance h along the z-direction (see Fig. 2.2). The Hele-Shaw condition only applies when the in-plane dimension l is much greater than the channel height h i.e. $l \gg h$. Hele-Shaw condition becomes valid at a in-plane distance of $\sim h$ from the boundary of the flow domain. The
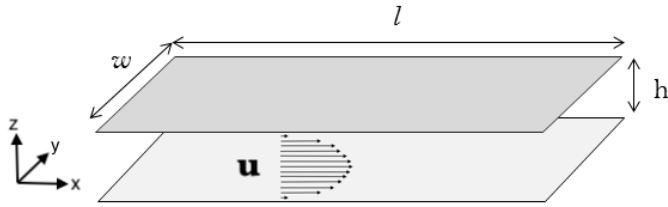
Figure 2.2: Schematic of a Hele-Shaw cell with the length *l*, width *w*, and height *h*. The flow is uniform in the *x*-direction and has a parabolic distribution over the height in the *z*-direction. The depth-averaged velocity in the *x*-direction is denoted as **u**.

velocity profile is parabolic in the *z*-direction due to the pressure gradient in the *(x,y)* plane.

$$\boldsymbol{u} = -\frac{1}{2\mu}(h-z)z\boldsymbol{\nabla}p \quad \text{with:} \quad 0 \leq z \leq h \tag{2.1}$$

where **u** is the velocity in the *x*, *y*- direction, *h* the channel height, *z* the wall-normal location in the channel, *μ* the viscosity and $\boldsymbol{\nabla}p$ the pressure gradient. From equation 2.1, the velocity field **u** can be fully determined from the depth-averaged velocity field. A simplified notation is used to refer to **u** = (u,v) as the two dimensional depth-average velocity field in the *(x,y)*-plane.

Our approach is based on the observation that for a Hele-Shaw flow, the flow direction can be established from fewer frames than the averaged flow magnitude. This is because the flow in Hele-Shaw flow is two dimensional and at a given (*x,y*) location, the direction of the velocity of a particle is independent of its location along the *z*-axis; see equation 2.1. The flow direction can be estimated at each interrogation position to construct the direction field of the velocity field and in turn, used to reconstruct the instantaneous streamlines. For a Hele-Shaw cell, the depth-averaged velocity field **u** is a potential flow and the velocity potential can be identified as the pressure field; see equation 2.1. Assuming the depth-averaged velocity field to be a potential flow, one can further deduce the depth-averaged velocity field from the direction field as the velocity field.

In the following, the work-flow used to reconstruct the depth-averaged velocity field using the Ψ-PIV algorithm is described. Fig. 2.3 represents the flow chart associated with Ψ-PIV and is compared to conventional micro-PIV. Similar to conventional PIV, single frames are divided into interrogation sections and image pairs are used to compute the cross-correlation function over each interrogation window. Unlike conventional PIV, the correlation map is not used to find the displacement-correlation peak but instead to find a direction-correlation peak. For the directional-correlation map, single frames of PIV images are divided into interrogation sections as shown in Fig. 2.3 and the image pairs are used to compute the ensemble correlation averaging [68] of fewer frames. Next, for each angle, all the values of the averaged-correlation map are summed up along a line with its origin fixed at the center of the correlation map. The length of the line is
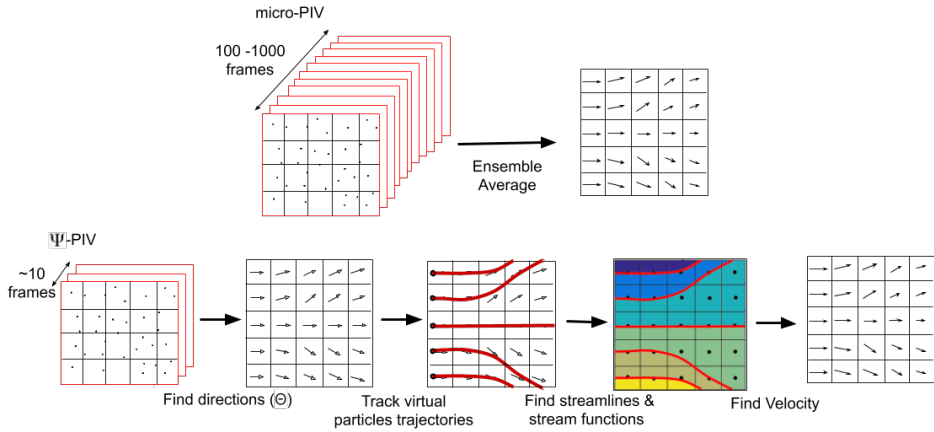
Figure 2.3: The principal difference between the micro-PIV and Ψ-PIV algorithms. In micro-PIV, correlation-averaging of a large number of frames is taken to estimate the velocity field which is shown by solid arrows. In Ψ-PIV, the local direction Θ of the flow is estimated from fewer frames. The direction of the flow is shown as the unit length arrows for each interrogation window. The red lines show streamlines that are determined by advecting virtual particles along the measured directions. The stream function values are obtained by nearest neighbor interpolation of streamlines and are assigned to the center location of each interrogation area (marked as black circular symbols). The velocity marked as solid arrows is calculated from the spatial differentiation of the stream function values with respect to the distance between two consecutive interrogation areas.

identical to the half-length of the correlation map. It is done by retrieving the intensity values of pixels from the correlation-averaged map along the line. The summed-up value along the line is calculated for every angle Θ from -180° to 180°. The pixel intensity value along the line for each angle is calculated by interpolation from the nearest pixel values of the correlation-average map. The angle corresponding to the highest peak of the directional correlation gives the most plausible direction of the flow in that interrogation window. The measured flow direction field is used to deduce the depth-averaged velocity field. When the velocity becomes zero, the correlation will have a single peak at the origin of the correlation, and it is no longer possible to determine an unambiguous flow direction. In our correlation analysis this situation is detected and labeled accordingly. In practice this is mitigated by the fact that a zero velocity is only encountered on stagnation points or separation points, where streamlines end (or would originate). These are limited to small areas in the flow and can be identified from the surrounding streamlines. It is noticed that the ambiguity in the determination of flow direction is least if the average particle image in-plane displacement is around 1/4th of the interrogation window size. Previous studies have shown the particle displacement gradient to reduce the amplitude of the correlation peak and broadens its width. At low effective image density N_{eff}, the

broadened correlation peak splits into a series of multiple aligned peaks, which is beneficial for our method as the sum of pixel values of more peaks increases the probability of finding the true flow direction. First, instantaneous streamlines are computed from the direction field using a 4th order Runge-Kutta integration scheme. Here the flow at the inlet is considered to be uniform, and determine the directional stream function. The value of the stream function at the center point of each interrogation window can be deduced from the (instantaneous) streamline pattern. Assuming a uniform flow at the inlet $\mathbf{u} = (U,0)$, the values of the stream function are determined for each streamline at the inlet. To assign the inlet stream function values to each point in the image domain, the streamlines at the inflow side of the image should preferably be parallel to each other i.e. uniform flow. In that case it is trivial to assign a value to each of the streamlines. In the case of a non-uniform inflow it would generally be possible to determine an appropriate stream function. For example, the flow velocity and the stream function from a source enclosed by the walls can be computed using a panel method. In general, this does not represent a significant complication, because, in most practical microfluidic application of Hele-Shaw flows, the inflow is generally uniform. The stream function (Ψ) in the rest of the domain is calculated at the center of each interrogation window by interpolation from the nearest streamline value. Finally, the velocity components in x- and y-direction are deduced from the stream function:

$$u = \left(\frac{\partial \Psi}{\partial y}\right), \quad v = -\left(\frac{\partial \Psi}{\partial x}\right) \tag{2.2}$$

It is expected that this method will reduce the data acquisition time required to measure the displacement field with the desired accuracy. This approach is validated with simulations using synthetic images and implement Ψ-PIV algorithm for velocity measurements in an experimental study of unsteady Hele-Shaw flows.

2.3   PROOF OF CONCEPT USING SYNTHETIC DATA

2.3.1   GENERATION OF SYNTHETIC DATA

Synthetic images were generated in order to validate the Ψ-PIV algorithm described in the previous section. Image sequences represent a uniform flow at the inlet, along the span-wise y-direction, and a parabolic Poiseuille flow along the z-direction. The main objective is to assess the reliability of Ψ-PIV to estimate the velocity field. In the synthetic data, the Brownian motion of the particles and the background noise from the image sensor are not take into account. The effectiveness of the Ψ-PIV algorithm is demonstrated in the Poiseuille flow with a uniform distribution of tracer particles. The tracer particles are uniformly scattered in the channel across the channel height and inserted at random positions at the inlet in order to keep the image density constant across all frames. The defocusing effect in size and intensity

of the particle images are not modeled in the synthetic data because the focus is on the measurements where the DOC is larger than the channel height. All images are generated with an image size of 1024×1024 pixels with 8-bit grey level quantization. The particles in the synthetic images are well resolved and have a mean particle image diameter of 3 pixels. The center-line displacement for the Poiseuille flow profile was kept at 8 pixels. The seeding density N_I was kept as 6 particles on an average in a 32×32 pixel interrogation window. Synthetic images are processed using a single-pass FFT cross-correlation with 32×32 pixel interrogation windows and without overlap.

The flow is considered uniform at the inlet and in the x-direction. Fig. 2.4 represents the contour plot of the cross-correlation function and for a particular interrogation window the corresponding correlation function and directional-correlation function. Fig. 2.4a,d,g,j represent the correlation function for the same interrogation window computed using a decreasing number of frames. Using 1000 frames, the correlation map displays low noise and presents a single strong signal peak; see Fig. 2.4a. The location of the maximum peak corresponds to the depth-averaged flow velocity because of the convolution of particle image size with the sampled velocity probability density function. As mentioned in the previous section, this correlation peak is broadened because of the displacement gradient effects; see Fig. 2.4b. Fig. 2.4c shows the directional-correlation of the correlation map for correlation-averaging of 1000 frames. In this case, the highest peak is at 0° because of the strong signal peak in the correlation map (see Fig. 2.4a). The directional-correlation peak is not broadened because the former only determines the direction and is not affected by the displacement gradient of the flow. As discussed before, a higher image density N_I is achieved in micro-PIV by correlation-averaging of several image frames N_F. Hence, the noise level (ratio of second highest peak to the highest peak of the correlation map) increases with a decrease in N_F. In this case, the SNR in the correlation map decreases because of erroneous correlation-averaging between the moving particles and particles attached to the wall. The correlation map clearly shows that the noise due to random correlations increases monotonically as the number of frames reduces from 1000 frames (Fig. 2.4a) to 50 frames (Fig. 2.4d), 10 frames (Fig. 2.4g) and 5 frames (Fig. 2.4j). For a larger number of frames, superposition of the spatial-correlation from each frame is large enough to determine the depth-averaged particle image displacement as shown in Fig. 2.4b. For less than 50 frames (Fig. 2.4e), the peak splits into a chain of multiple aligned peaks, see Fig. 2.4d and 2.4g, leading to the erroneous measurement of the displacement. This happens when the particle image diameter d_τ is smaller than the amplitude of the displacement gradient in the flow. For 10 and 5 frames, no clear peak is determined because of the strong measured random correlations as shown in Fig. 2.4h and Fig. 2.4k, respectively. Since directional-correlation is determined by integrating the correlation map values at each angle Θ from -180° $< \Theta \leq$ 180°, it can be robustly computed for a correlation map with higher random noise. For 50 frames (see Fig. 2.4d) and 10 frames (see Fig. 2.4g), all the small peaks within the
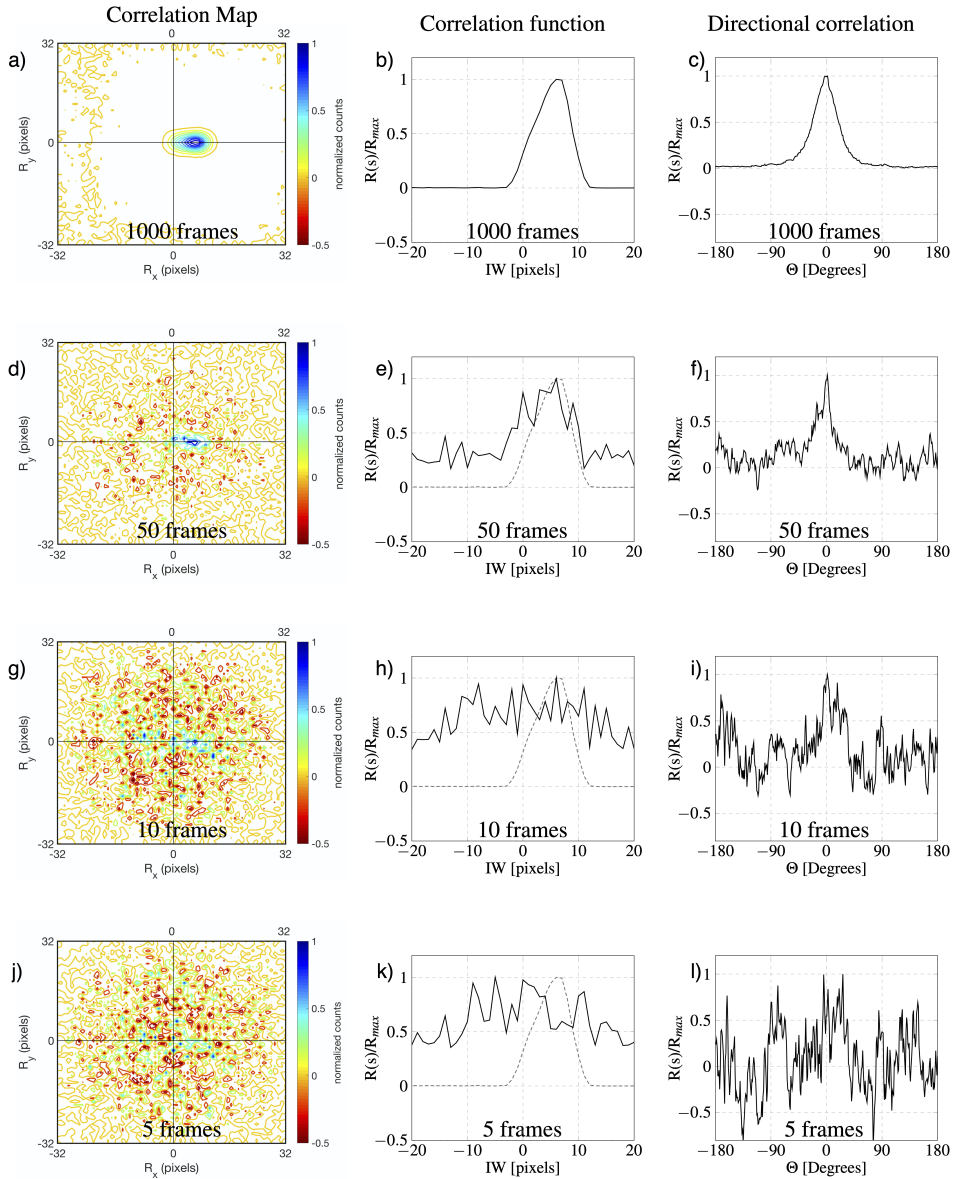
Figure 2.4: Contour plot, corresponding correlation-averaging and the directional-correlation over frames: 1000 (a,b,c), 50 (d,e,f), 10 (g,h,i), 5 (j,k,l); dashed gray line in (e,h,k) shows the correlation function of well resolved result for 1000 frames for qualitative comparison. The normalized cross-correlation magnitude is denoted by $R(s)/R_{max}$. For cross-correlation functions, the data within the range of -20 pixels to 20 pixels is only shown for better visualization.
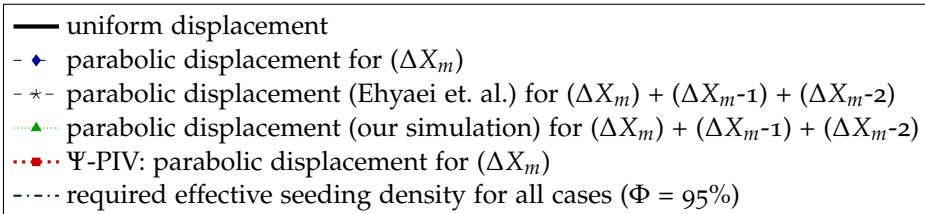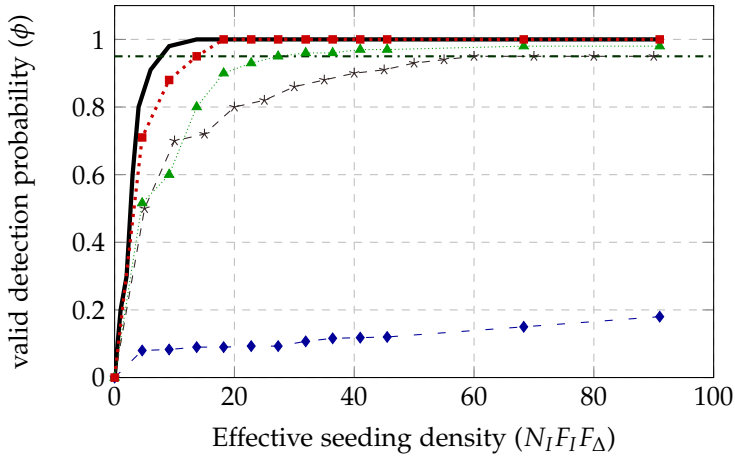
Figure 2.5: Valid detection probability for the displacement correlation peak as a function of the mean number of the particles within an interrogation window and compared with the result of uniform displacement.

chain of aligned peaks contribute to the peak in the directional-correlation, which can be clearly identified, see Fig. 2.4f and 2.4i. For fewer frames than 10, Fig. 2.4l shows that the directional-correlation peak can no longer be determined because of the strong measured random correlations.

2.3.2 VALID DETECTION PROBABILITY

Next, the valid detection probability ϕ is computed for varying effective seeding density, and compare Ψ-PIV to other PIV approaches reported in the literature, see Fig. 2.5. The valid detection probability is defined as the probability of the highest correlation peak which corresponds to the true mean displacement. [85] demonstrated that the probability of determining the true displacement peak improves as the average number of particle pairs in the interrogation area increases. This average number of particles within the interrogation area is represented by $N_I F_I F_O$ where N_I is the image density for a single image pair, F_I is the in-plane displacement of particles in an image pair and F_O is the out-of-plane motion of the particles. For uniform flow, conventional PIV requires a value of $N_I F_I F_O \approx$ 8-10 particles to reach a valid detection probability greater than 95% [86],[67]. However, in our case, $N_I F_I F_O$ is not an accurate measure of the effective

image density N_{eff} because the flow in the channel is two dimensional and volume illumination is used. Therefore, the loss of correlation is not due to the out-of-plane component and $F_O = 1$. Rather, it is due to the strong velocity gradient along the z-direction of the Poiseuille flow, and the loss of correlation is better represented by the in-plane displacement gradient F_Δ [87]. In addition, N_F, defined as number of frames is used to average the correlation data from each image pair, to improve the spatial correlation. Therefore, $N_{eff} = N_F N_I F_I F_\Delta$ is used as the effective seeding density to characterize the valid detection probability. Fig. 2.5 represents the valid detection probability for the synthetic data with different methods. Ehyaei *et. al.* [72] reported a similar figure for their method using 2 frames from a sequence of images ($N_F = 2$). Therefore, $N_F = 2$ is kept in Fig. 2.5 for consistency in the comparison between methods. For a uniform flow with a uniform flow profile along z-direction (i.e. $F_\Delta = 1$), the probability of finding the true displacement-correlation peak approaches 0.95 for $N_I F_I F_\Delta \approx 8$. For a parabolic velocity profile along the z-axis, a much higher effective image density is required to reach a valid detection probability of 0.95 . In Fig. 2.5, the valid detection probability of the maximum in-plane displacement ΔX_m for a parabolic profile, shows poor performance. This is due to the particle size biasing effect, where the maximum peak is located at 1 pixel less than the true displacement value. Ehyaei *et. al.* [72] showed that a higher valid detection probability can be reached. This however comes at a price of decreasing the spatial resolution. They [72] considered peaks at the locations of the true maximum displacement (ΔX_m), 1 pixel less than the maximum displacement ($\Delta X_m - 1$) and 2 pixels less than the maximum displacement ($\Delta X_m - 2$) to compute the signal-to-noise ratio. Using this methodology, they reached a valid detection probability of approximately 0.94 at $N_I F_I F_\Delta$ equal to 100, see Fig. 2.5. This result was obtained in their investigation using synthetic data ($\Delta X_m = 15$ pixels, $d_\tau = 4$ pixels) for a flow profile along the channel height. The algorithm developed by Ehyaei *et. al.* [72] is applied to our synthetic images and computed the associated ϕ. Similar values for ϕ are reached in our synthetic data; see Fig. 2.5. In our case, the valid detection probability curve is slightly higher reaching 0.95 for $N_{eff} = 30$. This is because the displacement gradient in our synthetic data was not as high as compared with the algorithm developed by Ehyaei *et. al.* [72]. Finally, Ψ-PIV is applied where the valid detection probability approaches 1 for a much lower effective seeding density (N_{eff} of 20 particle image pairs) because only the direction of the flow needs to be determined. The valid detection probability of 0.95 is reached with $N_{eff} = 17$; see Fig. 2.5.

The performance of Ψ-PIV is further characterized as a function of the interrogation area and the number of frames. Since the interrogation window size was kept constant at 32×32 pixels throughout the analysis done in Fig. 2.5, the valid detection probability of Ψ-PIV as a function of the interrogation area for the same synthetic data is studied; see Fig. 2.6. As expected, the valid detection probability exceeds 0.95 when there are at least 22 particle image pairs in the interrogation area. The number of frames N_F was equal to 2 in the analysis shown in Fig. 2.5. Hence, the minimum number of frames is determined that is required
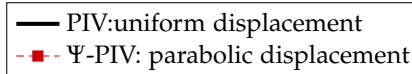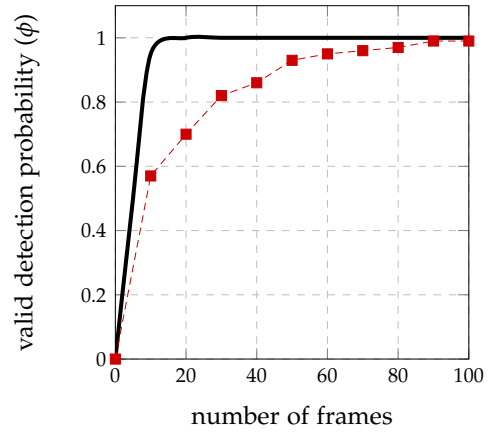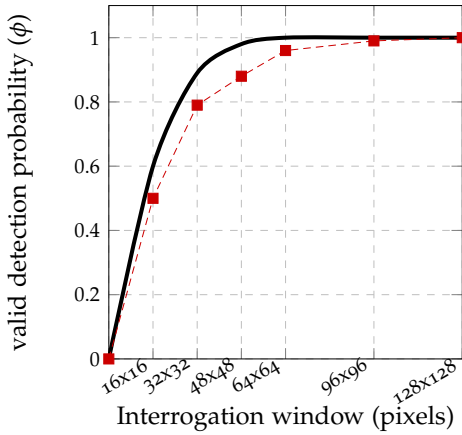
Figure 2.6: Valid detection probability as a function of interrogation area for synthetic data with $N_I = 6$. The solid line represents uniform flow result from [86].

Figure 2.7: Valid detection probability as a function of the number of frames for synthetic data with $N_I = 1$. The solid line represents uniform flow result from [86].

to reach a valid detection probability of 0.95 by Ψ-PIV. The valid detection probability was calculated for synthetic images with similar properties as used before, but with lower seeding density (less than about 1 particle image on average in a 32×32 interrogation window). This would mimic severe particle loss in the flow domain because of particle clogging at the inlet or particles getting attached to the channel wall. Fig. 2.7 shows that if the interrogation area is 32×32 pixels then a minimum of 50 image frames are required to have a valid detection probability of 0.95. This translates here to approximately 50 particle images in an interrogation area. In this case, the higher image density requirement could be the result of having less than about 1 particle image on average in an interrogation window.

The performance of the Ψ-PIV algorithm is characterized with separate experimental setups investigating two different flow cases, namely the flow around 2D cylinder and a Rankine half-body. The details of the experiments are described below.

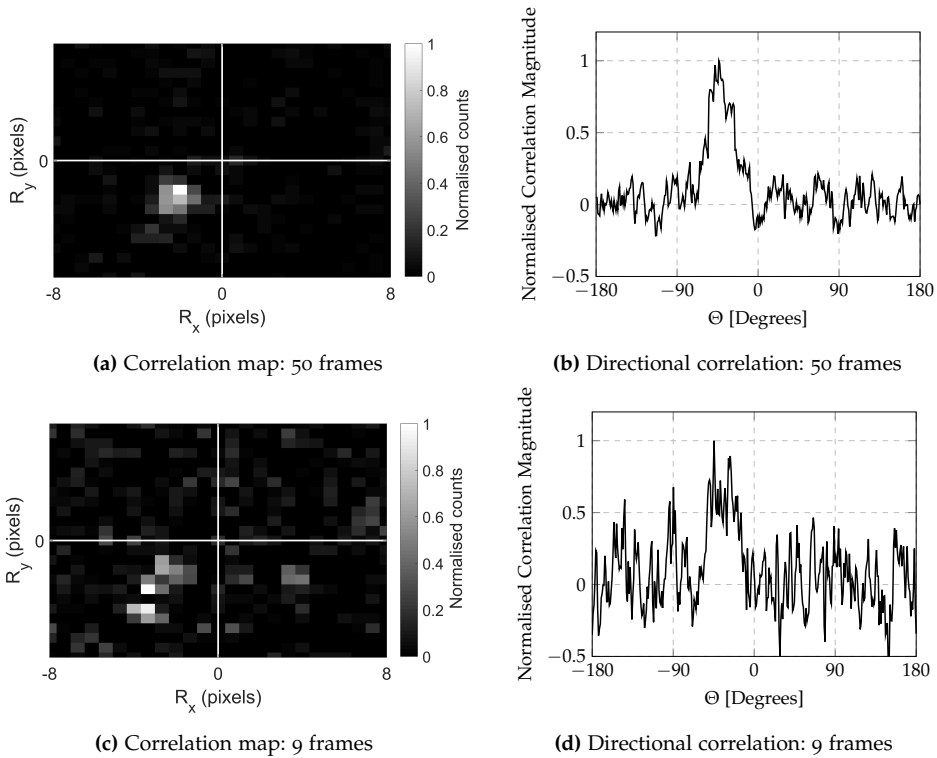**Figure 2.8:** Experimental test setup with all the required components. On the top right corner the schematic of the Hele-Shaw cell (l = 300 mm, w = 100 mm, h = 500 μm) is shown with the location of the cylinder (g = 180 mm) and the inflow direction from three inlet holes to yield an depth-averaged uniform flow **u** along the transverse direction of the cell. The diameter of the 2D cylinder is 60 mm. The velocity at the surface of the 2D cylinder along the x-axis is denoted as u_x.
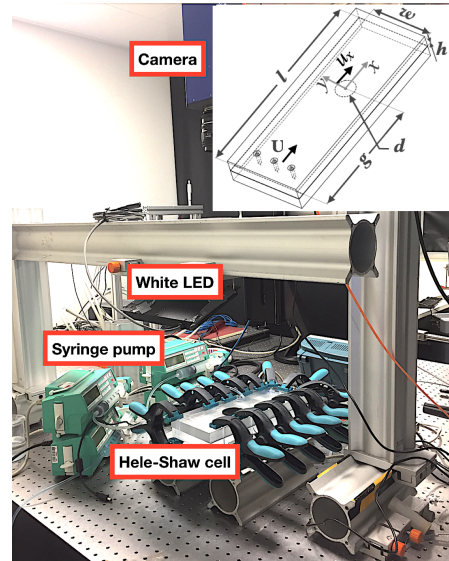
2.4   STEADY FLOW AROUND A 2D CYLINDER

2.4.1   EXPERIMENTAL SETUP

In the first measurement, the Hele-Shaw cell is built from two PMMA plates of length l = 300 mm and width w = 100 mm, see Fig. 3.1. The two plates are separated by spacers height of h = 500 μm and are clamped on the edges to keep h constant throughout the channel length. A cylinder with radius r_{cyl} = 30 mm and thickness h = 500 μm is placed at the center of the channel at a distance g- = 180 mm from the inlet; see Fig. 3.1. Syringe pumps (Cetoni neMESYS) were used to generate a pressure-driven flow with a centerline velocity of **u** = (0.06 mm/s, 0) which yields a gap based Reynolds number Re = 0.034. The working fluid was water, seeded with polystyrene microspheres with a mean particle diameter of 180-200 μm (Cospheric). Images were recorded with a CCD camera (LaVision Imager Intense) with a 1376×1040 pixel image format, 6.45 μm pixel pitch, and 12-bit grey level dynamic range. The camera was equipped with a Nikon objective with a 35 mm focal length and a magnification factor of 0.20. An f-stop of 8 was chosen in order to have a depth-of-field of 1 mm, which ensures that all particles within the channel are in focus. A depth-of-correlation DOC of 10 mm is chosen such that the DOC is larger than the channel height. This also ensures that all tracer particles are in focus and contribute to the correlation averaging. A camera exposure time of 2 ms was chosen to allow enough light to enter the image sensor for clear identification of the particle images. The active sensor size was cropped to 992×992 pixels to coincide with the flow region. An

(a) Correlation map: 50 frames

(b) Directional correlation: 50 frames

(c) Correlation map: 9 frames

(d) Directional correlation: 9 frames

Figure 2.9: Ensemble cross-correlation for 32x32 pixels interrogation window where the flow direction was calculated as -43° for 50 averaged images and 9 averaged images. For cross-correlation maps, the data is shown within a range of -8 pixels to 8 pixels for better qualitative representation. The directional-correlation in both cases shows the determined flow direction as -43°.

acquisition frequency of 2 Hz was used to capture the average in-plane displacement of about 1 pixel between two consecutive recordings. To get the maximum particle image displacement without correlation loss due to excessive in-plane displacement, a common practice is to keep the particle image displacement smaller than one-quarter of the interrogation window size [85]. Hence, for the interrogation analysis 8 frames were skipped to increase the velocity dynamic range (defined as the ratio of maximum to minimum resolvable velocity) of the recorded data. PIV images were pre-processed to remove the images of the particles, which were attached to the wall. A moving average filter in time over 9 frames is used to find the local minimum intensity value. This was subtracted from each frame, which effectively removes the background.
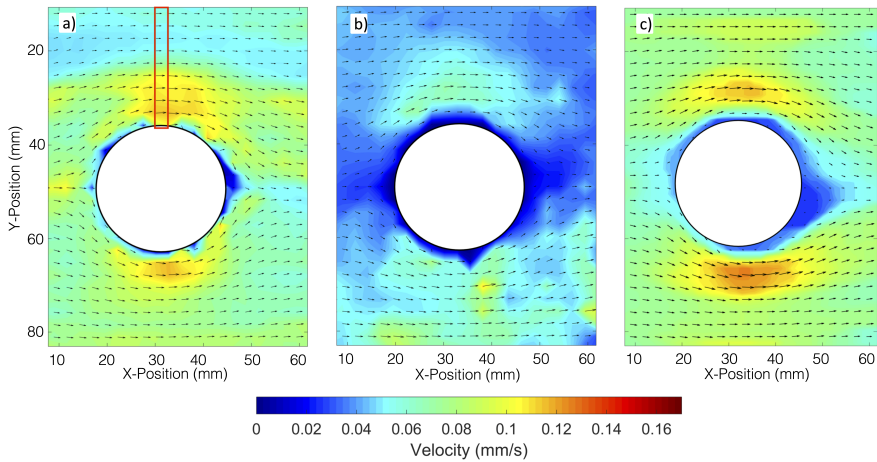
Figure 2.10: Results of flow around a 2D cylinder in a Hele-Shaw cell. The velocity direction is from left to right. (a), (b) corresponds to PIV results from correlation-averaging of 217 frames and 9 frames respectively. (c) shows the result Ψ-PIV for the correlation-averaging of 9 frames. The red rectangular domain in (a) is the area which is considerd in Fig. 2.11 and Fig. 2.12 for quantitative comparison between PIV and Ψ-PIV measurements.

2.4.2 DIRECTIONAL-CORRELATION PEAK IDENTIFICATION

The proposed Ψ-PIV approach is robust regardless of the direction of the flow. For instance, an interrogation window with an arbitrarily chosen flow direction of -43° from the experimental data of flow around a 2D cylinder in a Hele-Shaw cell (described in section 2.4.1) was considered for the directional analysis. Fig. 2.9a represents the correlation map for 50 averaged images, where the broadened peak is at an angle of -43° with respect to the x-axis. The corresponding normalized directional-correlation function is shown in Fig. 2.9b. For the same interrogation window, the top view of the correlation averaged map over 9 images is shown in Fig. 2.9c. In this case, multiple strong peaks are present in the direction of the flow *i.e* -43°. The corresponding normalized directional-correlation function is shown in Fig. 2.9d. For every interrogation window in the image domain, the flow direction is determined in a similar fashion.

2.4.3 EXPERIMENTAL RESULTS

Fig. 2.10a,b shows the velocity field obtained from the same experiment by using a conventional PIV algorithm with correlation-averaging over 217 frames and 9 frames respectively. In both cases, the interrogation windows had a size of 32×32 pixel with 0% overlap. Using 9 frames, the conventional PIV yields an estimate of the flow velocity that is significantly lower than the actual velocity. The velocity vectors are not adequately resolved, because the effective image density is
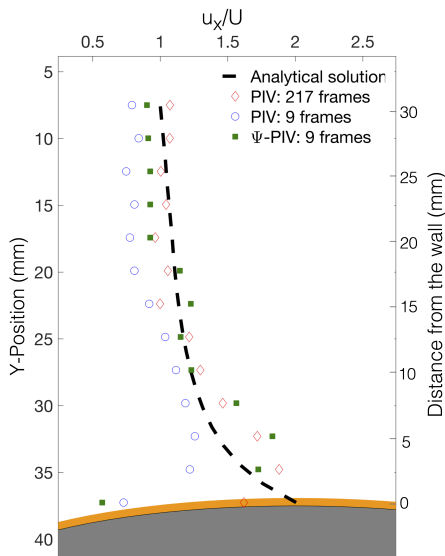
Figure 2.11: Measured velocity distribution (marked as the rectangular domain in Fig. 2.10) from PIV, Ψ-PIV next to the cylinder and compared with the theoretical distribution which is calculated assuming ideal flow conditions. The yellow band represents the region where the Hele-Shaw approximation is not valid ($l \approx h$).

insufficient for correlation-averaging. On the central lower side of the 2D cylinder (see Fig. 2.10b) the flow does not increase and the measurement is inaccurate as a result of cross-correlation among non-corresponding particle-image pairs. This is a typical problem with micro-PIV measurements at insufficient image density. Fig. 2.10c presents the velocity field constructed from the same measurement data and using our Ψ-PIV algorithm with 9 frames. The measurements are in close agreement with the PIV results obtained from a correlation-average over 217 frame-pairs (Fig. 2.10a). The velocity field measurement can be compared with the analytical solution for the flow around a cylinder expected from potential flow theory. Fig. 2.11 reports the theoretical velocity field in the *x*-direction at increasing distance from the cylinder surface along the *y*-axis and the corresponding measured data using PIV and Ψ-PIV. The theoretical solution imposes a no-penetration boundary condition at the surface of the cylinder and allows for a slip velocity. The velocity on the surface of the cylinder along the *x*-axis (see Fig. 3.1) increases to a velocity $u_x = 2U$ at the equator of the cylinder. The PIV result for correlation-averaging over 217 frames shows that the velocity field is in close agreement with the analytical solution except near the surface of the cylinder. Close to the surface, the velocity decreases because the Hele-Shaw condition is no longer appropriate near the wall and the potential flow solution does not hold because of the no-slip boundary condition. The PIV result for correlation-averaging over 9 frames clearly under-predicts the flow field due to the low effective image density. It should be noted that the measured free stream velocity for PIV with 9 frames is less compared to PIV data with 217 frames. This is because, with fewer frames, particles that are attached to the wall significantly contribute to the underestimation of the velocity field. Near the surface of the

CHAPTER 2

Figure 2.12: Comparison between the PIV and Ψ-PIV algorithms with RMS error as a function of number of frames (marked as the rectangular domain in Fig. 2.10). A solid line of PIV results for 217 frames is also shown to characterize the minimum measurement error with respect to the reference velocity. The reference velocity is computed analytically using potential flow theory.
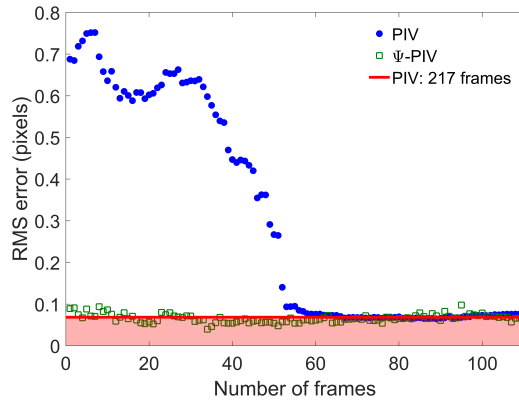
cylinder, the velocity measured from conventional PIV with correlation-averaging over 9 frames is largely erroneous with a difference of up to 37%, owing to the large in-plane displacement and displacement gradient. The Ψ-PIV result for correlation-averaging over 9 frames is in agreement with the PIV result for 217 frames. For Ψ-PIV, the difference in measured velocity with respect to the reference velocity is of approximately 8% throughout the velocity distribution. Ψ-PIV substantially reduces the requirement in the number of frames necessary for the correlation-averaging to reach the desired accuracy. The accuracy of Ψ-PIV is reported in Fig. 2.12 which displays the root-mean square error (RMS error) of the measured velocity data using PIV and Ψ-PIV in the x-direction at increasing distance from the cylinder surface along the y-axis (marked as the rectangular domain in Fig. 2.10). For a particle displacement of 8-10 pixels, PIV with 217 frames has a measurement error of 0.05 pixels or 0.5% of the measured displacement. The RMS error for PIV reaches 0.05 pixels for the correlation averaging of 70 frames and remains constant thereafter. With fewer frames, the RMS error of Ψ-PIV is small compared to PIV, because the flow direction can be determined from the ensemble correlation averaging of fewer frames. The Ψ-PIV algorithm reaches a RMS error of 0.05 pixels for the correlation-averaging of 9 frames and subsequently remains stable. Thus, for the same PIV dataset, the results from the Ψ-PIV algorithm converges with fewer frames (8 times fewer frames in this experiment) compared to the PIV algorithm. Both the algorithms use a single-pass cross-correlation to present the underlying difference between the two approaches.

## 2.5 UNSTEADY FLOW AROUND A DEVELOPING RANKINE HALF-BODY

2.5.1 EXPERIMENTAL SETUP

The performance of the Ψ-PIV algorithm is characterized for unsteady flow in a Hele-Shaw cell. In this second experiment, the Hele-Shaw cell has dimension $l = 60$ mm and $w = 15$ mm. The height of the channel $h = 350$ μm. The flow channel was made of PDMS using standard microfabrication techniques [88], and the PDMS layer was bonded to a glass cover-slip using plasma oxidation. The pressure pumps (Fluigent) were used to generate a uniform inflow with a centerline velocity $\mathbf{u} = (0.2$ mm/s, 0). A Rankine half-body is generated in the channel through an additional inlet located at the middle of the channel; see Fig. 2.13. Standard PTFE Teflon tubing with 1/16" outer diameter and 1/32" inner diameter were used to connect the Hele-Shaw cell and the pressure pump reservoir. Polystyrene microspheres with a mean diameter of 20-27 μm (Cospheric) were used as tracer particles. Images were recorded with a CCD camera with similar specifications as mentioned in section 2.4.1. The camera was equipped with a Nikon objective with a 200 mm focal length, a magnification factor of 0.80 and an f-stop of 8. The computed depth-of-field was 0.8 mm, which ensured that all particles within the channel were in focus. The depth-of-correlation DOC is 1.7 mm. The acquisition frequency was 9.8 Hz corresponding to an average in-plane displacement of 2-3 pixels between two consecutive recordings. An unsteady flow is generated in the channel, that corresponds to the following sequence: (1) a uniform flow from t = 0 seconds to t = 74.4 seconds, (2) a developing Rankine half-body from t = 74.5 seconds to t = 77.6 seconds due to an increasing volumetric flow rate through inlet 1, (3) the flow around a developed Rankine half-body generated by a volumetric flow rate $Q_1 = 0.4$ ml/min at the inlet 1 from t = 77.7 seconds to t = 240 seconds. The time interval between t = 66 seconds and t = 80.5 seconds is focused on. This is the time interval where the flow gradually develops from uniform flow to a fully developed Rankine half-body. The image processing was done using interrogation windows of 32×32 pixel with 0% overlap.A moving average filter in time over 9 frames is used to find the local minimum intensity value. This was subtracted from each frame, which effectively removes the background.

2.5.2 EXPERIMENTAL RESULT

Fig. 2.14 compares the streamlines obtained for the same experimental recording and using the velocity field obtained (1) from PIV using correlation-averaging over 100 frames (Fig. 2.14a,b,c), (2) from PIV using correlation-averaging over 3 frames (Fig. 2.14d,e,f) and (3) from Ψ-PIV using correlation-averaging over 3 frames (Fig. 2.14g,h,i). Fig. 2.15 compares the unsteady velocity measured at a given point using conventional PIV and Ψ-PIV. The experimental results are compared with

Figure 2.13: Experimental test setup with all the crucial components. On the bottom left corner, the schematic of the Hele-Shaw cell (l = 60 mm, w = 15 mm, h = 350 μm) is shown. The schematic shows the inflow from the inlet hole with volumetric flow rate Q to yield a uniform flow along the transverse direction of the cell and volumetric flow rate Q_1 shows the inflow in the longitudinal axis. The two additional inlet holes marked as inlet 1 and 2 can be used to generate a source or a sink.
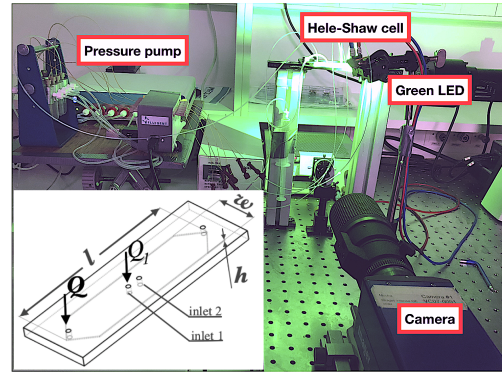
the analytical solution at the location marked as ,x, in the flow domain (Fig. 2.14). From potential flow theory, the velocity was calculated using a superposition of uniform flow and a single source. Similar to the experimental data, the analytical solution (see dashed line curve in Fig. 2.15) was kept as a uniform flow for the first 74.4 seconds (*i.e.* frames 1-80). The Rankine half-body was developed by increasing the strength of the source from t= 74.5 seconds to 77.6 seconds (*i.e.* frames 81 - 110), and thereafter the source strength remains constant until the end of the measurement at t= 80.5 seconds (*i.e.* frames 111 - 140). At time t = 66 seconds (frame 1), the uniform flow is captured well by PIV with correlation-averaging over 100 frames (Fig. 2.14a). At t = 75.5 seconds (frame 90), although the streamlines are continuous, they do not correspond to the true flow behavior. This is because the temporal resolution is lost due to large number of frames required for the correlation-averaging. In our experiments, a full Rankine half-body develops in 3 seconds, but the PIV results shown in Fig. 2.14b take the temporal information of 10.2 seconds to have enough effective seeding density to find the velocity vectors. Here the PIV result is similar to the PIV result of a fully developed Rankine half-body (see, Fig. 2.14c) because the PIV, in this case, takes particle image information starting from 75.5 seconds (frame 90) to 83.7 seconds (frame 171). This means the correlation-averaging also takes 70% of the particle image information from the fully developed Rankine half-body. At t = 78.5 seconds (frame 120), Fig. 2.14c shows a fully developed Rankine half-body that also corresponds to the actual flow because the flow around the developed Rankine half-body is steady for the entire experiment. The velocity field measurement for correlation-averaging over 100 frames have low random error but this leads to a notable loss of temporal information and thus PIV is not able to capture the gradual change in the flow rate as the Rankine half-body is developing in the flow field. This can be distinctly seen in Fig. 2.15 from the significant deviation between the PIV measurements and the theoretical solution. Fig. 2.14d,e,f show the streamlines using PIV velocity fields computed from correlation-averaging over 3 frames. These streamlines are discontinuous and in some cases break mid-way. This shows that the velocity vectors are erroneous due to lower effective image density. The development of the
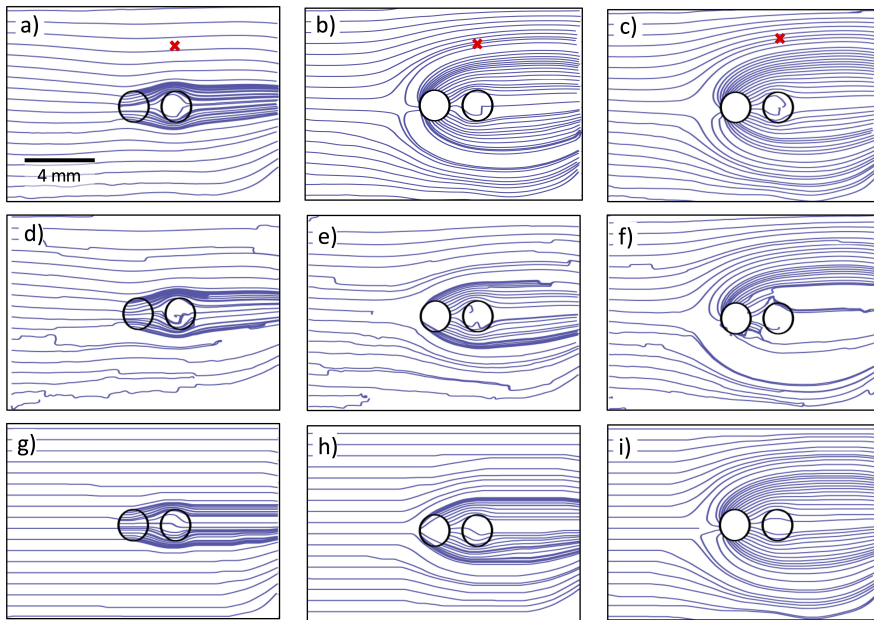
Figure 2.14: Images of flow around the development of Rankine half-body: (a), (b), (c) corresponds to PIV results from correlation-averaging of 100 frames at the measurement time of 66, 75.5 and 78.5 seconds respectively. (d), (e), (f) corresponds to the results from correlation-averaging of 3 frames using conventional PIV. (g), (h), (i) shows the result Ψ-PIV for the correlation-averaging of 3 frames at the measurement time mentioned above. The ,x, mark in (a), (b) and (c) depicts the arbitrarily chosen position which would be used in Fig. 2.15 for quantitative analysis. The velocity direction is from left to right. The flow appears to separate along the boundary of the downstream hole. This obstruction is caused by the tubing, which touched the bottom surface of the Hele-Shaw cell.

Rankine half-body becomes visible from the streamlines in Fig. 2.14e, even though the measured velocity field is inaccurate. For Ψ-PIV with correlation-averaging over 3 frames, the streamlines before (at t= 66 s; frame 1) and after (at t= 78.5 s; frame 120) the fully developed Rankine (see Fig. 2.14g,h) are in agreement with the streamline results of PIV with correlation-averaging over 100 frames (see Fig. 2.14a,c). At t= 75.5 seconds (frame 90), the on-set of the Rankine half-body is clearly visible from the streamlines in Fig. 2.14h. In this case, Ψ-PIV has a temporal resolution of 0.3 seconds with enough effective seeding density to capture the gradual change in the flow field. The velocity estimated using Ψ-PIV are in close agreement with the theoretical solution as the Rankine half-body develops *i.e.* from frames 81 - 110; see Fig. 2.15. For Ψ-PIV, the velocity slightly overshoots the theoretical velocity value for frames 111-130. This may be either due to the control response of the flow rate sensor for the pressure pump or due to a spurious direction vector from the Ψ-PIV algorithm or a combination of both. From frame

Figure 2.15: Velocity measured at the ,x, mark shown in the previous figure. The figure shows the time history of flow as uniform flow (at t = 66 seconds: frame 1) transitioning into a fully developed Rankine half-body (at t = 77.6 seconds: frame 110). PIV and Ψ-PIV results are compared with the theoretical solution which is calculated assuming ideal flow conditions.
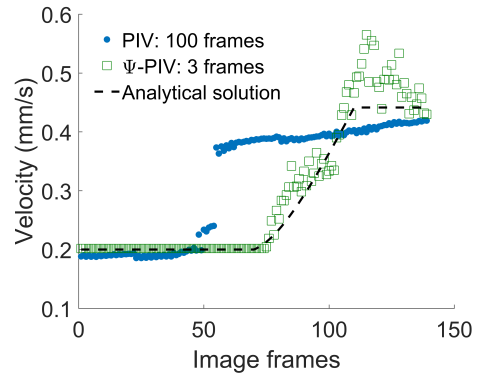
131 onward, the results from Ψ-PIV are again in agreement with the theoretical result.

2.6 DISCUSSION

The valid detection probability ϕ of synthetic data as a function of effective image density N_{eff} shows that a higher signal-to-noise ratio SNR can be achieved by Ψ-PIV compared to conventional PIV. Ψ-PIV attains $\phi = 0.95$ at $N_{\text{eff}} = 15$; see Fig. 2.5. For $\phi \geq 95\%$, the minimum effective image density represented by the Ψ-PIV algorithm is less than half compared to the valid detection probability analysis of tracer particles spread uniformly across the channel height using PIV as shown by Ehyaei *et. al.* [72]. Fig. 2.11 displays a comparison between PIV and Ψ-PIV result for the experiment of flow around a 2D cylinder in a Hele-Shaw cell. The Ψ-PIV result for correlation-averaging over 9 frames is in close agreement with the PIV result for correlation-averaging over 217 frames. Thus, the temporal resolution of Ψ-PIV increases by a factor of 25 compared to conventional PIV. Fig. 2.15 shows that for an unsteady flow, conventional PIV is unable to measure the velocity accurately because correlation-averaging is required over a large number of frames corresponding to a time interval greater than the time scale of the flow. This makes it very challenging to measure the flow field using conventional PIV for unsteady flows. For such flows, Ψ-PIV can obtain higher temporal information compared to conventional PIV for the same number of frames; see Fig. 2.15. Although Ψ-PIV is an improvement over the current correlation-averaging technique, it still requires an effective image density of around 20 particle image pairs. This means that the average effective seeding density needs to be around 20 particle image pairs in 32×32 pixels interrogation window to deduce the velocity field from the directional-correlation over two consecutive frames. If the image density N_I is lower than 20, then the correlation-averaging over a few frames is required to reach effective image density ($N_{\text{eff}} = N_F N_I F_I F_\Delta$) of 20.

2.7 CONCLUSION

This chapter describes a new algorithm to determine the velocity fields in a Hele-Shaw cell. This method reduces the minimum required effective image density ($N_{\text{eff}} = N_F N_I F_I F_\Delta$) compared to the conventional micro-PIV technique using correlation-averaging. This increases the temporal resolution that can be achieved by Ψ-PIV compared to conventional PIV. Ψ-PIV is therefore attractive to measure unsteady flows for microfluidic applications. The major difference lies in the fact that Ψ-PIV requires a lower image density to determine the flow direction for each interrogation window compared to the conventional method. Once the flow direction is determined, the two dimensional stream function is used to extract and reconstruct the magnitude of the velocity field. Synthetic image evaluation for uniform particle concentration shows that an effective image density of 20 particle image pair is satisfactory to measure the velocity field. This is 5 times lower compared to the required image density in the measurement of the velocity gradient within the correlation-depth [72]. For steady measurement case of the flow around a 2D cylinder in a Hele-Shaw cell, the Ψ-PIV algorithm using correlation-averaging over 9 frames, yields similar results as the PIV algorithm using over 70 frames for the single cross-correlation approach. Moreover, experiment results of a developing Rankine half-body for Ψ-PIV can reach significantly higher temporal resolution. This reduction in the number of frames for the correlation-averaging in Ψ-PIV would enable a substantial improvement of the temporal resolution in case of time-varying microfluidic flows. In addition, the minimum image density required to determine the direction field could be further improved with the use of advanced PIV processing steps such as multi-grid and iterative windows approach [89].

CHAPTER 2

PARTICLE MANIPULATION

The manipulation of particles and droplets has applications in diverse fields of engineering. Generally, manipulation activities are realized in microdevices which have a fixed design tailored to a specific task, making multiple analyses of a wide range of specimen- from biological to chemical specimens unfeasible on a single device. We designed a Hele-Shaw flow cell with "virtual channels" to address this issue. In our device, uniform flow in the flow chamber and three inlets perpendicular to the flow chamber are used to manipulate particle. These three inlets can inject or extract fluid in the flow cell to deviate the streamlines. This device allows us to integrate multiple functionalities such as particle trapping and separation onto a single device. Since the depth-averaged velocity over the channel in a Hele-Shaw cell is irrotational, we use potential flow theory to predict the flow field for manipulating particles. The linearity of potential flow theory is ideally suited to the fast computation times required by our application. In this chapter, a Hele-Shaw cell is characterized for particle manipulation applications. An optimized particle trajectory is determined a priori using an optimization routine which calculates a particle trajectory that has small flow rate bounds and least variation in the flow rate from the pump. This optimization routine is called as a priori particle manipulation algorithm. The results in this chapter show that the experimentally determined particle trajectories in this device are in close agreement with the trajectories computed with the a priori particle manipulation algorithm, which relies on the potential flow simulations.

This chapter is part of the manuscript to be submitted

3.1   INTRODUCTION

A microfluidic device functionality relies on elementary microfluidic manipulations, such as identification, selection, separation, and mixing of particles, biological or chemical specimens. These manipulations of particles have been achieved in microfluidics by developing various passive techniques such as micro-channel geometry and active techniques using laser fields, magnetic fields, acoustic forces, electrical fields, artificial cilia, and hydrodynamic forces, as discussed previously in section 1.3.

A significant challenge in particle manipulation activity is to develop a versatile device that has a generic, simple design and is capable of carrying out various tasks. Such a device could benefit from *a priori* particle manipulation algorithm that provides a user the ability to integrate multiple functionalities such as trapping, separation, or sorting onto a single device. In the early prototyping design phase, such a device is beneficial to see which type of micro-channel geometry is best suited for the desired application.

Our previous work in particle manipulation in a macroscopic Hele-Shaw cell (300×100×0.5 mm) [48] and in a circular device (10×0.36 mm) [49] to manipulate particle trajectories using streamlines were a starting point to develop further a microfluidic device that uses the hydrodynamic streamlines to manipulate particles under the influence of uniform flow using sources (inject fluid) and sinks (extract fluid).

In this chapter, a Hele-Shaw flow cell is designed that has "virtual channels". The "virtual channels" are generated with a uniform flow in the flow chamber and three inlets[1] perpendicular to the flow chamber. An *a priori* particle manipulation algorithm is developed to determine the optimized particle trajectories while confining the flow rate bounds and the variation in the flow rate of the inlets/outlets. In the present device, three inlets are used to either inject or extract fluid in the flow cell to modify the streamlines in the device. Since the depth-averaged velocity over the channel in a Hele-Shaw cell is irrotational, the potential flow theory is used to predict the flow field for manipulating particles. Different test cases demonstrate the potential of the device: single-particle trapping, single-particle trajectory deflection, separation of a particle pair, two particles coming close to each other, and interchanging the position of two particles. These test cases demonstrate the ability of this device to perform elementary microfluidic manipulations. The results show that the experimentally determined particle trajectories and flow rates agree with the corresponding pre-computed values using the *a priroi* particle manipulation algorithm.

The design and validation of the flow cell and essential components of the experimental setup are explained in section 3.2. In section 3.3, the flow rate input and the time response of the pump for the device are characterized, which helps to

---

[1]Please note that in this thesis, the word 'inlet' is used to refer the aperture of the microfluidic device. The word 'inlet' is used interchangeably for both inlet and outlet, where the outlet is defined as an inlet with a negative flow rate.

mitigate the bias error from the pump response time. The particle manipulation algorithm is detailed in section 3.4. In section 3.5, the results from the experiments for various test cases are presented and compared to the experimentally measured particle trajectories from the optimized particle trajectories. The performance and limitations of using pre-computed optimized particle trajectories and the potential benefits of implementing a feedback loop to calculate the flow rate corrections based on particle position are discussed in section 3.6.

3.2 EXPERIMENT OVERVIEW AND FLOW CELL DESIGN VALIDATION

3.2.1 EXPERIMENTAL SETUP

A schematic of all the essential components for the experiment is displayed in Fig. 3.1B. The setup consists of a pressure pump that regulates the pressure in 5 pressure ports. A pressure pump (Fluigent MFCS-EZ) generates the desired flow rate. These ports are connected to 5 reservoirs that contain the working fluid. The working fluid used in all the experiments is deionized (DI) water. These five reservoirs are connected to a flow sensor that measures the volumetric flow rates, Q_i, where i corresponds to the inlets as shown in Fig. 3.1B. For reservoir 4, an additional reservoir 4^* is connected to the device further downstream of the flow sensor. This is done to avoid any contamination and clogging of the capillaries in the flow sensor from the particles to be manipulated. Polystyrene fluorescent microspheres (density: 1gm/cc) with a mean diameter of 212 μm (Cospheric) were used as the target particles. At the final outlet corresponding to the fifth reservoir, a back pressure of 25 mbars was imposed to allow net-negative flow. The Hele-Shaw cell (l= 40 mm, w= 12 mm, and h= 350 μm) in Fig. 3.1D was 3D printed from clear resin using a FORM 3 3D printer. Images were recorded with a sCMOS camera (PCO) with a pixel pitch of 6.5 μm. The camera was mounted on a microscope (Nikon Eclipse Ti) with a 1x objective. The acquisition frequency was 5 Hz corresponding to an average in-plane displacement of 4-6 pixels between two consecutive recordings. The coordinates of the particles during the experiment are acquired using an in-house developed LabVIEW program which is used to acquire the images.

Simultaneous manipulation of N particles requires a minimum of 2N+1 inlets, where N is the number of particles (2N for movement in x- and y-position and an additional channel satisfying mass conservation [55]). Thus, for n=2, at least five (5) ports are required. A schematic of the microfluidic device, which has an inlet for continuous uniform flow, three holes to inject/extract fluid, and an outlet is illustrated in Fig. 3.1C. We consider the laminar flow, **u**, between the two parallel plates, i.e., a Hele-Shaw flow [90]. The details of the Hele-Shaw flow are discussed in detail in section 1.5.
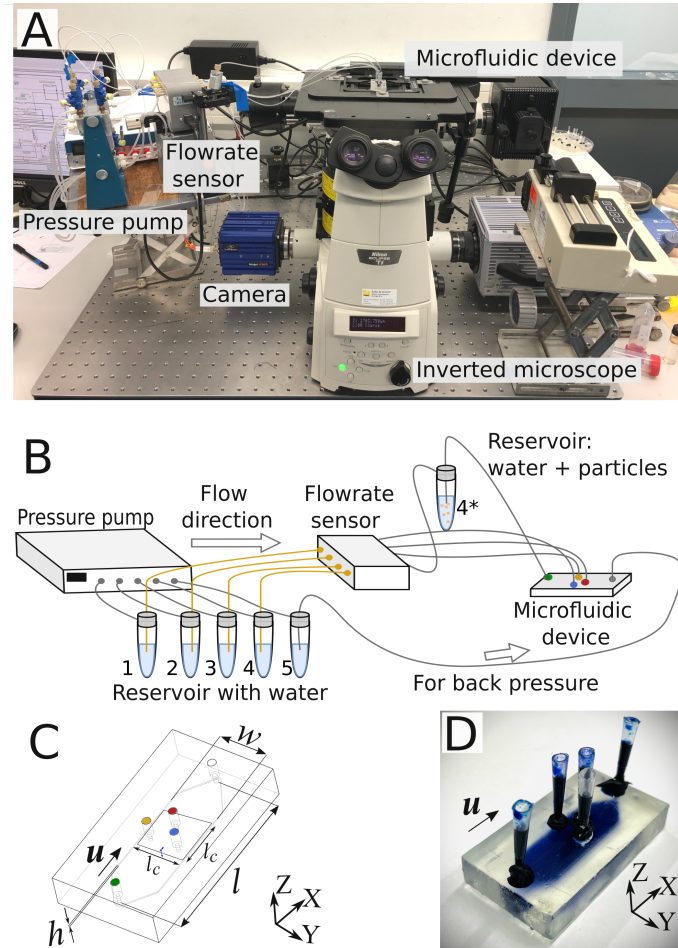
Figure 3.1: (A) Experimental setup with all the required components. (B) Schematic of the experimental setup shows the microfluidic device connected with reservoirs connected to a flow rate sensor. A pressure pump drives the fluid through the reservoir using pressurized air. Reservoir 1, 2, and 3 correspond to inlet 1, 2, and 3, respectively. Reservoir 4 is connected to an addition reservoir 4^* containing particle solution. Reservoir 4^* is connected to the uniform flow inlet. Reservoir 5 is attached to the outlet of the microfluidic device. The flow is regulated using an in-house developed LabVIEW program. (C) Schematic of the microfluidic device with the channel length l, width w and height h. The uniform flow is denoted as **u**. The flow is parabolic over the channel height in the z-direction. The circles represents uniform flow inlet (•), inlet 1 (•), inlet 2 (•) and inlet 3 (•). The region of interest, where particle manipulation is performed, is a square region denoted by l_c. (D) The actual 3D printed microfluidic device is filled with methylene blue-water solution for better visualization of the flow channel.

The Hele-Shaw condition is valid when the in-plane length of the flow domain l is much larger than the channel height h, i.e., $l \gg h$. The velocity profile is parabolic in the wall-normal direction (z-direction), and is proportional to the pressure field p satisfying Laplace's equation [91]. The two in-plane velocity components $\mathbf{u} = (u,v)$ in the (X, Y) plane can be described as a potential flow except near the obstacles where the distance to the object becomes of the order of the plate distance h. The no-slip boundary condition is imposed at the surface of the obstacle instead of the tangential-flow slip condition for an ideal flow. As the Laplace equation is linear, the superposition of any known potential flow solutions provides another valid solution. Hence, complicated flow patterns can be represented by the superposition of basic flow patterns.

3.2.2 NON-DIMENSIONALIZATION OF THE FLOW CELL

All length scales are non-dimensionalized using the region of interest characteristic length scale, $l_c = 12$ mm as shown in Fig. 3.1C. The characteristic time scale t_c is calculated from the characteristic uniform flow $\mathbf{u_c} = (u_c, 0)$ and the characteristic length scale l_c i.e $t_c = l_c / \mathbf{u_c}$. A non-dimensional uniform flow $\mathbf{u^*} = (u^*, 0)$ is defined by the user. The non-dimensional parameters are defined as follows:

$$X^* = \frac{X}{l_c}, \qquad Y^* = \frac{Y}{l_c}, \qquad Z^* = \frac{Z}{l_c} \qquad (3.1)$$

$$l^* = \frac{l}{l_c}, \qquad h^* = \frac{h}{l_c}, \qquad w^* = \frac{w}{l_c}, \qquad Q^* = \frac{Q}{l_c^2} \cdot \frac{u^*}{u_c} \qquad (3.2)$$

Here, X, Y and Z are dimensional axes, X^*, Y^* and Z^* are non-dimensional axes, l, w and h are dimensional length, width and height of the flow cell respectively. l^*, w^* and h^* are non-dimensional length, width and height of the flow cell respectively. $Q = [Q_1, Q_2, Q_3]$ are dimensional flow rates corresponding to inlet 1, 2 and 3 respectively. $Q^* = [Q_1^*, Q_2^*, Q_3^*]$ are non-dimensional flow rates corresponding to inlet 1, 2 and 3 respectively. The non-dimesionalized parameters of the flow cell is used extensively in the calculation of the optimized particle trajectory using the *a priori* particle manipulation algorithm discussed in section 3.4.

3.2.3 SOURCE-BASED PANEL METHOD

The aft-part of the microfluidic device is modeled using a discrete source-based panel method [92] to compute the approximate solution for the resultant pressure forces acting at the surface of the device. The panel method is a well-known potential flow solver mainly used to analyze flow fields for geometries, such as the flow around an airfoil or the flow around a cylinder. As the potential flow satisfies the Laplace equation, $\nabla^2 \Phi = 0$, where Φ is the potential function, the solution can be constructed as the linear superposition of flow elements such as an irrotational

vortex, a doublet, a source or a sink to create more complex flows. This method is used to determine the flow around an arbitrarily shaped body in a two- or three-dimensional domain with a no-penetration boundary condition on the surface. The no-penetration boundary condition is imposed at locations on the surface called the collocation points. The panel method reconstructs the solution as a superposition of the flow element distributed on the boundary of the domain. The panel method is a numerical approximation based on dividing the object into several finite segments called panels. A flow element such as a vortex, doublet, source or sink is prescribed to the panels. The boundary condition can only be solved for the collocation point of each panel as long as the panels are made to be reasonably small.

In the current work, a 2D discrete source-based panel method [92] is used to solve the potential flow equation that determines the flow pattern in the aft-part of the flow cell. The flow cell wall is divided into panels, and a collocation point is located at the center of each panel. The source points with unknown strength σ are located outside the flow cell wall at a unit length offset from the location of the collocation point as shown in Fig. 3.2. In potential flow theory, the complex potential, $w(z)$, due to a single source is given by:

$$w = \Phi + \Psi i \tag{3.3}$$

where z is a complex variable,

$$z = x + yi \tag{3.4}$$

such that the velocity induced due to the source element can be written in complex form as:

$$\frac{dw}{dz} = U - iV \tag{3.5}$$

Here, Φ is the potential function defined as $\Phi = \frac{\sigma}{2\pi} ln\sqrt{x^2 + y^2}$, Ψ is the stream function defiend as $\Psi = \sigma \tan^{-1}\frac{y}{x}$, σ represents the source strength or the flow rate per unit depth, and (x,y) is the field point of interest.

The influence coefficient a_{ij} is defined as the self-induced velocity component normal to the surface of a unit strength source j ($\sigma_j=1$) at each collocation point i. At collocation point $i = 1$, it can be written as:

$$a_{1j} = (U, V)_{1j} \cdot \boldsymbol{n_1} \tag{3.6}$$

The no-penetration boundary condition on the velocity component normal to the surface of the panel at each collocation point is imposed as zero velocity. In this case, the known components are a uniform flow coming from left to right, three inlets, and an outlet as marked in Fig.3.2. The known components are transferred to the right-hand side RHS of the equation as shown below:

$$RHS_i = -((u^*, 0) \cdot \boldsymbol{n_i} + \sum_{k=1}^{3} (U_k, V_k)_{ij} \cdot \boldsymbol{n_i} + (U_{\text{outlet}}, V_{\text{outlet}})_{ij} \cdot \boldsymbol{n_i}) \tag{3.7}$$
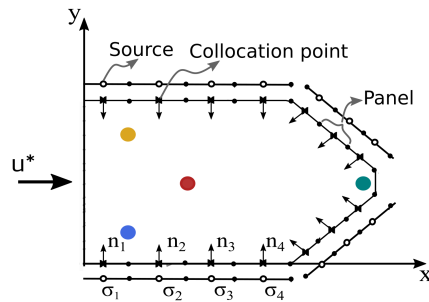
Figure 3.2: The aft part of the flow cell walls is divided into panels. A collocation point marked as **x** is located at the midpoint of each panel with normal vector, **n**. On the outer periphery of the wall, sources σ are located corresponding to each collocation points. The circles on the microfluidic device represents inlet 1 (●), inlet 2 (●), inlet 3 (●) and outlet (●). The uniform flow, u^*, direction is from left to right.

Here, i and j represent collocation point and source point locations respectively. Influence coefficient and RHS can be written for each of the collocation points using equation 3.6 and equation 3.7 and a set of algebraic equations are obtained:

$$\begin{pmatrix} a_{11} & a_{12} & \cdots & a_{1n} \\ a_{21} & a_{22} & \cdots & a_{2n} \\ \vdots & \vdots & \ddots & \vdots \\ a_{n1} & a_{n2} & \cdots & a_{nn} \end{pmatrix} \begin{pmatrix} \sigma_1 \\ \sigma_2 \\ \vdots \\ \sigma_n \end{pmatrix} = \begin{pmatrix} RHS_1 \\ RHS_2 \\ \vdots \\ RHS_n \end{pmatrix} \tag{3.8}$$

The unknown source strengths σ in equation 3.8 are calculated by using standard techniques of linear algebra. Thus at each panel, the calculated source strength enforces zero velocity at the collocation point normal to the panel.
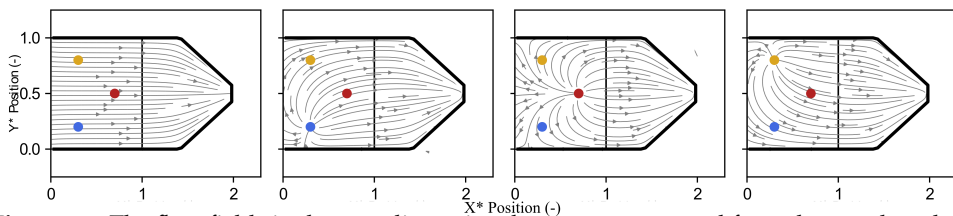
Figure 3.3: The flow fields in the non-dimensional state are computed from the panel method where all the flow components are zero except (A) uniform flow, (B) inlet 1, (C) inlet 2, and (D) inlet 3. All the flow components in the test cases mentioned above have a unit input. The measurement domain is marked by the black square box.

The performance of the numerical approach is evaluated by computing four elementary flows within the flow cell, see Figure 3.3. The four elementary flows are the uniform flow velocity over the flow cell and the flow injection (a source)

through inlet 1, 2, and 3. Since all the flows to be controlled are linear combinations of these four flows, pre-computing these four elementary flows and superposing them makes the computations faster. Test case 1 shows the flow field ($u_0 = (u_0, v_0)$) with contribution to all the three inlets as zero except the uniform flow u^* [Fig.3.3A]. Test case 2 shows the flow field ($u_1 = (u_1, v_1)$) where the uniform flow u^* is zero, inlet 1 acts as a source, and zero flow in inlet 2 and inlet 3 [Fig.3.3B]. Test case 3 shows the flow field ($u_2 = (u_2, v_2)$) where the uniform flow u^* is zero, inlet 2 is a source, and no flow comes through inlet 1 and the inlet 3 [Fig.3.3C]. Test case 4 shows the flow field ($u_3 = (u_3, v_3)$) where the uniform flow u^* is zero, inlet 3 is a source, and no flow comes through inlet 1 and the inlet 2 [Fig.3.3D]. It is noteworthy that, because of the linearity of the governing equation, all the flow fields relevant in this flow cell can be written as a linear combination of these four elementary flow fields. With these four test cases any complex flow field ($u_{new} = (u_{new}, v_{new})$) can be created by super-positioning the flow fields as long as the flow cell geometry is not changed.

$$u_{new} = u^* \cdot h^* \cdot w^* \cdot u_0 + Q_1^* \cdot u_1 + Q_2^* \cdot u_2 + Q_3^* \cdot u_3 \qquad (3.9)$$

where u^*, Q_1^*, Q_2^* and Q_3^* are the imposed non-dimensional uniform flow, flow rates at inlet 1, 2 and 3 respectively. During experiments, the upstream uniform flow is kept constant, and only Q_1^*, Q_2^* and Q_3^* are used to modulate the flow field, and in turn, to manipulate the particle.

A simple investigation is carried out for a steady-state test case to verify that the velocity flow field computed directly from the panel method solver is equal to the flow field computed using the superposition of the elementary solutions. Ideally, the computed flow field from the former and the latter method should be identical. A flow field is generated using a panel method solver with arbitrarily chosen non-dimensional values of uniform flow, $u^*= 1$. The inlet 1, 2 and 3 have arbitrary flow rate value as $Q_1^*= 0.05$, $Q_2^*= \text{-}0.02$, $Q_3^*= 0.03$ respectively as shown in Fig.3.4a. Another flow field shown in Fig.3.4b is generated using the superposition of elementary solution, using the equation 3.9 where the above-mentioned arbitrary values are multiplied to their respective reference flow field. Qualitatively both the flow fields in Fig.3.4 look identical, and quantitatively their difference is zero as expected. Using equation 3.9 for computing the flow field during the optimization process makes the *a priori* particle manipulation algorithm (discussed in section 3.4) faster, as it does not have to recalculate the flow field every time in the intermediate step of the algorithm. Instead, a simple linear calculation determines the flow field.

3.2.4   COMSOL SIMULATION

A 3D viscous flow solver, COMSOL, is used to compare the panel method solution (based on 2D inviscid potential flow) in section 3.2.5 with experimental data. In this section, the numerical characteristics of the COMSOL simulations are discussed.
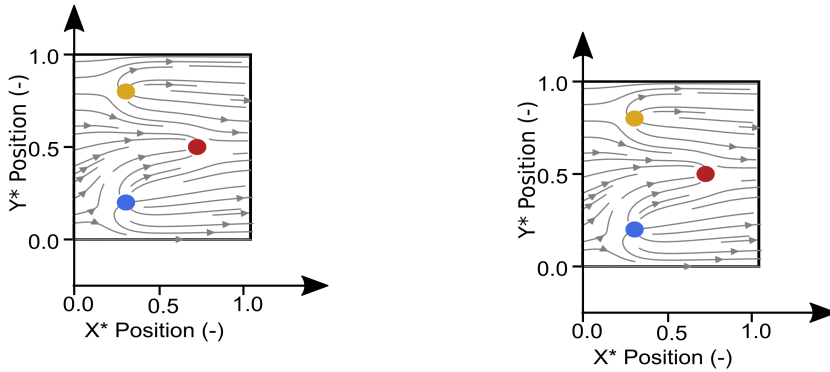
(a) Panel method solution with arbitrary input of 1, 0.05, -0.02, and 0.03 for uniform flow, inlets 1, 2, and 3, respectively. This solution is obtained by solving the equation 3.8.

(b) The flow field is created by multiplying flow field with unit input [refer Fig. 3.3] and the arbitrary value of 1, 0.05, -0.02, and 0.03 for uniform flow, inlets 1, 2, and 3, respectively. The result is obtained from equation 3.9.

Figure 3.4: Potential flow solution using the superposition principle.

The 3D flow inside the flow cell was simulated using the "Laminar Flow" module of COMSOL. The flow cell was oriented with the channel height along the positive z-direction as shown in Fig. 3.5A. A flow rate, $Q_{\text{uniform flow}} = 20\ \mu l/\text{min}$ at the uniform flow inlet was imposed through the boundary SS' as shown in Fig. 3.5A, such that when the channel width w is constant, the uniform flow at the center-line along the z-direction of the flow cell corresponds to $\mathbf{u} = (80,0)\ \mu m/s$. At inlet 2, a flow rate $Q_2 = 110\ \mu l/\text{min}$ is imposed through the boundary SS'. The outlet is used to draw out the fluid such that the mass conservation is maintained. A no-slip boundary condition on all the internal surfaces is imposed. The flow field with streamlines for the scenario with the above-mentioned flow rates is shown in Fig. 3.5B. In the COMSOL simulation, the flow cell geometry is meshed using a "physics-controlled" mesh. The mesh is refined to improve the stagnation point location accuracy and the numerical convergence of the analysis. The mesh independence study is carried out for four different mesh sizes to determine the position of the stagnation point. By taking the stagnation point location as the reference variable, see Fig. 3.5C, the difference between the last two results is less than 3%. Thus, the third mesh size, which corresponds to the element size option of "finer" in COMSOL, was used for further analysis to minimize computational cost. It results in a maximum element size of 2.56 mm and a minimum element size of 0.19 mm based on the flow cell geometry.

3.2.5   FLOW MODEL VALIDATION

To validate the source-based potential flow model, the flow fields computed with the panel method are compared with the flow field computed with COMSOL

---

[1] Psi-PIV is described in Chapter 2
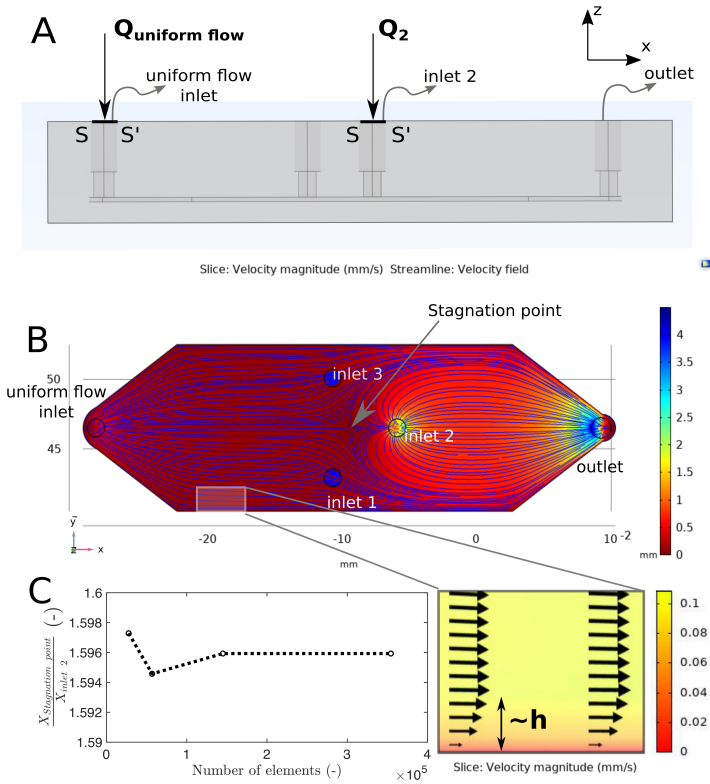
Figure 3.5: (A) Side view of the CAED design flow cell. The flow rate is imposed over the inlet at the top of the flow cell, marked as the SS' line. (B) COMSOL result: Velocity contour plot with streamlines (in blue) when the flow rate at uniform flow inlet, $Q_{\text{uniform flow}}$ = 20 μl/min and the flow rate at inlet 2, Q_2 = 110 μl/min. An upstream location on the flow cell is zoomed in to show that the Hele-Shaw condition does not apply close to the walls of the cell. The velocity contour plot is re-scaled to show the velocity field near the wall clearly. The Hele-Shaw condition is violated at an in-plane distance of h from the boundary of the flow domain. (C) Mesh independence study concerning the stagnation point location.

simulations. The two numerically calculated flow fields are further compared with the flow fields measured experimentally. The potential flow model is validated by comparing the position of a stagnation point induced by a single source in a uniform flow. We chose to measure the spatial location of the stagnation point in the flow chamber because stagnation points are inherently unstable, and their location can notably differ based on the interaction of the fluid with the walls of the flow cell and inlet locations. Suppose the stagnation point from the panel method does not deviate when compared to COMSOL simulations and experiments. In that case, it shows that the flow field computed by the panel method is a reasonably accurate representation of the actual flow field. The
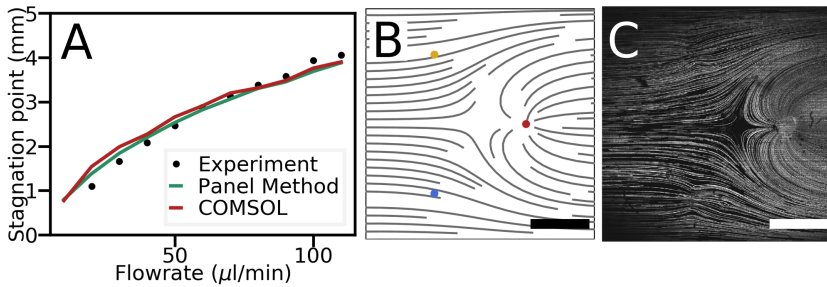
Figure 3.6: (A) Comparing the source-based panel method, COMSOL simulations, and experiments to characterize the device by comparing the stagnation point of the Rankine half-body. The Rankine half-body strength was regulated by keeping the uniform flow constant and gradually increasing the flow rate through inlet 2 (marked as a red circle). (B) and (C) shows a test case, where the flow rate at the upstream inlet is 20 μl/min and at inlet 2 is 50 μl/min from experiment and source-based panel method, respectively. The scale bar represents 4 mm.

stagnation point from the experimental data set is determined using Psi-PIV[1]. The experimentally determined stagnation point is a statistical average of 500 images for a good estimation. A good agreement between the panel method, COMSOL results, and the experiments for the spatial location of stagnation point as a function of increasing source strength is shown in Fig. 3.6A. This indicates that the panel method is a reliable option to predict the Hele-Shaw flow in the device. The panel method is computationally inexpensive compared to COMSOL simulations because the former is strictly based on potential flow theory, whereas the latter solves the Navier-Stokes equations.

3.3 MODELING THE RESPONSE TIME OF THE PUMP

The particle manipulation approach relies on the input of time-depending flow rates to manipulate the streamline pattern in real-time and control the particle trajectories. This approach requires that the flow rates imposed in the device closely follow the pre-defined value imposed. It can be achieved by characterizing the time response of the pump. The pre-defined flow rates are transmitted to the pressure pump as discrete input points. However, the volumetric flow rate imposed by the pump does not give the desired flow rate values instantaneously because the pump responds with a time delay. In order to take into account this systematic error from the pump, the pump response time is calculated. An experiment is performed in the flow cell where the flow rate is 0 μl/min in all the inlets except inlet 2. In the inlet 2, a constant flow rate of 10 μl/min is maintained with a constant uniform flow of $\boldsymbol{u}=$ (80,0) mm/s. Once the flow rate reaches a stable value of 10 μl/min, the flow rate at inlet 2 is increased to 11 μl/min, and the pump response time is deduced for the variation of 1μl/min in the flow rate. The time that the pump requires to reach

the pre-defined output value is deduced from the data logging file of the pump software that has a 20 ms sampling frequency. Similarly, the pump response time data is logged for multiple flow rate variations cases as shown in Fig. 3.7a.

The flow rate from the pump are recorded and fitted with the step response of the first-order system [93] that can be written as follows:

$$b(t) = -e^{-(\frac{t}{T})}a(t) \tag{3.10}$$

Here, $b(t)$ is the response to a unit step, t represents the time, T is the response time and $a(t)$ is a unit step signal. From the pump response time [Fig. 3.7a], the pump response behaves as a first-order system because it fits a simple exponential curve. The value of pump response time T is obtained from the equation 3.10. The average value of T from all the test cases is obtained to be 2.5 s.

Based on the first-order system, the input flow rate that will be transmitted to the pump $r_1(t)$ can be calculated from the pre-defined flow rate $c(t)$ and the response time T. The Laplace transform of the first-order system equation is given as:

$$R_1(S) = (sT + 1) \cdot C(s) \tag{3.11}$$

Here, $C(s)$ is the Laplace transform of the output flow rate c(t), $R_1(s)$ is the Laplace transform of the modified input flow rate r1(t) and T is the response time. In the above equation, using the time constant, T = 2.5 seconds, the modified input flow rate $R1(s)$ is calculated in the frequency domain. The flow rate that will be transmitted to the pump, $r1(t)$, is transformed from frequency domain to time domain using inverse Laplace transform of $R1(s)$.

Using the transfer function from equation 3.11, the flow rates required for the experimental setup are calculated. The desired pre-defined output for uniform flow inlet, inlet 1,2 and 3 is shown in Fig.3.8A. When the pre-defined flow rates are transmitted to the pump without considering the pump response time, a significant deviation between the measured flow rates of the pump (dotted line) and the pre-defined flow rates (solid lines) can be observed, see Fig.3.8B. The step-like response in the experimental data is because the input value in the pump is updated at discrete time steps, and the pump has a first-order response. The value of the flow rate given to the pump is updated at a discrete-time step of 2.5 seconds corresponding to the minimum time the pump takes to reach the next desired value [Fig.3.7]. When the pump input is modified to take into account the response time of the pump, the flow rates imposed by the pump (dotted line) closely agree with the pre-defined output (solid line) as shown in Fig.3.8C. In this case, the input value of the pump is updated at discrete time steps of 2.5 seconds. Thus, in all the experiments hereafter, the pre-computed flow rates determined from the *a priori* particle manipulation algorithm are modified to take into account the response time of the pump.
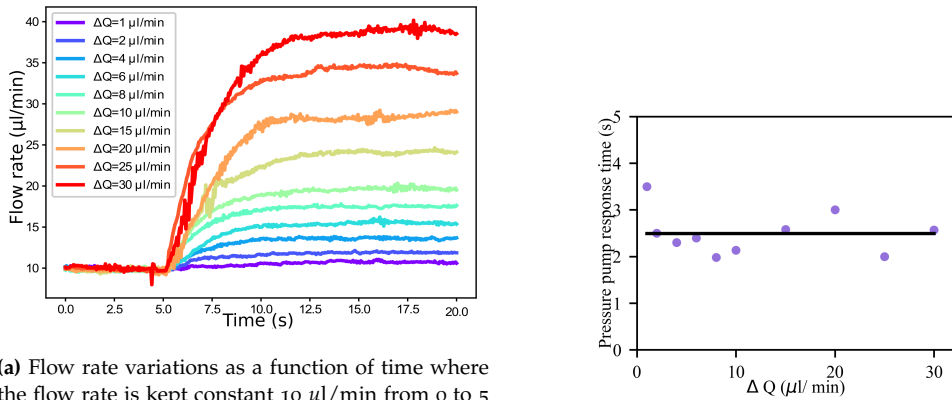
(a) Flow rate variations as a function of time where the flow rate is kept constant 10 μl/min from 0 to 5 secs for all the test cases. At t = 5 secs, a new input value is transmitted to the pump. The experiment is repeated for multiple flow rate variations.

(b) Pump response time for different flow rate variations, ΔQ

Figure 3.7: Characterization of the response time of the flow rate sensor of the pressure pump
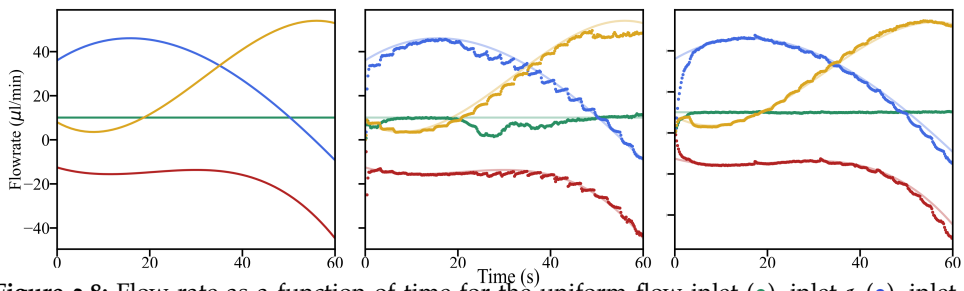
Figure 3.8: Flow rate as a function of time for the uniform flow inlet (●), inlet 1 (●), inlet 2 (●) and inlet 3 (●).(A) pre-defined output (B) pre-defined output (solid lines); experimentally measured flow rates from the pump without modeling the pump response time to the input flow rate (dotted lines). (C) pre-defined output (solid lines); experimentally measured flow rates from the pump for the modified input where the input is modeled with the pump response time (dotted lines).

3.4 A PRIORI PARTICLE MANIPULATION ALGORITHM

In the following, the workflow of the *a priori* particle manipulation algorithm is described that computes the time dependant flow rates Q which allows the algorithm to find the optimum particle trajectory between initial particle position $X_{Pi}(t_0)$ and final particle position $X_{Pi}(t_f)$. Here, i is the index of the particle to be manipulated, t_0 and t_f represent the time where the particle is at the initial position and the final position, respectively. In addition, the *a priori* particle manipulation algorithm is designed to find the flow rate (Q) with the lowest possible magnitude and also the lowest possible flow rate variations $\left(\frac{dQ}{dt}\right)$. It is desirable to have simple inputs to the pump for better control over the flow rates

during the experiments. In this approach, we assume that the particles are sufficiently large ($d_p \approx h$) such that their motion is not affected by Brownian motion. Hence the particle is advected at the local fluid velocity $\mathbf{u}(X_{Pi})$, such that $X_{Pi}(t) = \eta \cdot \mathbf{u}(X_{Pi})$, where $X_{Pi}(t)$ is particle position in x- and y-direction at time t, i is the index of the particle to be manipulated, η is a proportionality constant that depends on the particle shape and ratio of particle size and channel height [60]. Throughout this thesis, the particles used for experiments are spherical and have a particle diameter-to-channel height ratio of 0.6.

Here, all the parameters are non-dimensional as discussed previously in section 3.2.2. To decrease the complexity of the optimization problem, we optimize the flow rates as a function of time $Q_1^*(t)$, $Q_2^*(t)$, $Q_3^*(t)$, instead of optimizing for a discrete set of values of the flow rates. The flow rates as a function of time are projected on a finite base of the orthogonal polynomials, and the coefficients of those orthogonal expansions are used as design variables. The total time duration for optimization, t^* is defined over a range [a,b] that obeys the orthogonality relation. A time interval $t^* = [-1, 1]$ is chosen because most of the orthogonal polynomials relevant to this study have their orthogonality relation in the range [-1, 1].

The solution of the above-described optimization problem is found by using a two-step solution. The first optimization step finds a feasible solution, and the second optimization step finds a solution that minimizes the magnitude of the flow rate limits and the time variation of the flow rate. The performance of different bases of orthogonal polynomials is analyzed further in section 3.4.3.

3.4.1   FIRST OPTIMIZATION STEP: UNCONSTRAINED OPTIMIZATION

The input parameters for the first optimization step are the initial particle position $X_{Pi}(t_0^*)$, the pre-defined final particle position $X_{Pi}(t_f^*)$ and the non-dimensional uniform flow $\mathbf{u}^* = (u^*, 0)$. The optimization algorithm utilizes the coefficients of orthogonal expansions to compute the flow rates that gives an optimized particle trajectory between pre-defined initial and final particle position. A quasi-Newton method [94] based unconstrained optimization is used to minimize the objective function J_1, *i.e.* the norm of the distance between the particle position at the final time step $X_{Pi}(t_k^*)$ and the pre-defined final position $X_{Pi}(t_f^*)$:

$$\min_{Q^*} J_1 = ||X_{Pi}(t_k^*) - X_{Pi}(t_f^*)|| \tag{3.12}$$

3.4.2   SECOND OPTIMIZATION STEP: CONSTRAINED OPTIMIZATION

The Q^* and the particle trajectory acquired from the first optimization step are used as the input parameter for the second optimization step. The second optimization step uses a gradient descent based constrained optimization, where the objective function J_2 to be minimized consists of flow rate variations $\frac{dQ^*}{dt^*}$ and
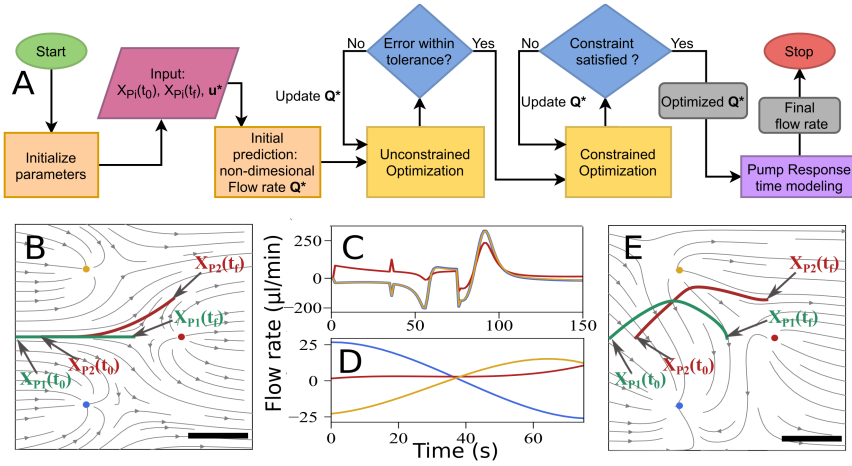
Figure 3.9: (A) Overview of the *a priori* particle manipulation algorithm. (B) and (E) illustrate two trajectories showing particle separation where the two particles are made to travel from the initial position to their final desired positions. $X_{P1}(t_0)$ and $X_{P1}(t_f)$ denote pre-defined initial and final particle location for particle 1 respectively. Similarly, $X_{P2}(t_0)$ and $X_{P2}(t_f)$ are for particle 2. To achieve the non-optimized trajectory (B) high flow rates with flow rate fluctuations are required (C) compared to the flow rate required (D) for the optimized particle trajectory (E). The scale bar represents 4 mm.

the absolute value of the flow rates Q^*. The objective function J_2 is minimized subject to the constraint that the distance between the particle position at the final time step $X_{Pi}(t_k^*)$ and the pre-defined final position $X_{Pi}(t_f^*)$ should be minimal:

$$\min_{Q^*, \frac{dQ^*}{dt^*}} J_2 = \alpha \cdot \int_{t^*=-1}^{t^*=1} \frac{\partial |Q^*|}{\partial t^*} dt^* + \beta \cdot \int_{t^*=-1}^{t^*=1} |Q^*| dt^* \qquad (3.13)$$

such that the following constraint is imposed:

$$||X_{Pi}(t_k^*) - X_{Pi}(t_f^*)|| = 0 \qquad (3.14)$$

Here, α and β are arbitrary weights that can be tuned based on the flow rates, Q^*, with either small-time variations (when α is comparatively higher) or small absolute values (when β is higher). Constant values of 1 and 10^{-3} are used for α and β respectively. These values are used because higher priority was given to minimize the flow rate variations. The integrals in equation 3.13 are numerically estimated using the trapezoidal rule. The dimensions are added to the non-dimensional flow rates Q^* using the characteristic length scale l_c and the characteristic uniform flow u_c, see section 3.2.2. The dimensional flow rate is denoted as $Q = [Q_1, Q_2, Q_3]$ for inlets 1, 2 and 3 respectively.

Numerically, the *a priori* particle manipulation algorithm is first assessed on an arbitrary test case. In this test case, two particles that are initially traveling on the
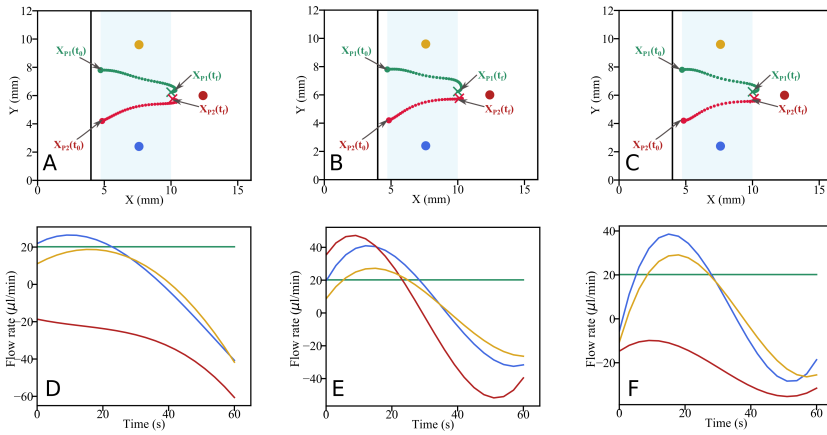
Figure 3.10: Optimized particle trajectories showing particles coming closer to each other for (━━: particle 1, ━━: particle 2) for (A) Legendre Polynomials (B) Chebyshev Polynomials (C) Hermite Polynomials. $X_{P1}(t_0)$ and $X_{P1}(t_f)$ denotes pre-defined initial and final particle location for particle 1 respectively. Similarly, $X_{P2}(t_0)$ and $X_{P2}(t_f)$ are for particle 2. The black square box marks the measurement domain. The blue shaded area marks the manipulation region. The time-varying flow rates as a function of time are plotted for (D) Legendre Polynomials (E) Chebyshev Polynomials and (F) Hermite Polynomials.

same streamline are separated based on the imposed final position for which the two particles are on separate streamlines. Fig. 3.9B shows the particle trajectory of a particle pair when forced to travel on a pre-defined particle trajectory without first and second optimization step. Fig. 3.9E shows the particle trajectories calculated using the *a priori* particle manipulation algorithm which is a two-step optimization routine. Fig. 3.9C-D indicates that if two particles are travelling on a certain pre-defined particle trajectory, the required flow rates can be almost 15 times larger compared to the flow rates calculated from the *a priori* particle manipulation algorithm. Moreover, the *a priori* particle manipulation algorithm eliminates the sharp variations in the flow rate, which are seen in the flow rates of the non-optimized solution. A similar effect of the particle optimization routine was noticed by Schneider *et al.*[55].

3.4.3 EFFECT OF THE CHOICE OF POLYNOMIAL BASE ON THE PARTICLE MANIPULATION ALGORITHM

The *a priori* particle manipulation algorithm discussed in the section 3.4 uses a linear combination of the coefficients of the orthogonal polynomials. A parametric study is carried out to investigate which orthogonal polynomial is relevant for this study. Polynomials such as Legendre polynomials, Chebyshev polynomials of the first kind, and Hermite polynomials are investigated. Legendre and Chebyshev
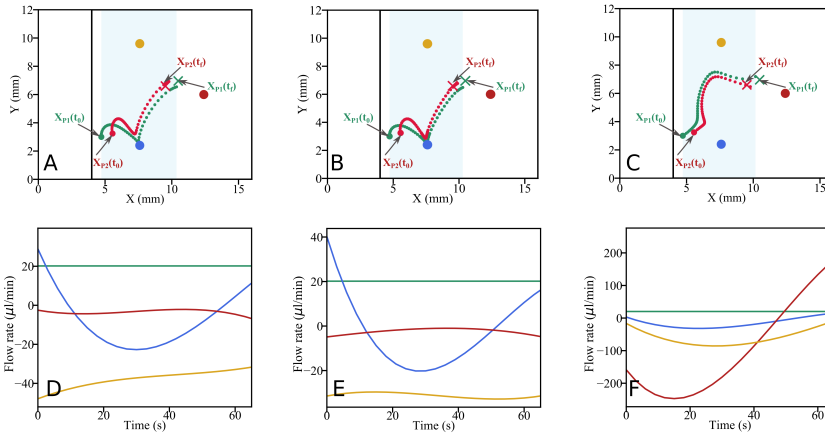
Figure 3.11: Optimized particle trajectories showing particles switching their position as they move downstream (━━: particle 1, ━━: particle 2) for (A) Legendre Polynomials (B) Chebyshev Polynomials (C) Hermite Polynomials. $X_{P1}(t_0)$ and $X_{P1}(t_f)$ denotes pre-defined initial and final particle location for particle 1 respectively. Similarly, $X_{P2}(t_0)$ and $X_{P2}(t_f)$ are for particle 2. The black square box marks the measurement domain. The blue shaded area marks the manipulation region. The time-varying flow rates as a function of time are plotted for (D) Legendre Polynomials (E) Chebyshev Polynomials and (F) Hermite Polynomials. Note that the flow rate bound for Hermite polynomials is an order of magnitude higher.

polynomials form an orthogonal basis for polynomials in the interval [-1,1] with weight functions $w(t^*)$ 1 and $(1 - t^{*2})^{-1/2}$ respectively. Hermite polynomials are orthogonal in interval [-∞, ∞] with weight $e^{-t^{*2}}$. The argument t^* represents non-dimensional time. The coefficients of the orthogonal polynomials did not show a significant effect on the solution beyond the fourth-order of the orthogonal polynomials. Hence, throughout this work, a fourth-order orthogonal polynomial is used to represent the flow rates as a function of time.

Two particles (marked as red and green in Fig. 3.10) at initial particle positions $X_{P1}(t_0)$ and $X_{P2}(t_0)$ are brought close to each other at final particle positions $X_{P1}(t_f)$ and $X_{P2}(t_f)$. Based on the input, the *a priori* particle manipulation algorithm determines the optimized particle trajectories and the corresponding time-varying flow rates using different polynomial bases to represent the flow rates. It is observed that the optimized particle trajectories are very similar for all three polynomials basis as illustrated in Fig. 3.10A, B, C. However, the differences in their corresponding flow rate are evident. Although the flow rate in all three cases has a similar magnitude, the flow rate variations of Legendre polynomials are the lowest, followed by Chebyshev polynomials as shown in Fig. 3.10D, E, F. Similarly, another test case of particle switching their positions as they move downstream is analyzed, see Fig. 3.11. Legendre and Chebyshev polynomial performance are identical in terms of optimized particle trajectories, and

time-varying flow rate variations are indicated in Fig. 3.11A, B, C, D. The performance of Hermite polynomials significantly differs from the other two polynomials. The flow rate variations are small, but the flow rate magnitude is an order of magnitude higher, see Fig. 3.11E, F.

The choice of orthogonal polynomials is a mathematical choice and not a physics-based choice, because all three sets of polynomials give an optimum solution. The convergence of Hermite polynomial to the optimum solution is slower compared to Legendre and Chebyshev polynomials. The performance of the Legendre and Chebyshev polynomials are very similar in their optimized particle trajectories and flow rate bounds. Nevertheless, Legendre polynomials are selected as a suitable candidate for the *a priori* particle manipulation algorithm, because in practice they showed the lowest flow rate variations.

3.5   RESULTS

The coordinates of the particles are acquired during the experiment from the in-house developed image acquisition LabVIEW program. The initial $X_{pi}(t_0)$ and final $X_{pi}(t_f)$ particle locations are used as input parameters for the particle manipulation algorithm written in MATLAB. The program computes the optimized flow rate for given particle manipulation, which is further transmitted to the LabVIEW program to deliver the required flow rates into the flow cell. The maximum deviation, $\varepsilon(X_P)$, between the optimized particle trajectories and experimentally measured trajectories is calculated as the percentage change of the linear dimension of the measurement domain (12 mm). Hereafter, the results are presented for various test cases using the above-mentioned approach.

3.5.1   SINGLE PARTICLE DEFLECTION

This experiment shows that a particle can travel along the pre-computed optimized particle trajectory with minor deviations during the experiment based on the real-time selection of initial particle position $X_{P1}(t_0)$ and final particle position $X_{P1}(t_f)$. Throughout the experiment, a constant uniform flow of 80 μm/s is imposed, corresponding to the flow rate of 20 μl/min. The particle approaches the measurement domain due to uniform flow in the x-direction as shown in Fig. 3.12A. Based on the pre-defined $X_{P1}(t_0)$ and $X_{P1}(t_f)$, the *a priori* particle manipulation algorithm computes the optimized particle trajectory (solid green line in Fig. 3.12A) and corresponding flow rates are transmitted into the pump. Once the particle reaches the starting point of the manipulation, the pre-computed flow rates start to be imposed based on the prescribed pre-computed flow rates. Thus, leading to a time-dependent change in the streamline pattern of the flow cell. As a result, the particle gets advected along the streamlines and moves toward the pre-defined final location, $X_{P1}(t_f)$. The dashed line indicates the experimental trajectory. A good agreement between the simulated and the experimental
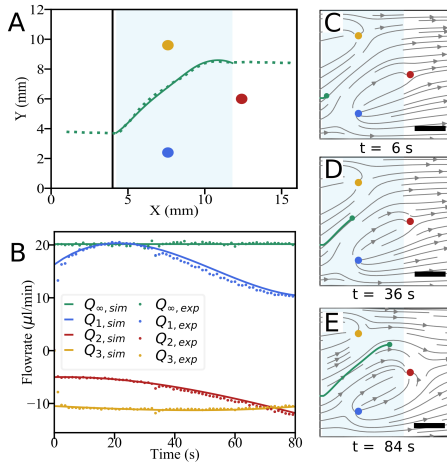
Figure 3.12: (A) Particle trajectory showing particle deflection for (▬) optimized particle trajectory and (▪▪▪) experimentally measured particle trajectory. $X_{P1}(t_0)$ and $X_{P1}(t_f)$ denotes pre-defined initial and final particle location for particle 1 respectively. A black square box marks the measurement domain. The blue shaded area indicates the region where manipulation was applied. (B) Imposed and experimentally measured flow rates. The streamlines are obtained from the experimental flow rate data at different time instants during the manipulation process: (C) t = 6 s (D) t = 36 s and (E) t = 84 s. The scale bar represents 4 mm. **Movie 3.1** shows the experimental video of this test case.

trajectory is observed. It is achieved because there is a good agreement between the simulated and the actual flow rates shown in Fig. 3.12B. The maximum error in particle location is 0.8% of the linear dimension of the measurement domain (12 x 12 mm^2).

Next, the experimental flow patterns are analyzed. This helps to visualize the streamlines during the manipulation event. Here, the streamlines during the manipulation time of, t = 6 s, 36 s, and 84 s are plotted corresponding to Fig. 3.12C, D, and E, respectively. Throughout the manipulation event, the streamline pattern does not change significantly. Initially, the flow field changes considerably, and the streamlines move towards inlet 3 as the inlet 1 has a high source strength [Fig. 3.12C]. The particle advects with the streamlines as the streamline continues to move towards inlet 3 as inlet 2 and 3 continue to act as sinks; meanwhile, the source strength of inlet 1 decreases [Fig. 3.12D]. Finally, the particle descends for a short duration and move towards the final location [Fig. 3.12E]. From the literature [55], it is known that only three inlets are sufficient to manipulate a single particle. However, with five inlets, the imposed flow rate variations are small because additional inlets give more flexibility in controlling the particle.

3.5.2 SINGLE PARTICLE TRAPPING

In the single-particle trapping, a flow rate of 20 μl/min is imposed upstream and yields a uniform flow, $\mathbf{u}$ = (80, 0) μm/s. The particle approaches the measurement domain from the centerline along the width of the device. The particle is trapped in the control area (red-shaded region) as shown in Fig. 3.13A. Based on the initial particle position $X_{P1}(t_0)$ and trapping location, the particle manipulation
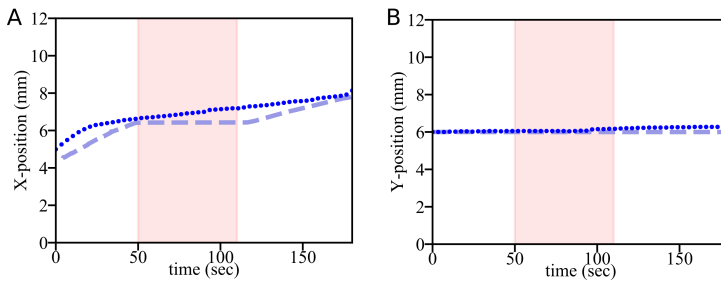
Figure 3.13: (A) Particle trajectories showing particle trapping for (━━) optimized particle trajectory and (•) experimentally measured particle position data. $X_{P1}(t_0)$ and $X_{P1}(t_f)$ denotes pre-defined initial and final particle location for particle 1 respectively. A black square box marks the measurement domain. The blue shaded area indicates the region where manipulation was applied. Red shaded area indicates trap location. (B) Imposed and experimentally measured flow rates. The streamlines obtained from the experimental flow rate data at different time instants during the manipulation process: (C) t = 20 s (D) t = 60 s and (E) t = 160 s. The scale bar represents 4 mm. **Movie 3.2** shows the experimental video of this test case.
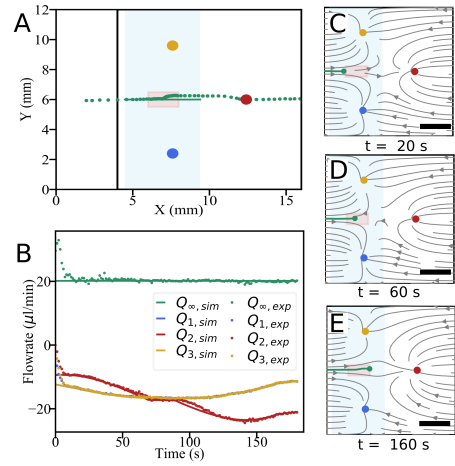
Figure 3.14: The dashed lines shows optimized particle trajectory and dotted line shows experimentally measured position for a particle that is trapped and released. The red shaded region shows the pre-defined particle trap duration. (A) Particle displacement in *x*-direction as a function of time. (B) Particle displacement in *y*-direction as a function of time.

algorithm calculates the optimized particle trajectory and the corresponding flow rates that are transmitted into the pump. As the particle enters the manipulation area, the pre-computed flow rates are imposed. The green dots in Fig. 3.13A indicates the experimentally measured particle position, which shows that the particle significantly slows down in the trapping area. The imposed and the experimentally measured flow rates are in close agreement, see Fig. 3.13B. The maximum deviation, $\varepsilon(X_P)$, in particle location is 1%. Next, the flow pattern is deduced from the experimentally measured flow rates during the manipulation at the time, t = 20 s, 60 s, and 160 s corresponding to Fig. 3.13C, D, and E, respectively. The particle starts to slow down as the inlets 1, 2, and 3 act as sinks [Fig. 3.13C]. The particle substantially slowed down but did not get completely trapped in the stagnation point, and the flow rates in inlets 1, 2, and 3 remain at constant sink strength for a manipulation period from 60 s to 90 s. As the
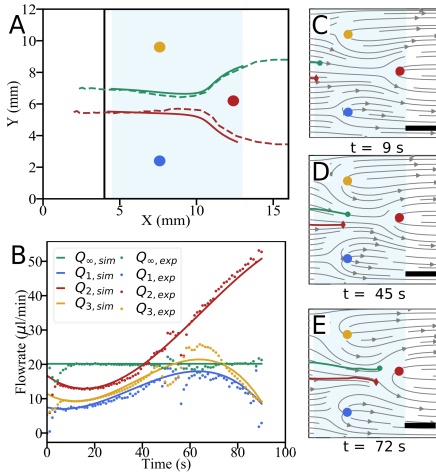
Figure 3.15: Separating two particles: (A) Particle trajectories showing particle separation for optimized particle trajectories (▬: particle 1, ▬: particle 2) and experimentally measured (▪▪▪: particle 1, ▪▪▪: particle 2) data. $X_{P1}(t_0)$ and $X_{P1}(t_f)$ denotes pre-defined initial and final particle location for particle 1 respectively. Similarly, $X_{P2}(t_0)$ and $X_{P2}(t_f)$ are for particle 2. A black square box marks the measurement domain. The blue shaded area indicates the region where manipulation was applied. (B) Imposed and experimentally measured flow rates. The streamlines are obtained from the experimental flow rate data at different time instants during the manipulation process: (C) t = 9 s (D) t = 45 s and (E) t = 72 s. The scale bar represents 4 mm. **Movie 3.3** shows the experimental video of this test case.

stagnation point is inherently unstable, in this case, the particles move slightly away from the optimized particle trajectory [Fig. 3.13D]. Eventually, the particle resumes advecting downstream after the trapping time ends [Fig. 3.13E].

In the trapping duration of 60 seconds, in Fig. 3.14A, the particle translates in x-direction by 410μm i.e. equivalent to approximately twice the diameter of the particle. In y-direction, the experimentally measured particle position had no significant deviation compared to the optimized particle trajectory, see Fig. 3.14B.

3.5.3 SEPARATING TWO PARTICLES

In a subsequent test, the functionality of the micro-device is demonstrated for particle separation. This test case simulates a Y-channel where each particle flows in either of the two branches of the channel. Throughout the experiment, a constant uniform flow, $\mathbf{u}$ = (80,0) μm/s is imposed. Optimized particle trajectories are computed based on the pre-defined final position, $X_{P1}(t_f)$ and $X_{P2}(t_f)$ for particle 1 and particle 2 respectively and their potential start point, $X_{P1}(t_0)$ and $X_{P2}(t_0)$, where the particle pair would enter the square domain. The optimized particle trajectories are indicated as solid green and red lines in Fig. 3.15A. When the particles reach the starting points of the manipulation, the pump begins to impose the pre-computed flow rates based on the optimized particle trajectories. The particles are manipulated due to the change in the flow rates in the flow cell in the manipulation area (blue shaded region). The experimentally measured trajectories are depicted by dashed lines in Fig. 3.15A. The maximum deviation,

Movie 3.3

Figure 3.16: Joining two particles: (A) Particle trajectories showing particles approaching each other for optimized particle trajectories (━━: particle 1, ━━: particle 2) and experimentally measured (▪▪▪: particle 1, ▪▪▪: particle 2) data. $X_{P1}(t_0)$ and $X_{P1}(t_f)$ denotes pre-defined initial and final particle location for particle 1 respectively. Similarly, $X_{P2}(t_0)$ and $X_{P2}(t_f)$ are for particle 2. A black square box marks the measurement domain. The blue shaded area indicates the manipulation region. (B) Imposed and experimentally measured flow rates. The streamlines are obtained from the experimental flow rate data at different time instants during the manipulation process: (C) t = 10.5 s (D) t = 20 s and (E) t = 45 s. The scale bar represents 4 mm. **Movie 3.4** shows the experimental video of this test case.
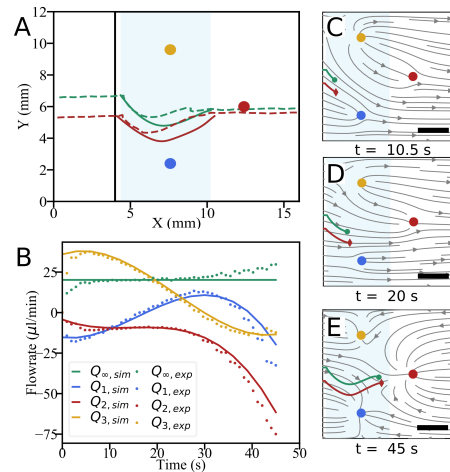
$\varepsilon(X_P)$, in particle location is 3.3%. A good agreement between the imposed flow rates and the experimentally measured flow rates is shown in Fig.3.15B.

Further, streamline patterns are analyzed using the measured flow rates determined from the experiments during the manipulation at the time, t= 9 s, 45 s, and 72 s corresponding to Fig. 3.15C, D, and E, respectively. The particle pair moves downstream without any significant change in their trajectories [Fig. 3.15C]. The particles accelerate as the streamlines get squeezed in between the widths of the two Rankine half-bodies originating from inlets 1 and 3 [Fig. 3.15D]. As the particles travel towards inlet 2, the source strength of inlet 2 increases substantially to separate the two particles and move them closer to the pre-defined positions [Fig. 3.15E].

3.5.4   JOINING TWO PARTICLES

The joining of two particles was done to demonstrate the functionality of our flow cell for studies related to coalescence, particle assembly, and adhesion. A constant uniform flow, $\mathbf{u}$ = (80,0) μm/s is imposed throughout the experiment. The solid green and red lines show the computed optimized particle trajectories based on the pre-defined initial location ($X_{P1}(t_0)$ and $X_{P2}(t_0)$) and final locations ($X_{P1}(t_f)$ and $X_{P2}(t_f)$) for particle 1 and 2, respectively, as shown in Fig. 3.16A. The dashed green and red lines show the experimentally measured particle trajectories for particles 1 and 2, respectively. Due to the constant uniform flow, the particles translate in the x-direction as they approach the manipulation area. In the manipulation area, the particle-pair approach each other based on the optimized

trajectories, followed by the particle pair traveling downstream due to the uniform flow as illustrated in Fig. 3.16A. The maximum error, $\varepsilon(X_P)$, in particle location is 16.6%. The deviation between the imposed flow rates and the experimentally measured flow rates is shown in Fig.3.16B. The actual flow rates deviate from the calculated flow rates between the manipulation time of 30 s and 45 s. This deviation can be due to the inability of the pump to effectively deliver the flow rates under high flow rate variations, which is simultaneously varying for inlets 1, 2, and 3, or the particle was not exactly at the center-line across the channel height or particle coagulation in the system.

Furthermore, the streamline patterns are investigated using the experimentally measured flow rates during the manipulation at the time, t= 10.5 s, 20 s, and 45 s corresponding to Fig. 3.16C, D, and E, respectively. First, the particles deflect towards inlet 1 under the influence of the sink and source from inlets 1 and 3, respectively [Fig. 3.16C]. Then, the particles begin to move towards inlet 3 as inlet 1 acts as a source instead of a sink at the beginning of the manipulation period [Fig. 3.16D]. Finally, as the particles travel towards inlet 2, the slope of the streamline on which the second particle is advecting is higher. Thus, it comes close to the first particle as they move towards the pre-defined final positions [Fig. 3.16E].

3.5.5 VIRTUAL MIXING CHANNEL

Further, the mixing of particles in a rectangular channel is demonstrated. Mixing is mostly required for sample dilution, chemical reactions, or DNA extraction [95]. Based on the application, achieving sufficient mixing is difficult in a microfluidic device due to the laminar flows. Throughout the experiment, there is a constant uniform flow, $\mathbf{u}$ = (40,0) μm/s which corresponds to a flow rate of 10 μl/min. As a particle pair approaches the measurement domain, the particles are manipulated to switch their positions downstream of the flow cell using *a priori* particle manipulation algorithm. The optimized particle trajectories (solid green and red lines) are indicated in Fig. 3.17A. The dashed green and red line show the experimentally measured particle trajectories for particles 1 and 2, respectively. The maximum error, $\varepsilon(X_P)$, in particle location is 8%. A good agreement between the imposed and the experimentally measured flow rates is shown in Fig.3.17B.

The streamline patterns derived from the experiment flow rates for the manipulation at the time, t= 50 s, 100 s, and 150 s are shown Fig. 3.17C, D, and E, respectively. In the beginning, particle 1 is upstream and closer to inlet 1 with respect to particle 2. They come close to each other near inlet 1, which acts as a sink [Fig. 3.17C]. As both the particles get deflected towards inlet 3; particle 1 begins to overtake particle 2. This is because particle 1 follows a streamline that is more influenced by the sink strength of inlet 3 compared to the streamline that is followed by particle 2 [Fig. 3.17D]. Towards the end of the manipulation period, particle 1 is downstream and closer to inlet 3 with respect to particle 2 [Fig. 3.17E].

Movie 3.5

Figure 3.17: Virtual mixing channel: (A) Particle trajectories showing particle mixing for optimized particle trajectories (━━: particle 1, ━━: particle 2) and experimentally measured (▪▪▪: particle 1, ▪▪▪: particle 2) data. $X_{P1}(t_0)$ and $X_{P1}(t_f)$ denotes pre-defined initial and final particle location for particle 1 respectively. Similarly, $X_{P2}(t_0)$ and $X_{P2}(t_f)$ are for particle 2. A black square box marks the measurement domain. The blue shaded area indicates the region where manipulation was applied. (B) Imposed and experimentally measured flow rates. The streamlines are obtained from the experimental flow rate data at different time instants during the manipulation process: (C) t = 50 s (D) t = 100 s and (E) t = 150 s. The scale bar represents 4 mm. **Movie 3.5** shows the experimental video of this test case.
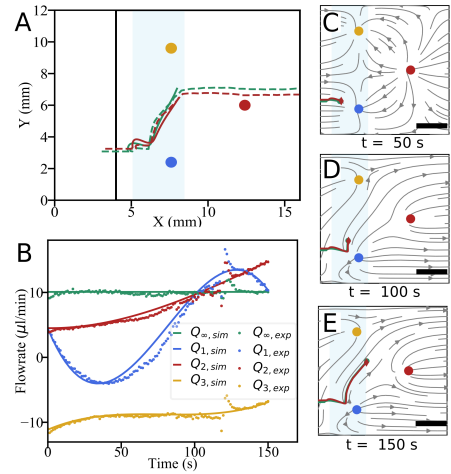
3.6 DISCUSSION AND CONCLUSION

This chapter describes a method to create "virtual channels" in a Hele-Shaw cell using hydrodynamic forcing only. First, the flow model is validated by comparing the position of a stagnation point induced by a single source in a uniform flow. The flow model for the bulk fluid velocity and the particle velocity is based on assuming that the depth-averaged flow in the Hele-Shaw cell behaves as a potential flow. This allows us to take a linear superposition of 2D point sources and a uniform flow to represent and compute the flow patterns. Fig.3.6 shows that the spatial position of the stagnation point induced by varying the source strength predicted by the source-based panel method and COMSOL simulations are in agreement with the experimental data. The advantage of using the panel method is that it is based on potential flow theory, and the computational cost is significantly lower compared to COMSOL simulations, which makes it suitable for real-time applications.

Secondly, a novel *a priori* particle manipulation algorithm is introduced to determine optimal particle trajectories *a priori*, based on the pre-defined initial and final particle location. The optimized particle trajectory is determined while minimizing the magnitude of the flow rates and the flow rate variations. The *a priori* particle manipulation algorithm can be scaled to different Hele-Shaw cells based on their physical dimensions. It is possible since the entire optimization calculations are performed on non-dimensional terms that are scaled by the length scale of the region of interest, channel height, and the uniform flow velocity. The five inlets in the current flow cell are the minimum number of inlets required to manipulate two particles simultaneously. These five inlets are designed to have an

inlet for uniform flow, three inlets to inject or extract liquid, and an outlet to maintain mass conservation.

Thirdly, experiments are presented to show that the device is capable of elementary microfluidic manipulations such as sorting (see Fig. 3.12), trapping (see Fig. 3.13), separating (see Fig. 3.15), joining (see Fig. 3.16) and interchanging the position of two particles (see Fig. 3.17). All these processes can be done on a single microfluidic device instead of having multiple separate devices.

A key observation was that if the imposed flow rates are stable, the experimental particle trajectories match the *a priori* optimized particle trajectories determined using the potential flow. However, this is not always the case as shown in Fig. 3.15, 3.16, 3.17. This happens because certain aspects are not included in the *a priori* computations, such as particle density and off-center particle position along with the channel height. Hence, to improve the repeatability of the experiments, a feedback loop is necessary. This can be achieved by implementing a PID control and using the pre-computed optimized particle trajectories from the *a priori* particle manipulation algorithm.

CHAPTER 3

4

PARTICLE MANIPULATION WITH A FEEDBACK LOOP

Manipulation of particles within the flow device using the a priori particle manipulation algorithm allows the user to perform various elementary microfluidic processes such as sorting, trapping, separation, selection, and mixing (see section 3.5). These processes can be done on a single flow cell instead of multiple devices and performed using only hydrodynamic forcing. However, a priori particle manipulation algorithm is currently limited by not considering aspects such as surface roughness, particle density, and off-center particle position along the channel height. This would lead to errors in the particle trajectory that will accumulate over time, leading to a complete failure of the experiment. Therefore, it is essential to use feedback control schemes and mitigate aspects of the experiment uncertainty to achieve robust and repeatable experiment results for various experiments. With a feedback loop in an experiment, the error in particle position can be determined with respect to the a priori optimized trajectory, and additional flow rates can be given to correct for the error. In this chapter, the performance of a Proportion-Integral-Derivative-based (PID) controller is investigated. Nonlinear optimization determines the PID control parameters, which are used as initial control parameter for various experiments. Also, the controller architecture during the experimental run is explained in detail. The results show that the experimentally determined particle positions are in close agreement with the optimized trajectory. The maximum error is on the order of one particle diameter at the end of the manipulation.

4.1 INTRODUCTION

The *a priori* manipulation algorithm[1] leverages the linearity of potential flow theory to find the optimized particle trajectory strategy in a fast, straightforward and efficient manner. However, the *a priori* particle manipulation algorithm has a few limitations. Effects such as surface roughness and off-center particle position in the channel are not modeled. In this chapter, the *a priori* particle manipulation algorithm is coupled with closed-loop control, which allows better control of the particle in an experiment. In general, a closed-loop control system is a system of hardware and software that can automatically adjust variations in a process to a set point with pre-defined limits without human interaction. The Proportional-Integral-Derivative (PID) control gives corrective flow rates to the inlets based on the position error of the particles. The particle position error is defined as the difference between the particle location from the *a priori* manipulation algorithm and the experimentally measured particle location. In this chapter, the closed-loop approach is compared to the open-loop approach on the same manipulations discussed in section 3.5 *i.e.* single-particle trajectory deflection, single-particle trapping, separating a particle pair, joining two particles, and interchanging particle pair position.

As an application for the flow cell, the real-time selection of an arbitrary pollen grain (diameter = 70 μm) and its trapping within a control area is demonstrated. The experimental setup and modification in setup for the pollen grain experiment are discussed in section 4.2. The architecture of the PID control scheme during an experiment and the tuning of the controller are described in section 4.3. In section 4.4, results are shown for various test cases where particle trajectories are corrected during an experiment. Concluding remarks on the control scheme and potential improvements in the flow cells and the control approach are discussed in section 4.5.

4.2 EXPERIMENTAL SETUP

For the pollen grain experiment, the experimental setup used is similar to the experimental setup discussed previously in Section 3.2.1. An image of the actual experimental test setup is shown in Fig. 4.1A. A schematic representing all the essential components of the setup is depicted in Fig. 4.1B. The setup consists of a pressure pump with five pressure ports, namely, a uniform flow inlet, an outlet, and three inlets for carrying out the manipulation activities. The working fluid is water in all the reservoirs except reservoir 4*, which contains a water-pollen mixture at a low concentration. The reservoirs are connected to a flow sensor which measures the volumetric flow rates Q_i, where *i* represents the index of the reservoir. Reservoir 4 is connected to reservoir 4* via the flow rate sensor to avoid contamination of the flow sensor with pollen grains. An additional sCMOS camera

---

[1] The *a priroi* particle manipulation algorithm is discussed in Section 3.4
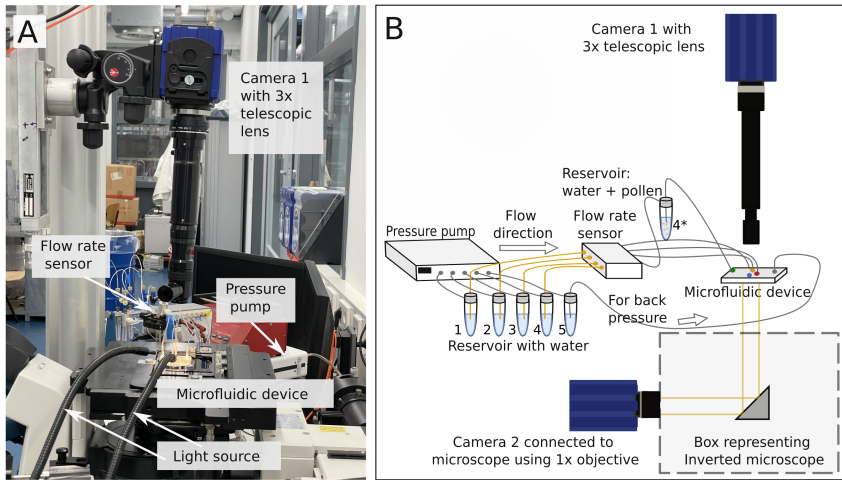
Figure 4.1: (A) Experimental test setup with all the required components except the second camera attached to the microscope (not visible in this picture). (B) The experiment setup schematic shows the microfluidic device with reservoirs connected to the flow rate sensor. The circles on the inlets of the microfluidic device represents uniform flow inlet (•), inlet 1 (•), inlet 2 (•) and inlet 3 (•). A pressure pump drives the fluid through the reservoir using pressurized air. Reservoirs 1, 2, and 3 are connected via the flow rate sensor to inlet 1, 2, and 3 of the microfluidic device, respectively. Reservoir 4 is connected to reservoir 4*, a water-pollen mixture at low concentration. Reservoir 4* and 5 are connected to the uniform flow inlet and outlet, respectively. Camera 1 is mounted on the top of the device with the 3x telescopic lens, and the Camera 2 is mounted on the side of the inverted microscope with the 1x objective to view the entire field of view, 12 × 12 (mm).

(Imager) is required for high magnification visualization of the pollen grain. Camera 1 with a 3x telescopic lens is mounted on the top of the device to capture a high magnification image of the pollen at an acquisition frequency of 15 Hz. Camera 2 was mounted to the Nikon Eclipse Ti inverted microscope, with a 1x objective to view the entire field of view, 12 × 12 (mm), and facilitate the PID control algorithm. The acquisition frequency of camera 2 was 5 Hz, leading to an average in-plane displacement of 4-6 pixels between two consecutive recordings. Cameras 1 and 2 have an exposure time of 50 ms and 100 ms, respectively, to allow enough light to enter the image sensors and accurately identify the pollen grain on the images.

4.3 FEEDBACK LOOP: PID CONTROL

A feedback system is implemented to correct for particle drift and minimize the deviation of the particles during an experiment. In the feedback loop, the flow rate output is *corrected* based on the real-time measurements of the deviation of particles
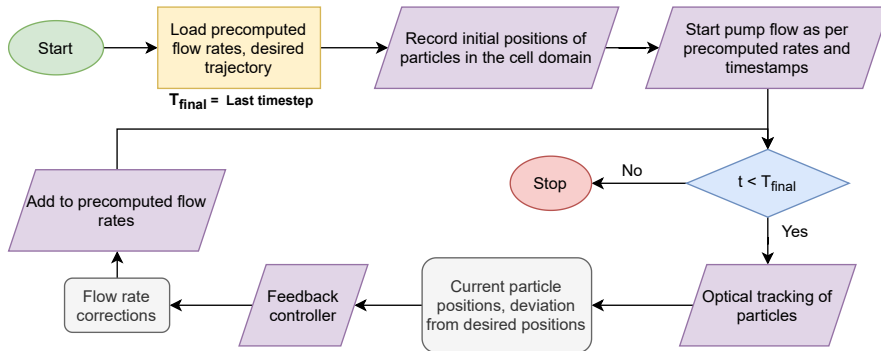
Figure 4.2: High-level flowchart illustrating the steps involved in the experiment with a feedback controller included.

from their optimized trajectories - that is, the control loop is closed using a feedback controller. Furthermore, considering the nature of the uncertainties (i.e., difficulty in modelling them mathematically) and the slow response time of the pump, a PID controller is implemented. The PID controller makes additive corrections to the pre-computed flow rates depending on the deviation of the particles from their optimized trajectories. Fig. 4.2 illustrates the experimental steps broadly with the feedback controller included.

4.3.1 CONTROLLER MODELLING AND ARCHITECTURE

A feedback controller is used when a measured output (setpoint) of a process needs to be maintained at a particular pre-defined value. Since the process is prone to external disturbances, the controller is a function that calculates the process input(s) that would produce the output at a pre-defined value despite the disturbances. The goal of a feedback controller is to reduce the error between the pre-defined (desired) and experimental (measured) output values; ideally, it should minimize the error.

A PID controller is a type of feedback controller that considers the immediate error, the trend of errors over time, and the rate of change of error to calculate the process input at that time step. Hence, the error values for the subsequent time steps are reduced or maintained within a set of limits. A general block diagram representation of a PID controller is shown in 4.3. The proportional (P) block calculates the input to the process based on the immediate error measured at the process output. The integral (I) block takes into consideration the change (accumulation) in error values over time, and the differential (D) block considers the immediate rate of change of error values. Finally, the sum of the output values from the three blocks is taken as the input to be provided to the process.

The primary advantage of a PID controller is that it relies only on the process response (the measured output values) to calculate input values without having an underlying model of the process. Hence, in this case, a PID control can be
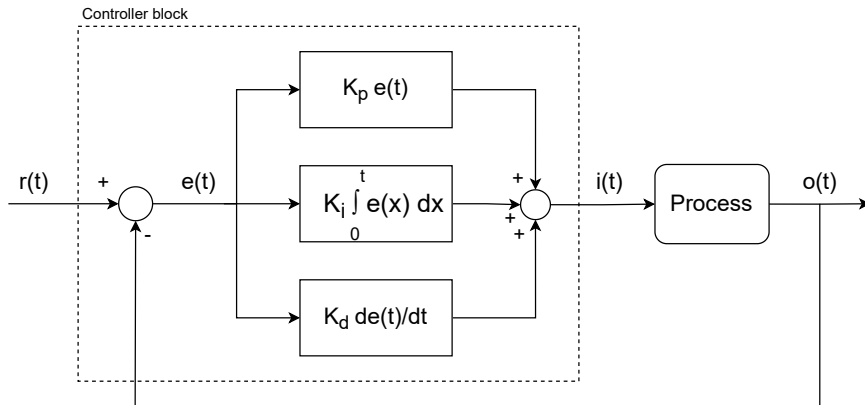
Figure 4.3: A block diagram representing a conventional PID controller. At a given time step t, the output of the process block $o(t)$ should be close to the reference signal, $r(t)$. The input to the process $i(t)$ is calculated so as to reduce the error $e(t)$ (i.e. the difference between the reference and process output values) for the subsequent time steps. K_p, K_i, K_d represent the proportional, integral, and derivative gain values respectively. [96]

implemented as long as the deviation of particles from their pre-defined trajectories can be observed, the details of shape and size of the particles, the pump used and the working fluid medium need not be known.

In this setup, the optimized trajectories of particles and imposed flow rates for the pumps at different time steps are computed beforehand using *a priori* particle manipulation algorithm. The ideal outcome is that the particles follow these pre-defined trajectories exactly during the experiments. However, due to various experimental factors (such as particles not being centered along the channel height of the device, variations in particle density, etc.) the particles deviate from these trajectories - that is, an error is observed for each time step. Hence, a feedback controller becomes necessary to make corrections to the imposed flow rate values in order to reduce the error values, thereby keeping the particles close to their pre-defined optimized trajectories.

Hence, the feedback controller should make corrections to each inlet such that the positional error for the next time step is reduced. Thus, the controller takes a positional error as its input and calculates corrections to the imposed flow rate values as its output. Though there is a direct relation between particle position $\mathbf{X}_P(t)$ and the imposed flow rate values, there may be deviations in particles from their analytically calculated positions due to the non-ideality of experiments. This motivates the usage of a PID controller since the response of the process can be measured (the positional error), and the corresponding inputs can be accordingly calculated (corrections to imposed flow rate values).

In general, a PID controller is used to periodically calculate the inputs for a process based on the error measured at the output. Hence, the output of the controller block is the input for the process. However, in this case, the PID

controller is used as a function to make periodic corrections to the pre-computed process inputs (imposed flow rate values) to reduce the positional error of the particles instead of calculating the actual input values.

The key assumption here is that the PID controller is only used to reduce the positional error at a time step by *correcting* the (pre-computed) imposed flow rate values. Therefore, this approach is not suitable to compute the flow rate values directly.

A live camera feed is used to obtain the current view of the region of interest in the flow cell domain within which the feedback action is applied. Before imposing the pre-computed flow rate values, the initial positions of the particles $\mathbf{X}_{Pi}(t_0)$ are given as feature points for tracking. Here, the Lukas-Kanade algorithm is used [97] to track the motion of the particles during the experiments. Time stamp values are recorded with the obtained position values to get the trajectories of the particles, and these trajectories are provided as inputs to the PID controller.

Based on the system constraints, such as the spatial arrangements of the inlets and the possible differences in mobility along the X and Y axes, the PID controller is structured as a combination of multiple PID controllers. For each particle to be controlled, two PID controllers are used (for positional errors along the X and Y axes). The overall flow rate correction is calculated as the sum of corrections from each PID controller (henceforth referred to as sub-controllers). Since this system involves controlling two particles, there is a total of 4 sub-controllers.

It is assumed that the magnitude of the correction to be made to a given inlet at a time step is proportional to the magnitude of the imposed flow rate value at that time step. The direction of the correction (i.e. whether to add or subtract the controller output for a given inlet) depends on the position of the particle and the direction in which it has deviated from its desired position (the details of which are covered in Section 4.3.2). Each sub-controller has a block for calculating the magnitude of corrections and a block for determining the direction of the corrections; such an arrangement is necessary because three inlets influence the trajectory of each particle and the effect of changing the flow rates depends on the immediate position of the particle. This architecture is illustrated in Fig. 4.4.

For a given particle, the PID sub-controller for a given direction is modelled mathematically as follows:

$$\kappa = \begin{cases} \left| K_p \cdot l_t + K_i \cdot \sum_{k=1}^{t} l_k + K_d \cdot (l_t - l_{t-1}) \right|, & \text{if } |l_t| > d_p \\ 0, & \text{otherwise} \end{cases} \tag{4.1}$$

In this equation, K_p, K_i, K_d are the proportional, integral, and derivative gain values respectively. Since the controller output (κ) is dimensionless, the units of the individual control parameters are as per the value they are multiplied with (i.e. Kp: m^{-1}, Ki: $m^{-1}s^{-1}$, Kd: $m^{-1}s$). The PID controller is essentially a transfer function so the control parameters are scaled according to the chosen inputs values [98]. l_t is the positional error at time step t, i.e. $l_t = \mathbf{X}_{opt}(t) - \mathbf{X}_{exp}(t)$, where $\mathbf{X}_{opt}(t)$ and $\mathbf{X}_{exp}(t)$ are the desired (optimized) and actual (experimental) positions of the
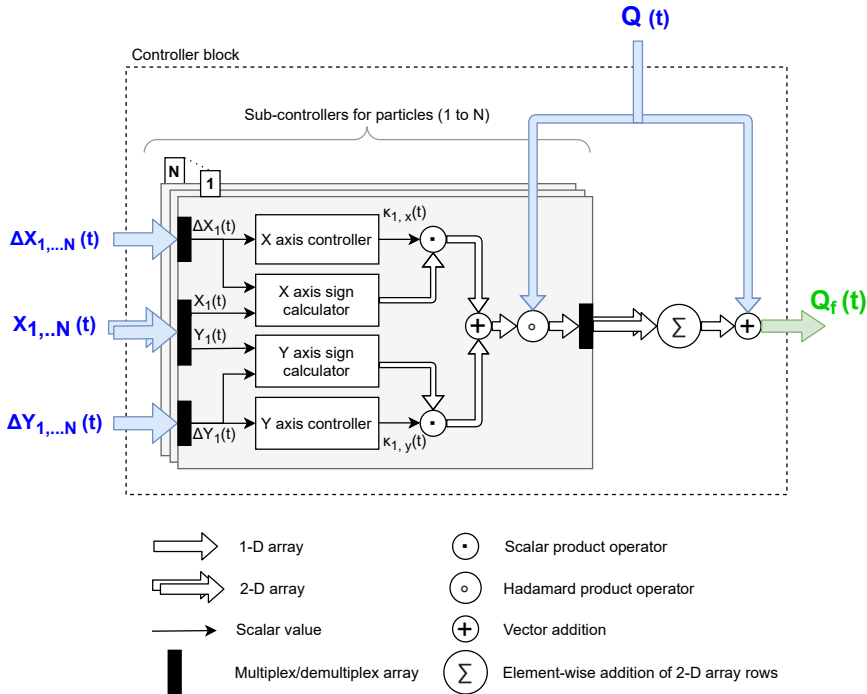
Figure 4.4: Controller architecture illustrating flow corrections at time step t for N particles. The positional errors and position coordinates of each particle are provided as inputs to the overall controller block. $\Delta X_{Pi}(t)$ and $\Delta Y_{Pi}(t)$ are positional error values for particle i at t in the X and Y directions respectively, $\mathbf{X}_{Pi}(t)$ is the current position (a set $(X_{Pi}(t), Y_{Pi}(t))$) of particle i at t, $Q(t)$ is the array of imposed flow rate values at t, and $Q_f(t)$ is the array of corrected flow rates the pump needs to provide. Each particle has an X- and a Y-axis controller for computing the correction factor values ($\kappa_{i,x}(t), \kappa_{i,y}(t)$ respectively for particle i at t) and their corresponding sign calculator blocks. A legend indicating the various symbols is provided below the diagram.

particle respectively along a given direction at time step t. The terms multiplied with $K_p, K_i,$ and K_d represent the instantaneous error, the trend of errors accumulating over time steps, and rate of change of errors respectively. $\sum_{k=1}^{t} l_k$ denotes the accumulation of positon error from the start of the PID controller (k= 1) to the positon error at the current time step (k = t).

κ is the "correction factor" - an abstract quantity by which the imposed flow rate input are scaled at time step t. The flow rate inputs values are multiplied with this factor and yields the magnitude of flow rate corrections to be made at that time step. It is assumed that the diameter of a particle (d_p) is the threshold for applying corrective actions - and thus κ can be negligible for a time step if the positional error in a given direction is too low.

This architecture of the controller is different from the conventional architecture, and therefore an optimization routine is implemented to calculate the controller gain values. It is explained in detail in Section 4.3.4.

Using equation 4.1, the correction factors for a single particle for the two coordinate axes can be expanded as:

$$
\kappa_x = \begin{cases} \left\| [K_{p_x} \ K_{i_x} \ K_{d_x}] \cdot \begin{bmatrix} \Delta X_t \\ \sum_{k=1}^{t} \Delta X_k \\ \Delta X_t - \Delta X_{t-1} \end{bmatrix} \right\|, & \text{if } |\Delta X_t| > d_p \\ \\ 0, & \text{otherwise} \end{cases}
\tag{4.2}
$$

and

$$
\kappa_y = \begin{cases} \left\| [K_{p_y} \ K_{i_y} \ K_{d_y}] \cdot \begin{bmatrix} \Delta Y_t \\ \sum_{k=1}^{t} \Delta Y_k \\ \Delta Y_t - \Delta Y_{t-1} \end{bmatrix} \right\|, & \text{if } |\Delta Y_t| > d_p \\ \\ 0, & \text{otherwise} \end{cases}
\tag{4.3}
$$

κ_x and κ_y are the correction factors in the x- and y-directions respectively. $K_{p_x} \ K_{i_x} \ K_{d_x}$ are the proportional, integral, and derivative gain values for the positional error in the x-direction respectively. Similarly $K_{p_y} \ K_{i_y} \ K_{d_y}$ are the controller gains for the positional error in the y-direction. ΔX_t and ΔY_t denote particle position deviation from the pre-computed path in the x- and y-directions respectively at time step k, i.e. $\Delta X_t = X_{opt}(t) - X_{exp}(t)$, where $X_{opt}(t)$ and $X_{exp}(t)$ are the desired (optimized) and actual (experimental) positions of the particle respectively along the x-direction. Correspondingly, $\Delta Y_t = Y_{opt}(t) - Y_{exp}(t)$, where $Y_{opt}(t)$ and $Y_{exp}(t)$ are the optimized and actual (experimental) positions of the particle respectively along the y-direction.

The particles to be manipulated may not have the same value of error along the two coordinate (x- and y-) directions. Hence, two sub-controllers per particle are used - one for each direction, so that corrections to be made corresponds to the errors in their respective directions. However, the flow rate inlets are not directional i.e. the flow from one inlet does not necessarily affect the movement of the particles only in one direction. Thus, the flow rate corrections are calculated by adding the corrections from each direction. Considering inlet 1 as an example, for a given time step, these are given by:

$$
\Delta Q_{1,x} = \kappa_x \cdot Q_1, \text{ and } \Delta Q_{1,y} = \kappa_y \cdot Q_1
\tag{4.4}
$$

where $\Delta Q_{1,x}$ and $\Delta Q_{1,y}$ are the *magnitudes* of flow corrections to be made to inlet 1 based on deviations along the x- and y-directions respectively. κ_x and κ_y are the
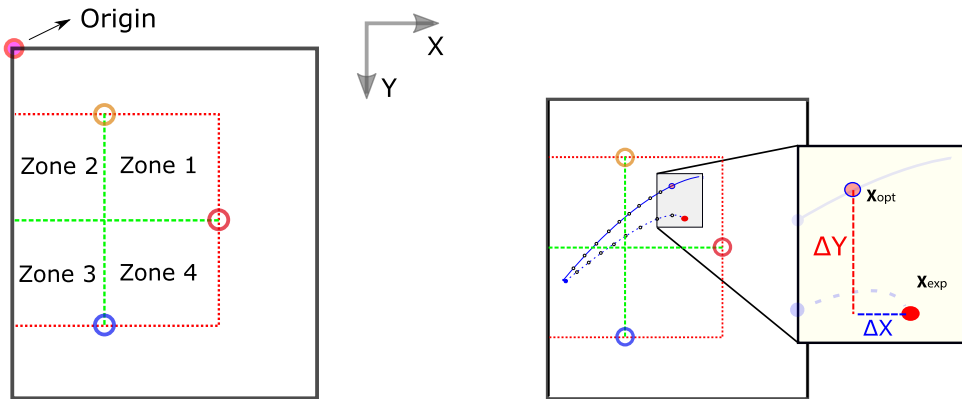
(a) Division of the cell domain into *zones* to determine the signs of flow rate corrections from the feedback controller. The green line segments are used to demarcate zones boundaries, and the red line segments represent the bounds within which the corrective feedback action is applied. The convention for the coordinate axes follows the convention of the image feed from the camera used in the experiments. The origin of the coordinate system is marked on the image. Note that the upstream inlet, responsible for the uniform flow component, is not shown in the figure above.

(b) An example illustrating the numerically determined *desired trajectory* (solid blue) and the experimentally observed *actual trajectory* (dotted blue) for a particle and the deviation between the ideal position (X_{opt}) and the actual position (X_{exp}) at a given time step denoted by the set ($\Delta X, \Delta Y$) representing deviations along the two coordinate axes.

Figure 4.5: Illustration of PID zones and deviation of a particle

correction factors calculated along the *x*- and *y*-directions respectively, and, Q_1 is the imposed flow rate value for inlet 1.

Following the same process for all inlets, the corrections from both directions are scaled to the appropriate magnitudes based on the imposed flow rates. However, note that the values calculated are only the magnitudes of correction; the signs of the corrections depend on additional factors that are discussed in Section 4.3.2.

There are important considerations for the PID controller used here. First, the flow rate correction values must be sufficiently small. In the chosen system architecture, the primary purpose of the PID controller is only to minimize deviations from the *a priori* optimized trajectory. That is, the pre-computed flow rates would yield the expected trajectory in an ideal scenario - and the PID controller is a correcting mechanism added in experiments to further decrease the error. It is unlike the use of a conventional PID controller, involving reference tracking or disturbance rejection [99]. Here, the PID controller plays an auxiliary role of keeping the deviation to a minimum. Thus, if the PID output is of a considerably high magnitude, adding it to the pre-computed flow rates may cause the *corrected* flow rates to manipulate the trajectories of the particles in an undesired manner, thereby defeating the purpose of the controller. Secondly,

CHAPTER 4

another consideration is that the system is conventionally slow (the time between two intervals is ~2 seconds), and hence the integral and derivative terms do not play as significant a role as the proportional term. That is, the error accumulation over time may not be substantial, and the system may not need a quick response from the PID controller, given that the pre-computed flow rates account for most of the particle movement. Thus, K_i and K_d have low magnitudes.

4.3.2 CELL DOMAIN PARTITIONING

The magnitude of the corrections made to the imposed flow rate values at a given time step are calculated based on a standard PID controller equation as illustrated in equation 4.1. However, this equation is not sufficient to determine whether the corrections for the individual inlets should be additive or subtractive. It is because the direction of the flow from the inlet at a given time step is determined using offline optimization routines (i.e. *a priori* particle manipulation algorithm), which takes into account the superposition of flow rates from all the inlets. Hence, during the experiment, particles can get influenced by sudden variations in the flow rate of an individual inlet, particle density or particle position along the channel height. This necessitates using the spatial information of the particles during the experiments to determine whether to add or subtract the corrections, viz. the current position of the particle in the domain of the cell and the sign of the positional error in that direction based on a pre-determined convention.

To illustrate this, configuration represented in Fig. 4.5b is considered. At a given time step, the particle ideally needs to be at position $\mathbf{X}_{opt}$ but is experimentally observed to be at position $\mathbf{X}_{exp}$. Based on a physical understanding of the system, to reduce the deviation values ΔX and ΔY:

- inlets 1 (in blue) and 3 (in yellow) need to have an additive *inward* flow to *pull* the particle towards its ideal position along the *x*-direction. Accordingly, inlet 2 (in red) needs an additive *outward* flow to *push* the particle.

- the upstream inlet (not shown in the figure) responsible for the uniform flow needs an inward flow correction to reduce uniform flow in the *x*-direction.

- inlets 1 and 2 need to provide an outward flow rate correction, and inlet 3 needs to provide an inward flow rate correction to reduce the deviation in the *y*-direction.

This information is used to determine the signs of the flow corrections. The same sign convention is used previously in the description of the experimental setup: outward flow corrections carry a positive sign, and inward flow corrections carry a negative sign.

This example illustrates how the flow rates can be adjusted based on the positional error of the particle. The direction of corrections throughout the region of interest is determined according to the physical understanding of the effect of

inflow and outflow from the inlets on the particle. It is based on the possible combinations of particle location and signs of positional errors. The flow cell is virtually partitioned into *zones* delineated by the inlet locations as illustrated in Fig. 4.5a. For each of these zones, the signs of the corrections for each inlet are determined through rules based on the signs of the positional errors. These rules are created according to the effect of flow directions from the various inlets. This information is used to construct lookup tables (one for each direction) as shown in Table 4.1. The final corrections to be applied to the individual flow rates are calculated by taking the sum of the corrections determined for each particle positional errors along each of the two coordinate axes.

Mathematically, the correction for inlet j for one particle at a given time step can be stated as:

$$\Delta Q_j = (d_{j,x})\Delta Q_{j,x} + (d_{j,y})\Delta Q_{j,y} \qquad (4.5)$$

where ΔQ_j is the final correction value to be added to the pre-computed rate for inlets j. $(d_{j,x})$ and $(d_{j,y})$ are the signs of the corrections for the x- and y-directions respectively, obtained from Table 4.1. $\Delta Q_{j,x}$ and $\Delta Q_{j,y}$ are the flow correction magnitudes for the x- and y-directions respectively for inlet j (given by equation 4.4).

It is noteworthy that the flow corrections provided by the x- and y-direction controllers for a given inlet may have opposing signs, depending on the location of the particles and the signs of their positional errors. To illustrate this point, consider the case shown in Fig. 4.5b - the particle is in *Zone 1* - and both ΔX and ΔY are positive quantities. The x- and y-direction controllers provide different signs ($d_{1,x}$ and $d_{1,y}$) based on the controller lookup tables. Hence, following equation 4.5, the final ΔQ_1 value can be a positive or a negative quantity depending on the magnitudes of the corrections $\Delta Q_{1,x}$ and $\Delta Q_{1,y}$. It can thus be seen that the nature of the flow corrections heavily depends on conditions determined by the spatial arrangement of the inlets and positional errors.

4.3.3 MOBILITY OF PARTICLES

From experiments with multiple particles, it is observed that all particles have different mobility and move at different speeds for the same uniform flow rate. It could be because of differences in their relative position along the channel height or differences in their particle density [100]. Thus, we assign a weights to each particle, and adjust the controller outputs accordingly. This step is purely motivated by our experimental observations. The particle weights are determined based on the relative mobility of the particles, observed through their response to the uniform flow.

CHAPTER 4

ΔX sign	Zone	$d_{1,x}$	$d_{2,x}$	$d_{3,x}$	$d_{\text{uniform},x}$
+	1 or 4	+	-	+	+
+	2 or 3	-	-	-	+
-	1 or 4	-	+	-	-
-	2 or 3	+	+	+	-

ΔY sign	Zone	$d_{1,y}$	$d_{2,y}$	$d_{3,y}$
+	3 or 4	-	+	+
+	1 or 2	-	-	+
-	3 or 4	+	-	-
-	1 or 2	+	+	-

(a) Determining the signs for the flow corrections based on the deviation in the x-direction. $d_{j,x}$ = sign of correction for the inlet j. Note that all four inlets are influenced by deviations in the x-direction.

(b) Determining the signs for the flow corrections based on the deviation in the y-direction. $d_{j,y}$ = sign of correction for the inlet j. Note that the y-direction controller has no influence on the uniform flow component (given by $d_{\text{uniform},x}$ in Table 4.1a) - thus, $d_{\text{uniform},y} = 0$.

Table 4.1: Lookup tables for determining the signs of the flow corrections based on the current position (zone) and direction of deviation ($\Delta X, \Delta Y$) of a particle. These tables are constructed based on a physical understanding of the effect of inward or outward flows from the inlets on the movement of the particles in the cell domain - and accordingly, how increasing or decreasing flow rates would affect the trajectories of particles depending on the situation.

After considering all factors, the final flow correction at a given time step k for inlet 1 is given by the following equation:

$$\Delta Q_{1,k} = \sum_{i=1}^{N} \Gamma_i \cdot \Delta Q_{1,k,i} \tag{4.6}$$

where N is the number of particles. $\Delta Q_{1,k}$ is the final value to be added to the imposed flow rate value for inlet 1 at time step k. $\Gamma_i = W_i/(\sum_{j=1}^{N} W_j)$ is the normalized weight of particle i, W_i being the user-assigned *weight*. $\Delta Q_{1,k,i}$ is the correction for flow inlet 1 at time step k based on particle i's positional errors - this is calculated using equation 4.5.

The input to be provided to inlet 1 at a given time step is thus:

$$Q_{f,1,k} = Q_{1,k} + \Delta Q_{1,k} \tag{4.7}$$

where for time step k, $Q_{f,1,k}$ is the final flow rate through inlet 1, $Q_{1,k}$ is the imposed flow rate at inlet 1, and $\Delta Q_{1,k}$ the correction calculated following equation 4.6.

This process is repeated for all the inlets, thus yielding the final flow rates to be provided as input. In its implementation, the process is performed using vectors, as illustrated in Fig. 4.4. In summary, the flow corrections at a given time step in the experiment are eventually determined, considering the particle mobility differences and the deviation values in each direction. Hence, each particle can be manipulated to travel along its desired trajectory.
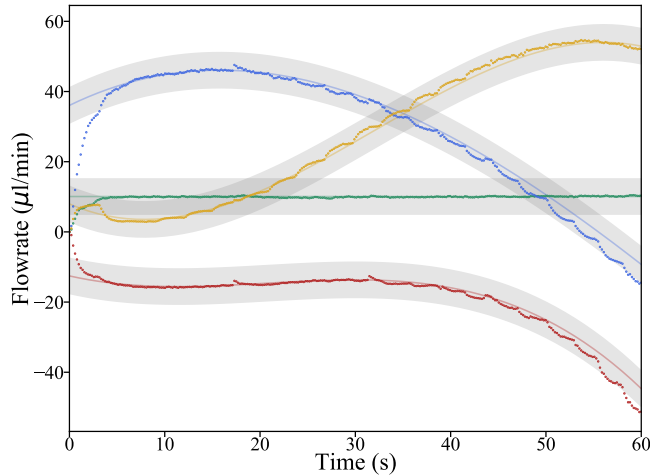
Figure 4.6: Flow rate as a function of time for uniform flow inlet (●), inlet 1 (●), inlet 2 (●) and inlet 3 (●). The desired output are marked as solid lines. The experiment data output is shown as dotted lines. The amplitude of random noise considered in the PID controller is shown as a error band (marked as gray area).

4.3.4 CONTROLLER TUNING

In any process that is controlled using a feedback controller, being able to control the value of a process output with desired specifications requires to tune. Hence, the parameters have to be appropriate values in order to ensure that the output specifications are met. For PID controllers, tuning involves setting the gain values K_p, K_i, and K_d appropriately. In this case, adding a PID controller in the loop would not necessarily lead to a better result (i.e. reduced positional errors) if the controller is not tuned.

The flow cell system needs to be controlled with the same controller gain values (K_p, K_i, K_d) for all test cases. Thus, the controller cannot be tuned using conventional techniques available in the literature [101–104] in which the process model is approximately known. The controller gain values are therefore calculated using alternative means.

A nonlinear optimization routine is used to determine the neighborhood of the controller gain values, as illustrated through a flowchart in Fig. 4.7. An appropriately-sized vector of random noise is added to the pre-computed flow rates to simulate the presence of uncertainties in the experimental setup (See Fig. 4.6). Accordingly, the resulting trajectories may deviate from the *a priori* optimized trajectories when a feedback controller is not present, as illustrated in Fig. 4.5b.
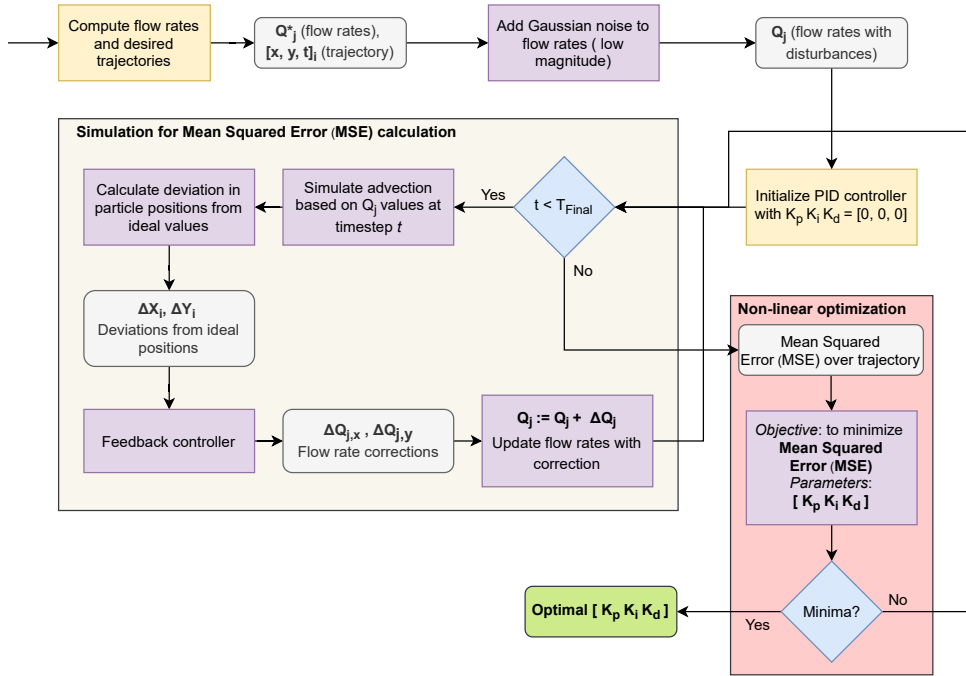
Figure 4.7: High-level flowchart illustrating how optimal PID controller parameters are computed using a non-linear optimization approach. The random noise added to the pre-computed flow rates is limited to a maximum of 5 μl/min. Additionally, the controller gain values (K_p, K_i, K_d) are also direction-specific (for instance, K_{p_x} and K_{p_y}) but this is omitted in the diagram for simplicity.

A figure of merit for quantifying the controller response is the mean squared error (MSE) of the deviation of the particles from their desired trajectories - lower values indicating better corrective action from the controller. For a given particle, the MSE is calculated as:

$$MSE = \frac{1}{T} \sum_{t=1}^{T} \left[(X_{op}(t) - X_u(t))^2 + (Y_{op}(t) - X_u(t))^2 \right] \qquad (4.8)$$

where $X_{op}(t)$ and $Y_{op}(t)$ represents the optimized (a priori) x- and y-coordinate of the particle at time step t respectively. $X_u(t)$ and $Y_u(t)$ represent the x- and y-coordinate with uncertainty at time step t respectively. T is the total number of time steps over which the MSE value is calculated.

A nonlinear optimization problem is thus formulated. The controller gains are initialized ($K_p = 0, K_i = 0, K_d = 0$). An appropriately-sized random noise vector (with a fixed set of bounds) is added to the pre-computed flow rates to simulate experimental uncertainty and the deviation of the particles ($\Delta X_t, \Delta Y_t$) from their desired trajectories is calculated for each time step. Based on the value of this
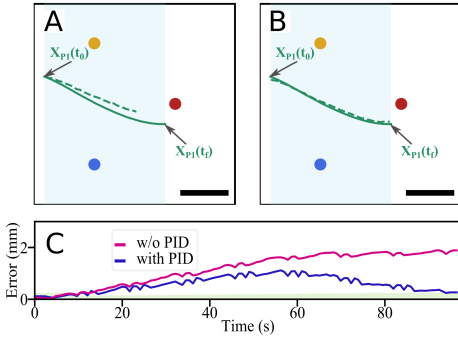
Figure 4.8: Particle trajectories showing particle deflection (——: optimized trajectory) and (▪▪▪: experimenttally measured trajectory) data for (A) without PID control and (B) with PID control. The blue shaded area is the manipulation region. The scale bar represents 4 mm. (C) Positional error as a function of time for the experiment time history. The green shaded area represents the particle mean diameter of 212 μm, which is considered as an acceptable threshold.

deviation, the locations of particles, and their weights, the controller computes the correction to be applied to the flow rates, as given by equation 4.6. The corrective action is added to the flow values, and the resulting trajectory of the particle is computed accordingly through the 4th order Runge-Kutta integration scheme for the entire run. After the final time step, the MSE for the entire run is calculated as the sum of the MSE for each particle given by equation 4.8. The objective function is to minimize the total MSE value considering the PID gain values as the parameters to optimize.

Experimental data (as shown in Fig. 4.6) suggest that the addition of random noise to pre-computed flow rates provides a realistic approximation for the variations observed in the experimentally determined flow rates. However, due to the variations between experimental runs, the *optimized* gain parameters are considered indicative values. Therefore, they need to be adjusted manually during the experiments based on observations of particle trajectories and flow rate corrections. For instance, if a particle lags considerably behind its expected trajectory after every time step, it means that the current value of K_p needs to be increased to provide a more aggressive immediate correction.

Following this procedure, $K_p, K_i,$ and K_d values are obtained in the neighbourhood of 0.5, 0.1, and 0.1 respectively. In this work, the same gain values are used for both directions (i.e. $K_{p_x} = K_{p_y}, K_{i_x} = K_{i_y}, K_{d_x} = K_{d_y}$). It is possible though, for the user to set the gains to different values in the two directions depending on direction-specific experimental conditions.

4.4 RESULTS

4.4.1 IMPORTANCE OF PID CONTROL LOOP

The performance of the PID controller is demonstrated by performing single-particle manipulations, namely particle deflection, and particle trapping. The optimized trajectory and the corresponding flow rates are computed using the *a priori* particle manipulation algorithm for the pre-defined initial $X_{P1}(t_0)$ and final

Figure 4.9: (A) Particle trajectories showing particle trapping (▬ : optimized trajectory) and (• : experimentally measured particle position) data for (A) without PID control and (B) with PID control. The blue shaded area is the manipulation region. The scale bar represents 4 mm. (C) Positional error as a function of time for the experiment time history. The green shaded area represents the particle mean diameter of 212 μm, which is consider as an acceptable threshold.
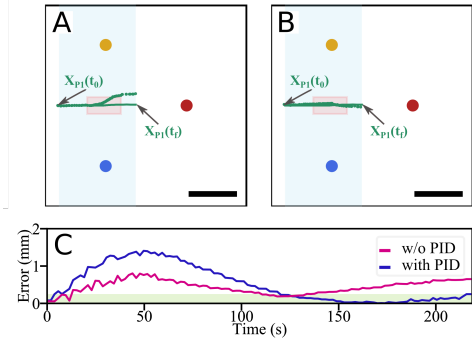
particle $X_{P1}(t_f)$ position. For the same optimized particle trajectory, the experiments are carried out with and without the PID control loop, and the results are compared based on their respective position error. The position error is calculated as the mean squared error (MSE) of the particle deviation between the experimentally determined particle trajectory and the optimized particle trajectory. A value for the MSE comparable to the particle diameter is considered as the acceptable threshold. The experimental trajectory of particle deflection without PID control is shown in Fig. 4.8A. In this case, the particle does not follow the optimized path. This may be due to the particle not being exactly at the center-line across the channel height, leading to lower particle velocity for a given flow rate. As the *a priori* particle manipulation algorithm considers particle location at the center-line across the channel, such deviations are expected. In this case, the MSE gets accumulated throughout the experiment and gives a position error of 2 mm at the end of the manipulation time. Following this first experiment, the same particle was brought back to the same initial particle position $X_{P1}(t_0)$. The experiment was then repeated using the PID controller, where the flow rate corrections are calculated in real-time to correct for the particle position error (Fig. 4.8B). During the experiment, the position error increases and then gradually decreases to below the acceptable threshold level based on the flow rate corrections, see Fig. 4.8C.

Similarly, an experiment with single-particle trapping without PID control is performed. In this case, the particle does not get trapped (see Fig. 4.9A) because the stagnation point is inherently unstable, and here the particle tends to follow a streamline near the stagnation point and ends up in different locations. Thus, the particle moves towards inlet 3 (yellow) as it moves downstream, as shown in Fig. 4.9A. Without the PID controller, the position error first increases and decreases for a short duration because the particle lags in the flow. Then, as the particle comes to the trap location, the error first decreases, before increasing again as the particle does not get trapped. The PID controller can significantly reduce the inconsistent effect of the stagnation point by correcting the flow rates while keeping the particle stationary, as demonstrated in Fig. 4.9B. With the PID controller, although the position error is prominent at the start of the manipulation,
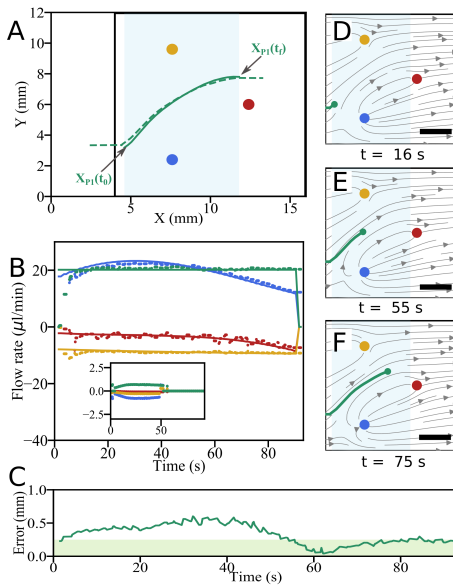
Figure 4.10: (A) Particle trajectory showing particle deflection for ▬: optimized particle trajectory and ▬▬▬: experimentally measured particle trajectory. $X_{P1}(t_0)$ and $X_{P1}(t_f)$ denotes pre-defined initial and final particle location for particle 1 respectively. The black square box marks the measurement domain. The blue shaded area indicates the region where manipulation took place. (B) Imposed and experimentally measured flow rates. (Inset) Flow rate corrections by PID controller during the experiment to minimize the particle positional error. (C) Positional error as a function of time. The green shaded area represents the mean particle diameter, 212 μm, which is considered an acceptable threshold. The particle tracks are computed from the streamlines. The streamlines are computed from the flow rates recorded during the experiment at different time instants: (D) t = 16 s (E) t = 55 s and (F) t = 75 s. The scale bar represents 4 mm.

the PID controller helps lower the position error by giving additional flow rates correction. Thus, forcing the particle to follow the *a priori* optimized trajectory.

4.4.2 SINGLE PARTICLE DEFLECTION

[Fig. 4.10D]. The experiment here is similar to the open-loop single-particle deflection discussed in section 3.5.1. Here, a constant flow, **u** = (80,0) μm/s ($Q_{\text{uniform flow}}$ =20 μl/min) is maintained throughout the experiment. The optimized trajectory and the corresponding flow rates are computed using the *a priori* particle manipulation algorithm. The solid and dashed line indicate the optimized particle trajectory and experimentally measured particle trajectory, respectively, as shown in Fig. 4.10A. The PID controller makes additive corrections to the pre-computed flow rates to minimize the particle deviation from the optimized particle trajectory. The flow rate corrections shown in the inset of Fig. 4.10B are based on the particle position error. With small flow rate corrections, a good agreement between the optimized and the experimental particle trajectory is observed. The particle position error is initially larger than the acceptable error threshold but gradually decreases as shown in Fig. 4.10C. The acceptable threshold here is the mean diameter of the particle to be manipulated *i.e.* 212 μm. Next, the flow patterns are analyzed using the experimentally measured flow rates. This provides insight into the streamlines during the manipulation event. Here, the streamlines are plotted for the manipulation at the time, t=16 s, 55 s, and 75 s

Movie 4.1

Movie 4.2

Figure 4.11: (A) Particle trajectories showing particle trapping for ▬: optimized particle trajectory and •: experimentally measured particle trajectory. $X_{P1}(t_0)$ and $X_{P1}(t_f)$ denotes pre-defined initial and final particle location for particle 1 respectively. The black square box marks the measurement domain. The blue shaded area indicates the manipulation region. The red shaded area shows the particle trapping location. (B) Imposed and experimentally measured flow rates. (Inset) Flow rate corrections by PID controller to minimize the particle's positional error. (C) Positional error as a function of time. The green shaded area represents the mean particle diameter, 212 μm, considered as the acceptable threshold. The streamlines are computed from the flow rates recorded during the experiment at different time instants: (C) t= 100 s (D) t= 150 s and (E) t= 200 s. The scale bar represents 4 mm.
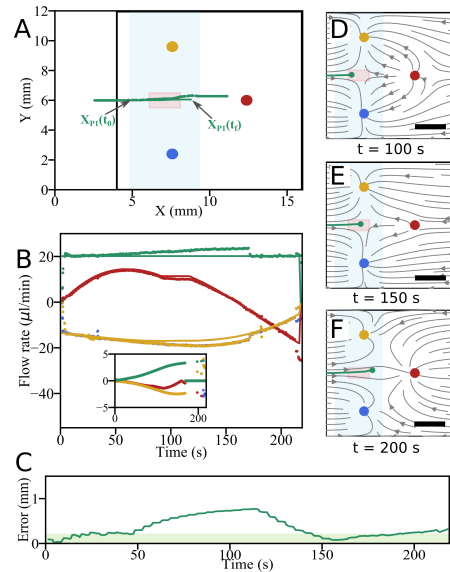
corresponding to Fig. 4.10D, E, and F, respectively. Throughout the manipulation event, the streamline pattern does not change significantly. The particle starts from $X_{P1}(t_0)$ and move towards inlet 3 as the inlet 1 has a large source strength. The particle continues to move towards inlet 3 as inlets 2 and 3 continue to act as sinks, while the source strength of inlet 1 decreases [Fig. 4.10E]. Finally, the particle begins to move straight in the downstream towards the final particle location $X_{P1}(t_f)$ [Fig. 4.10F]. See **Movie 4.1** and **Movie 4.2** for the experimental video for the single-particle deflection and the corresponding streamline visualization respectively.

4.4.3 SINGLE PARTICLE TRAPPING

Similar to the open-loop single particle trapping discussed in section 3.5.2, here, a single particle trapping is demonstrated in a closed-loop. The scatter points in Fig. 4.11A indicate the experimentally measured particle position, which shows that the particle significantly slows down and eventually gets trapped in the trapping area (red-shaded region). During the experiment, as the particle positional error increases between t = 0 s to 120 s [Fig. 4.11C], the flow rate corrections reduce the error [Fig. 4.11B (inset)]. The flow rate corrections modulate the pre-computed flow rate components such that the error is again within the threshold. Next, the streamlines are analyzed using the flow rates measured experimentally at the time, t= 100 s, 150 s, and 200 s corresponding to Figs. 4.11D,
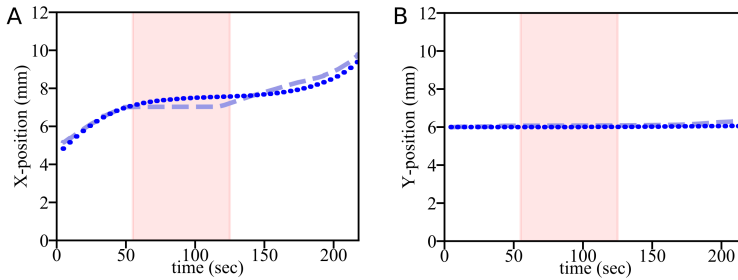
Figure 4.12: The dashed lines shows optimized particle trajectory and dotted line shows experimentally measured position for a particle that is trapped and released. The red shaded region shows the pre-defined particle trap duration. (A) Particle displacement in *x*-direction as a function of time. (B) Particle displacement in *y*-direction as a function of time.

E, and F, respectively. The particle starts to slow down as inlets 1 and 3 act as sinks, and inlet 2 acts as a source [Fig. 4.11D] until the particle becomes trapped at the stagnation point. As the stagnation point is inherently unstable, the flow rates are adjusted to maintain the particle trapped in a position by giving small corrections to the flow rates [Fig. 4.11E]. Eventually, the particle resumes the downstream motion after the trapping time has passed [Fig. 4.11F]. See **Movie 4.3** and **Movie 4.4** for the experimental video for the single-particle trapping and the corresponding streamline visualization respectively.

In the trapping duration of 60 seconds, in Fig. 4.12A, the experimentally determined particle position translates in *x*-direction by 390 μm between t= 50 s to 78 s. From t= 78 s to 110 s, the particle is stagnant at the *x*-position of 6.40 mm. Throughout the experiment in the *y*-direction, experimentally measured particle position had no significant deviation compared to the optimized particle trajectory, see Fig. 4.12B.

4.4.4 SEPARATING PARTICLE PAIR

We now focus on separating a particle pair similar to the manipulation discussed in section 3.5.3. Based on the pre-defined final position, $X_{P1}(t_f)$ and $X_{P2}(t_f)$ for particles 1 and 2 respectively and their potential start point, $X_{P1}(t_0)$ and $X_{P2}(t_0)$, where the particle pair would enter the square domain, optimized particle trajectories are computed using *a priori* particle manipulation algorithm. The optimized particle trajectories (solid green and red lines) and experimentally measured particle trajectories (dashed green and red lines) are indicated in Fig. 4.13A. During the experiment, the feedback loop system computes the experimentally measured particle positional errors for the optimized trajectories and provides flow rate corrections accordingly. A good agreement between the imposed and the experimentally measured flow rates is shown in Fig.4.13B.

CHAPTER 4

Movie 4.3

Movie 4.4

Figure 4.13: Separating particle pair: (A) Particle trajectories showing particle separation for optimized particle trajectories (━━: particle 1, ━━: particle 2) and experimentally measured (▪▪▪: particle 1, ▪▪▪: particle 2) data. $X_{P1}(t_0)$ and $X_{P1}(t_f)$ denotes pre-defined initial and final particle location for particle 1 respectively. Similarly, $X_{P2}(t_0)$ and $X_{P2}(t_f)$ are for particle 2. The measurement domain is marked by the black square box. The blue shaded area marks the manipulation region (B) Imposed and experimentally measured flow rates. (Inset) Flow rate corrections by PID controller during the experiment to minimize particles positional error. (C) Positional error as a function of time for particle 1 (━━) and particle 2 (━━). The green shaded area indicates the mean particle diameter, 212 μm, which is considered as an acceptable threshold. The streamlines are computed from the flow rates recorded during the experiment at different time instants: (D) t = 10 s (E) t = 72 s and (F) t = 104 s. The scale bar represents 4 mm.
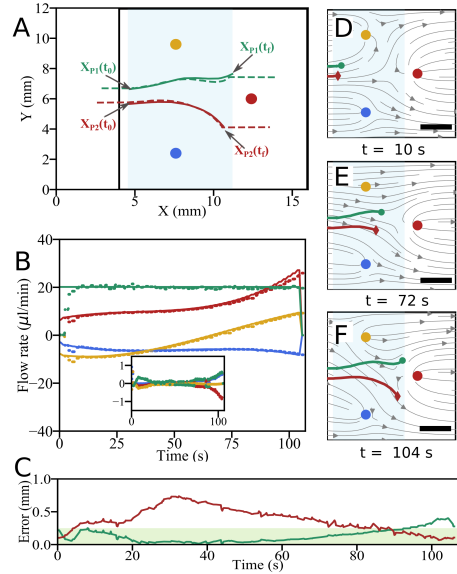
Considerably lower flow rate corrections were required in this test case [Fig.4.13B (inset)]. The particle positional error trend of particle 1 is within the threshold for the entire duration of the experiment, as shown in Fig. 4.13C. The particle positional error trend of particle 2, is outside the threshold for the majority of the manipulation duration. It might be due to the off-center particle position along the channel height. During the experiment, when the normalized weight of particle 2 is increased with respect to particle 1, the positional error trend starts to decrease for particle 2 and increase for particle 1, but stays within the threshold limit.

Furthermore, the streamline patterns are analyzed using the experimentally measured flow rates during the manipulation at the time, t= 10 s, 72 s, and 104 s corresponding to Fig. 4.13D, E, and F, respectively. The particles continue to move downstream, with particle 1 moving towards inlet 3, which acts as a sink [Fig. 4.13D]. As the particles move downstream, they separate further as a result of inlet 1 acting as a sink, and the distance between the particles increases [Fig. 4.13E]. As the particles travel towards inlet 2, the source strength of the inlet 2 increases to separate the two particles and move them closer to the pre-defined final positions [Fig. 4.13F]. See **Movie 4.5** and **Movie 4.6** for the experimental video for the separation of a particle-pair and the corresponding streamline visualization respectively.
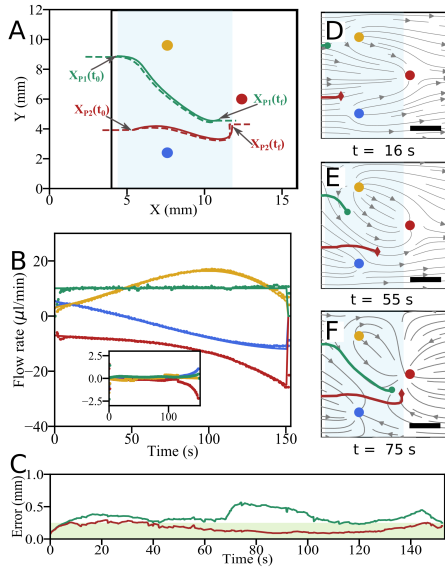
Figure 4.14: Joining two particles: (A) Particle trajectories showing particle coming close to each other for optimized particle trajectories (——: particle 1, ——: particle 2) and experimentally measured (···: particle 1, ···: particle 2) data. $X_{P1}(t_0)$ and $X_{P1}(t_f)$ denotes pre-defined initial and final particle location for particle 1 respectively. Similarly, $X_{P2}(t_0)$ and $X_{P2}(t_f)$ are for particle 2. The measurement domain is marked as the black square box. The blue shaded area indicates manipulation region. (B) Imposed and experimentally measured flow rates. (Inset) Flow rate corrections by PID controller during the experiment to minimize particle positional error. (C) Positional error as a function of time for particle 1 (——) and particle 2 (——). The green shaded area indicates the mean particle diameter, 212 μm, which is considered as an acceptable threshold. The streamlines are computed from the flow rates recorded during the experiment at different time instants: (D) t = 16 s (E) t = 55 s and (F) t = 75 s. The scale bar represents 4 mm.

4.4.5 JOINING TWO PARTICLES

Bringing two particles together in an open-loop system is discussed in section 3.5.4, here a similar experiment is demonstrated with the closed-loop control system. The *a priori* manipulation algorithm determines the optimized particle trajectories and the corresponding flow rates from the input: initial particle position ($X_{P1}(t_0)$ and $X_{P2}(t_0)$) and final particle position ($X_{P1}(t_f)$ and $X_{P2}(t_f)$) for particles 1 and 2 respectively. The optimized particle trajectories (solid green and red lines) and experimentally measured particle trajectories (dashed green and red lines) are indicated in Fig. 4.14A. A maximum of 10% deviation between the imposed and the experimentally measured flow rates is shown in Fig.4.14B. A small flow rate correction at the time t= 100 s is required [Fig.4.14B (inset)]. The particle positional error of particle 2 is within the threshold for the entire experiment. In this case, the particle position error of particle 1 remains constant until t= 70 s and increases for a short duration between t = 70 s and 75 s. During the experiment, the normalized weight of particle 1 is increased with respect to particle 2, the particle position error for particle 1 decreases to the threshold level after that [Fig. 4.14C].

Movie 4.7

Figure 4.15: Virtual mixing channel: (A) Particle trajectories showing particle mixing for optimized particle trajectories (▬ : particle 1, ▬ : particle 2) and experimentally measured (▪▪▪ : particle 1, ▪▪▪ : particle 2) data. $X_{P1}(t_0)$ and $X_{P1}(t_f)$ denotes predefined initial and final particle location for particle 1 respectively. Similarly, $X_{P2}(t_0)$ and $X_{P2}(t_f)$ are for particle 2. The black square box marks the measurement domain. The blue shaded area indicates the manipulation region. (B) Imposed and experimentally measured flow rates. (Inset) Flow rate corrections by PID controller during the experiment. (C) Positional error for particle 1 (▬) and particle 2 (▬). The green shaded area indicates the threshold, *i.e.* mean particle diameter: 212 μm. The streamlines are computed from the flow rates recorded during the experiment at different time instants: (C) t = 68 s (D) t = 100 s and (E) t = 150 s. The scale bar represents 4 mm.
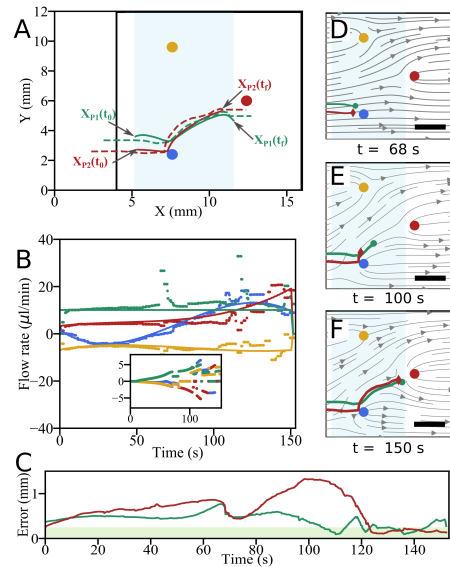
Subsequently, the streamline patterns are presented using the experimentally measured flow rates determined during the manipulation at the time, t= 16 s, 55 s, and 75 s corresponding to Fig. 4.14D, E, and F, respectively. Both the particles move downstream, and particle 1 begins to move towards inlet 1 due to inlets 1 and 2 acting as a source and sink, respectively [Fig. 4.14D]. Both particles travel downstream, with particle 1 having a larger velocity due to a strong source and sink strength from inlets 1 and 2, respectively, making a Rankine oval [Fig. 4.14E]. As the particles travel towards inlet 2, the sink strength of inlet 2 increases to move the two particles closer to each other to the pre-defined final particle position [Fig. 4.14F]. See **Movie 4.7** and **Movie 4.8** for the experimental video for the particles coming close to each other experiment and the corresponding streamline visualization respectively.

4.4.6   VIRTUAL MIXING CHANNEL

Interchanging the position of a particle pair downstream for an open-loop system is shown in section 3.5.5. In this section, the same particle manipulation is discussed in a closed-loop. The optimized particle trajectories (solid green and red lines) computed from the *a priori* particle manipulation algorithm, and experimentally measured particle trajectories (dashed green and red lines) are indicated in Fig. 4.15A. In this experiment, significant deviation arises between the imposed and the experimentally measured flow rates in the second half of the

Movie 4.8

Movie 4.9

experiment, as shown in Fig.4.15B. Here, the flow rate corrections are substantial in correcting the particle positional error [Fig.4.15B (inset)]. Since the controller gains were kept constant, the high magnitude of the flow correction may be due to a small blockage in the inlet tubes or to particle settling in the flow cell that reduces the velocity in the parabolic flow profile. This example shows that the PID control is robust in practice and can give appropriate flow rate corrections to mitigate random disturbances in the experiment. The positional error of particle 2 increases significantly, and it might be due to the settling behavior of the particle in the flow cell. The flow rate corrections decreased the particle positional error to the threshold level [Fig. 4.15C].

The streamline patterns are computed using the experimentally measured flow rates during the manipulation at the time, t= 68 s, 100 s, and 150 s corresponding to Fig. 4.15D, E, and F, respectively. In the beginning, particle 2 is in front and below particle 1. At t = 68 s, both particles are close to each other near inlet 1 [Fig. 4.15D]. Both particles are subsequently deflected towards inlet 2, and particle 2 is pushed towards inlet 3 at a steep angle such that it moves on the other side of the trajectory of particle 1 [Fig. 4.15E]. Towards the end of the manipulation period, particle 2 is behind and above particle 1 [Fig. 4.15E]. See **Movie 4.9** and **Movie 4.10** for the experimental video and the corresponding streamline visualization, respectively.

Movie 4.10

4.4.7   REAL-TIME POLLEN SELECTION AND TRAPPING

As an application of this multi-purpose flow cell, an arbitrary pollen grain is selected and trapped in the flow cell while the other pollen grains continue to flow. There has been considerable work done in pollen trapping [105, 106]. Manipulation techniques such as electric or magnetic manipulation are not feasible here. They do not create appropriate growth conditions for growing pollen tubes from a pollen grain, which promptly respond to chemical or electrical stimuli. The pollen trapping experiment is done similarly to the particle trapping experiment explained previously in section 4.4.3. The modified experimental setup for the pollen grain experiment is discussed in section 4.2. The pollen grain approaches the measurement domain from the centerline along the width of the device. The objective is to trap the pollen at the stagnation point in the trapping area (red-shaded region) as shown in Fig. 4.16A. As the pollen enters the manipulation region, significant flow rate corrections are required [Fig. 4.16B (inset)]. The magnitude of the corrections is in the same order as the pre-computed flow rates. The pollen diameter (70 μm) is significantly smaller than the channel height (350 μm). Thus, the probability of the pollen grain not being at the centerline along the channel height is significant. At the start of the experiment, the positional error is large and gradually decreases throughout the experiment to the threshold value of 70 μm *i.e.* pollen grain diameter. Fig. 4.16D, E, and F correspond to pollen grain trapping at the manipulation time of 100 s, 130 s, and 160 s, respectively, as seen with a 3x zoom lens along with the streamline imposed from the experimental

CHAPTER 4

Figure 4.16: Real-time pollen selection and trapping: (A)Particle trajectories showing pollen grain trapping for simulated (▬) and experiment (▪▪▪) data. $X_{P1}(t_0)$ and $X_{P1}(t_f)$ denotes pre-defined initial and final location for the selected pollen grain respectively. The black square box marks the measurement domain. The Blue shaded area indicates manipulation region. The red shaded area shows the particle trapping location. (B) Imposed and experimentally determined flow rate. (Inset) Flow rate corrections by PID controller to minimize the positional error. (C) Positional error as a function of time. The green shaded area represents the mean pollen diameter, 70 μm, considered as the acceptable threshold. Images of trapped pollen is shown at different time stamps during the trapping process: (C)t = 100 s (D)t = 130 s and (E)t = 160 s.The gray lines depict the streamlines around the pollen grain. The scale bar represents 250 μm.
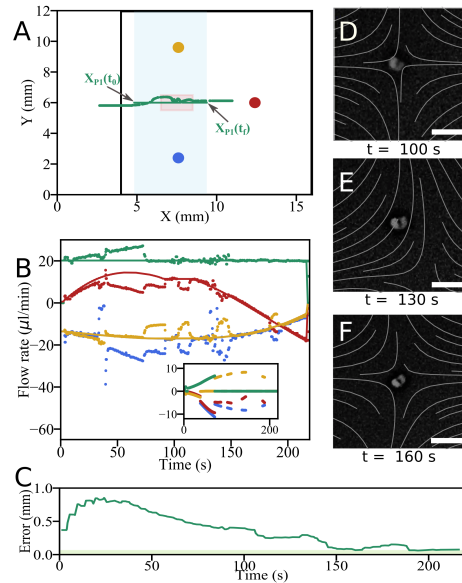
flow rate data. The streamlines vary with time to keep the pollen at the same position. See **Movie 4.11** for the pollen trapping experiment as seen by 1x lens (for pollen manipulation) and 3x zoom lens (for visualization).

4.5 DISCUSSION AND CONCLUSION

This chapter describes the PID control approach, which complements the *a priori* particle manipulation algorithm to improve the accuracy and precision of the experimental manipulation of particles using pre-computed optimized trajectories. It is essential to make this work in practice. The linear aspect of potential flow makes the control strategy straightforward and fast. The PID controller gives flow rate corrections added to the pre-computed flow rate based on the measured particle deviation from the pre-computed optimized particle trajectories in real-time during the experiment.

With the PID control strategy, the flow cell is capable of various microfluidic fundamental processes such as sorting (see Fig. 4.10), trapping (see Fig. 4.11), separating (see Fig. 4.13), joining (see Fig. 4.14) and interchanging (see Fig. 4.15). This work can be used in chemical and biological processes such as cell trapping, cell interactions, cell separations, micro-reactors, particle assembly, adhesion,

droplet coalescence, and mixing. As a potential application for the device, it was also shown that an arbitrary pollen grain in the flow cell was trapped (see Fig. 4.16), while the flow further advects the other pollen grains. Here, the pollen grain is trapped for a minute. In principle, trapping time can be extended or reduced based on the user. An advantage of using hydrodynamic forcing is that it does not influence chemical/biological samples by external forces such as electric fields or acoustic fields.

In the future, adding more ports can make the system for two-particle manipulation more redundant. In addition, having more inlets will help to have more stable streamlines. Moreover, coupling the *a priori* particle manipulation algorithm with a more robust feedback loop such as Nonlinear Model Predictive Control (NMPC) would allow better control of the particle manipulation. NMPC can be applied with a pre-determined time horizon as already the most stable optimized particle trajectories are computed from the *a priori* particle manipulation algorithm. Additionally, an adaptive feedback controller can also be formulated that selects the controller parameters from the particle locations and the pre-computed flow rates. Also, a separate optimization can be done to find the optimum location for the inlets and their configuration to facilitate optimized particle trajectories with minimum absolute flow rate and flow rate variations.

CHAPTER 4

CONCLUSIONS AND FUTURE PERSPECTIVE

This chapter summarizes the main conclusions presented in the different chapters. Each chapter is self-contained and has its respective conclusion. Moreover, possible future research and development suggestions are discussed here.

5.1 CONCLUSIONS

The main objective of this thesis is discussed in section 1.4. The aim was to build a versatile microfluidic platform for multi-purpose particle manipulation applications. This thesis demonstrates that such a device can be fabricated and can potentially be employed for diverse applications. To support this claim, multiple pivotal experiment test cases such as sorting, trapping, separating, joining and mixing are performed in the microfluidic device. The success of these test cases shows the capability of the device for various applications in the field of microfluidics. Concluding remarks from this work are discussed hereafter.

PSI-PIV

The development of the Psi-PIV algorithm was an important milestone in moving towards the main objective of this thesis. Psi-PIV overcomes the problem of correlation depth, which is substantially larger than the channel height. Thus Psi-PIV does not suffer from measurement errors and uncertainty that one would otherwise encounter. This algorithm helps determine the flow fields using the potential flow theory. In comparison to conventional PIV, a major difference lies in the fact that Psi-PIV requires a lower image density ($N_{\mathrm{eff}} = N_F N_I F_I F_\Delta$) to determine the flow direction for each interrogation window. Once the flow direction is determined, the two-dimensional stream function is used to extract and reconstruct the magnitude of the velocity field. This increases the temporal resolution that Psi-PIV can achieve compared to conventional PIV. In this thesis, Psi-PIV was used to validate the flow field pattern in the microfluidic device when comparing the data from experiments to the potential flow simulations.

PARTICLE MANIPULATION

The development of the novel *a priori* particle manipulation algorithm made great strides in making such a flow cell a reality. The optimization routine determines an optimal particle trajectory based on the pre-defined initial and final location of the particles. The optimized particle trajectory is determined while minimizing the absolute flow rates and the flow rate variations, which are crucial from the experimental point of view. Additionally, the *a priori* particle manipulation algorithm is adaptable and easy to scale up or down to suit the physical dimensions of the microfluidic device. It is possible since the entire optimization calculations are performed on non-dimensional terms that are scaled by the length scale of the region of interest, channel height, and the uniform flow velocity. The experimental results in chapter 3 showed that the *a priori* particle manipulation algorithm can construct stable pre-computed flow rates that the pump can deliver. Thus, it maximizes the probability of the particle following the desired optimal particle trajectory in an experiment despite measurement noise. However, the robustness of the *a priori* particle manipulation algorithm is currently limited as it does not consider certain effects, which can unpredictably alter the particle trajectory, such as surface roughness, particle density, and off-center particle position along the channel height. This would lead to error in the particle trajectory that will accumulate over time, leading to an increasing deviation of the particle from the desired trajectory.

PARTICLE MANIPULATION WITH A FEEDBACK LOOP

To increase the reliability of the experiments in the flow cell, real-world aspects such as flow cell surface roughness, small deformities of the inlets due to the fabrication process, and off-center particle position in the channel need to be addressed. To address these issues, we develop a Proportional Integral Derivative (PID) controller, which complements the *a priori* particle manipulation algorithm to improve the robustness, accuracy and precision of our particle manipulation approach. The linearity of the potential flow theory makes the control strategy straightforward and fast. The PID controller produces flow rate corrections for the pre-computed flow rates based on the particle deviation from their prescribed path during the real-time experiment. The experiments demonstrated that with the *a priori* particle manipulation algorithm and PID control strategy, the flow cell performs various microfluidic fundamental processes such as sorting, trapping, separating, joining, and mixing. As an application for the device as a trapping device, an arbitrary pollen grain is selected in the flow cell and trapped while the other pollen grains continue to flow. An advantage of using hydrodynamic forcing is that it allows identical growth conditions for the chemical/biological specimens compared to external forces such as electric fields or acoustic fields.

CHAPTER 5

Thus, this microfluidic device can be used in chemical and biological processes such as cell trapping, cell interactions, cell separations, micro-reactors, particle assembly, adhesion, droplet coalescence, and mixing.

5.2 FUTURE PERSPECTIVES

Considering the challenges experienced in this work, the following recommendations are formulated for future work.

PSI-PIV

The minimum image density required to determine the direction field could be further improved with the use of advanced PIV processing steps such as multi-grid and iterative windows approach ([89]). Psi-PIV can be modified to determine velocity field from the concentration measurements in a Hele-Shaw cell which is relevant for studies related Rayleigh-Benard convection of carbon dioxide dissolving into brine [107]. In such a method, in-plane velocity ratio *(u/v)* at every *x*-, *y*-coordinate pair can be determined from the directional correlation as discussed in Chapter 2. The concentration map of carbon dioxide can be captured using fluorescent emission of a pH-sensitive dye. The information from the concertation map and the vector angle (Θ) from Psi-PIV can be combined and coupled with the advection-diffusion equation ([90]) to determine the velocity from the concentration as shown below:

$$u = v \cdot \tan \theta \tag{5.1}$$

$$v = \frac{D \cdot \left(\frac{\partial^2 C}{\partial x^2} + \frac{\partial^2 C}{\partial y^2} \right) - \frac{\partial C}{\partial t}}{\tan \Theta \cdot \frac{\partial C}{\partial x} + \frac{\partial C}{\partial y}} \tag{5.2}$$

where u and v are velocity component in *x*- and *y*- direction respectively. C is concentration and D is diffussion coefficient.

PARTICLE MANIPULATION

The *a priori* particle manipulation algorithm is a two-step optimization that uses the solutions of Legendre polynomials to predict the flow rates. A combination of the orthogonal polynomials for the unconstrained and constrained algorithms can be explored to deliver lower absolute flow rates values and lesser flow rate variations. As the flow rate is calculated using potential flow theory, the flow control mechanism will work for all the Newtonian fluids as long as the Hele-Shaw approximation is valid. As the *a priori* particle manipulation algorithm is based on the framework of superposition of sources and sinks in a potential flow field, the same framework can be modified to be used with electric and magnetic

CHAPTER 5

forces as well. It is possible because even these forces can be described as a superposition of sources and sinks.

Combining hydrodynamic forcing with acoustic/magnetic/electric fields or optical tweezers can make the flow cell more versatile. The microfluidic device can be made smaller, making it more interesting for biological applications such as cell trapping. Fabricating the device with different materials such as glass can reduce the flow cell surface roughness. The effects of microbubbles or air obstruction in the channel can be reduced with hydrophilic coating. Also, adding more inlets would make the system more redundant for two-particle manipulation. Having more inlets will help to establish more stable streamlines. Moreover, a separate optimization can be done to find the optimum location of the inlets and configuration to facilitate the desired particle trajectories.

PARTICLE MANIPULATION WITH A FEEDBACK LOOP

In the existing PID setup, the corrections for the individual inlets depend only on the zone and particle deviation values. This can be further extended by using "weighting functions" to determine relative weights for individual flow rate corrections based on the distance of the particles from the inlets. Additionally, to prevent possible oscillatory behavior at zone boundaries, "dead zones" can be demarcated within which no control action should be applied to the flow rates. Furthermore, coupling our *a priori* particle manipulation algorithm with more optimal approaches such as Nonlinear Model Predictive Control (NMPC) [108] may allow better control of the particle manipulation. NMPC can be used to break the optimized trajectory from the *a priori* particle manipulation algorithm into multiple optimization problems over a finite period of time. Here, the model is a system whose output consists of particle trajectories over the finite period of time (horizon) in the control domain. The set of input is the flow rates to be imposed. The optimized particle trajectories and flow rates for the horizon can be computed using the *a priori* manipulation algorithm considering the deviated particle positions as the new initial positions. This process is computationally more expensive but provides optimal flow rate values based on particle deviations from the pre-defined particle trajectory. Additionally, an adaptive feedback controller can also be formulated that selects the controller parameters from the particle locations and the pre-determined flow rates.

REFERENCES

[1] S. Hassan and Y. S. Zhang, *Chapter 10 - Microfluidic technologies for local drug delivery*, ser. Micro and Nano Technologies. William Andrew Publishing, (2019), pp. 281–305. DOI: https://doi.org/10.1016/B978-0-12-812659-2.00010-7.

[2] S. A. Khan, A. Günther, M. A. Schmidt, and K. F. Jensen, Microfluidic synthesis of colloidal silica, *Langmuir*, **20**, no. 20, pp. 8604–8611, (2004). DOI: 10.1021/la0499012.

[3] K. W. Bong, D. C. Pregibon, and P. S. Doyle, Lock release lithography for 3d and composite microparticles, *Lab Chip*, **9**, no. 7, pp. 863–866, (2009). DOI: 10.1039/B821930C.

[4] L. CC, S. TM, and Q. SR, A microfluidic oligonucleotide synthesizer, *Nucleic Acids Res.*, **38**, no. 8, pp. 2514–2521, (2010).

[5] Y. Cui, F. M. Hameed, B. Yang, K. Lee, C. Q. Pan, S. Park, and M. Sheetz, Cyclic stretching of soft substrates induces spreading and growth, *Nat. Commun.*, **6**, no. 1, p. 6333, (2015).

[6] D. R. Gossett, H. T. K. Tse, S. A. Lee, Y. Ying, A. G. Lindgren, O. O. Yang, J. Rao, A. T. Clark, and D. Di Carlo, Hydrodynamic stretching of single cells for large population mechanical phenotyping, *PNAS*, **109**, no. 20, pp. 7630–7635, (2012). DOI: 10.1073/pnas.1200107109.

[7] J. Dai, S. H. Yoon, H. Y. Sim, Y. S. Yang, T. K. Oh, J. F. Kim, and J. W. Hong, Charting microbial phenotypes in multiplex nanoliter batch bioreactors, *Anal. Chem.*, **85**, no. 12, pp. 5892–5899, (2013).

[8] M. Mehling, T. Frank, C. Albayrak, and S. Tay, Real-time tracking, retrieval and gene expression analysis of migrating human T cells, *Lab Chip*, **15**, no. 5, pp. 1276–1283, (2015). DOI: 10.1039/C4LC01038H.

[9] A. M. Skelley, O. Kirak, H. Suh, R. Jaenisch, and J. Voldman, Microfluidic control of cell pairing and fusion, *Anal. Chem.*, **6**, no. 2, pp. 147–152, (2009). DOI: 10.1038/nmeth.1290.

[10] C. Zheng, L. Zhao, G. Chen, Y. Zhou, Y. Pang, and Y. Huang, Quantitative study of the dynamic tumor–endothelial cell interactions through an integrated microfluidic coculture system, *Anal. Chem.*, **84**, no. 4, pp. 2088–2093, (2012). DOI: 10.1021/ac2032029.

[11] H. W. Hou, M. E. Warkiani, B. L. Khoo, Z. R. Li, R. A. Soo, D. S.-W. Tan, W.-T. Lim, J. Han, A. A. S. Bhagat, and C. T. Lim, Isolation and retrieval of circulating tumor cells using centrifugal forces, *Sci. Rep.*, **3**, no. 1, p. 1259, (2013). DOI: 10.1038/srep01259.

[12] Y. Yang, H. S. Rho, M. Stevens, A. G. J. Tibbe, H. Gardeniers, and L. W. M. M. Terstappen, Microfluidic device for dna amplification of single cancer cells isolated from whole blood by self-seeding microwells, *Lab Chip*, **15**, no. 22, pp. 4331–4337, (2015). DOI: 10.1039/C5LC00816F.

[13] T. Krebs, C. P. G. H. Schroen, and R. M. Boom, A microfluidic study of oil-water separation kinetics, *Adv. Fluid Mech*, **74**, pp. 427–438, (2012). DOI: 10.2495/AFM120381.

[14] M. H. Schneider, V. J. Sieben, A. M. Kharrat, and F. Mostowfi, Measurement of asphaltenes using optical spectroscopy on a microfluidic platform, *Anal. Chem.*, **85**, no. 10, pp. 5153–5160, (2013). DOI: 10.1021/ac400495x.

[15] R. Fisher, M. K. Shah, D. Eskin, K. Schmidt, A. Singh, S. Molla, and F. Mostowfi, Equilibrium gas–oil ratio measurements using a microfluidic technique, *Lab Chip*, **13**, no. 13, pp. 2623–2633, (2013). DOI: 10.1039/C3LC00013C.

[16] B. Morin, Y. Liu, V. Alvarado, and J. Oakey, A microfluidic flow focusing platform to screen the evolution of crude oil–brine interfacial elasticity, *Lab Chip*, **16**, no. 16, pp. 3074–3081, (2016). DOI: 10.1039/C6LC00287K.

[17] A. Karimi, S. Yazdi, and A. M. Ardekani, Hydrodynamic mechanisms of cell and particle trapping in microfluidics, *Biomicrofluidics*, **7**, no. 021501, pp. 1–23, (2013).

[18] P. Sajeesh and A. K. Sen, Particle separation and sorting in microfluidic devices: A review, *Microfluid. Nanofluidics*, **17**, no. 1, pp. 1–52, (2014).

[19] C. Wyatt Shields IV, C. D. Reyes, and G. P. López, Microfluidic cell sorting: A review of the advances in the separation of cells from debulking to rare cell isolation, *Lab Chip*, **15**, no. 5, pp. 1230–1249, (2015).

[20] A. M. Pit, M. H. G. Duits, and F. Mugele, Droplet manipulations in two phase flow microfluidics, *Micromachines*, **6**, no. 11, pp. 1768–1793, (2015).

[21] S. Zhang, Y. Wang, P. Onck, and J. den Toonder, A concise review of microfluidic particle manipulation methods, *Microfluid. Nanofluidics*, **24**, no. 4, pp. 1–20, (2020).

[22] J. McGrath, M. Jimenez, and H. Bridle, Deterministic lateral displacement for particle separation: A review, *Lab Chip*, **14**, no. 21, pp. 4139–4158, (2014). DOI: 10.1039/C4LC00939H.

[23] Z. Liu, F. Huang, J. Du, W. Shu, H. Feng, X. Xu, and Y. Chen, Rapid isolation of cancer cells using microfluidic deterministic lateral displacement structure, *Biomicrofluidics*, **7**, no. 1, p. 011801, (2013). DOI: 10.1063/1.4774308.

[24] S. H. Holm, J. P. Beech, M. P. Barrett, and J. O. Tegenfeldt, Separation of parasites from human blood using deterministic lateral displacement, *Lab Chip*, **11**, no. 7, pp. 1326–1332, (2011). DOI: 10.1039/C0LC00560F.

[25] M. Yamada, M. Nakashima, and M. Seki, Pinched flow fractionation: Continuous size separation of particles utilizing a laminar flow profile in a pinched microchannel, *Anal. Chem*, **76**, no. 18, pp. 5465–5471, (2004). DOI: 10.1021/ac049863r.

[26] J. Takagi, M. Yamada, M. Yasuda, and M. Seki, Continuous particle separation in a microchannel having asymmetrically arranged multiple branches, *Lab Chip*, **5**, no. 7, pp. 778–784, (2005). DOI: 10.1039/B501885D.

[27] Z. Wu, B. Willing, J. Bjerketorp, J. K. Jansson, and K. Hjort, Soft inertial microfluidics for high throughput separation of bacteria from human blood cells, *Lab Chip*, **9**, no. 9, pp. 1193–1199, (2009). DOI: 10.1039/B817611F.

[28] D. Di Carlo, D. Irimia, R. G. Tompkins, and M. Toner, Continuous inertial focusing, ordering, and separation of particles in microchannels, *PNAS*, **104**, no. 48, pp. 18 892–18 897, (2007). DOI: 10.1073/pnas.0704958104.

[29] S. C. Hur, H. T. K. Tse, and D. Di Carlo, Sheathless inertial cell ordering for extreme throughput flow cytometry, *Lab Chip*, **10**, no. 3, pp. 274–280, (2010). DOI: 10.1039/B919495A.

[30] Y. Zhang and N.-T. Nguyen, Magnetic digital microfluidics – a review, *Lab Chip*, **17**, no. 6, pp. 994–1008, (2017). DOI: 10.1039/C7LC00025A.

[31] K. Hoshino, Y.-Y. Huang, N. Lane, M. Huebschman, J. W. Uhr, E. P. Frenkel, and X. Zhang, Microchip-based immunomagnetic detection of circulating tumor cells, *Lab Chip*, **11**, no. 20, pp. 3449–3457, (2011). DOI: 10.1039/C1LC20270G.

[32] J. H. Kang, S. Krause, H. Tobin, A. Mammoto, M. Kanapathipillai, and D. E. Ingber, A combined micromagnetic-microfluidic device for rapid capture and culture of rare circulating tumor cells, *Lab Chip*, **12**, no. 12, pp. 2175–2181, (2012). DOI: 10.1039/C2LC40072C.

[33] X. Xuan, Recent advances in direct current electrokinetic manipulation of particles for microfluidic applications, *Electrophoresis*, **40**, no. 18-19, pp. 2484–2513, DOI: https://doi.org/10.1002/elps.201900048.

[34] M. Muniruzzaman, C. M. Haberer, P. Grathwohl, and M. Rolle, Multicomponent ionic dispersion during transport of electrolytes in heterogeneous porous media: Experiments and model-based interpretation, *GCA*, **141**, pp. 656–669, (2014). DOI: https://doi.org/10.1016/j.gca.2014.06.020.

[35] P. Y. Lee, J. Costumbrado, C.-Y. Hsu, and Y. H. Kim, Agarose gel electrophoresis for the separation of dna fragments, *JoVE*, no. 62, p. 3923, (2012). DOI: 10.3791/3923.

[36] E. B. Cummings and A. K. Singh, Dielectrophoresis in microchips containing arrays of insulating posts: Theoretical and experimental results, *Anal. Chem.*, **75**, no. 18, pp. 4724–4731, (2003). DOI: 10.1021/ac0340612.

[37] X. Hu, P. H. Bessette, J. Qian, C. D. Meinhart, P. S. Daugherty, and H. T. Soh, Marker-specific sorting of rare cells using dielectrophoresis, *PNAS*, **102**, no. 44, pp. 15 757–15 761, (2005). DOI: 10.1073/pnas.0507719102.

[38] A. Ashkin, J. M. Dziedzic, J. E. Bjorkholm, and S. Chu, Observation of a single-beam gradient force optical trap for dielectric particles, *Opt. Lett.*, **11**, no. 5, pp. 288–290, (1986). DOI: 10.1364/OL.11.000288.

[39] J. R. Moffitt, Y. R. Chemla, S. B. Smith, and C. Bustamante, Recent advances in optical tweezers, *Annu. Rev. Biochem.*, **77**, no. 1, pp. 205–228, (2008), PMID: 18307407. DOI: 10.1146/annurev.biochem.77.043007.090225.

[40] A. Kasukurti, M. Potcoava, S. Desai, C. Eggleton, and D. W. M. Marr, Single-cell isolation using a dvd optical pickup, *Opt. Express*, **19**, no. 11, pp. 10 377–10 386, (2011). DOI: 10.1364/OE.19.010377.

[41] D. Wei, P. G. Dehnavi, M.-E. Aubin-Tam, and D. Tam, Measurements of the unsteady flow field around beating cilia, *J. Fluid Mech*, **915**, A70, (2021). DOI: 10.1017/jfm.2021.149.

[42] B. Hammarström, T. Laurell, and J. Nilsson, Seed particle-enabled acoustic trapping of bacteria and nanoparticles in continuous flow systems, *Lab Chip*, **12**, no. 21, pp. 4296–4304, (2012). DOI: 10.1039/C2LC40697G.

[43] A. Nilsson, F. Petersson, H. Jönsson, and T. Laurell, Acoustic control of suspended particles in micro fluidic chips, *Lab Chip*, **4**, no. 2, pp. 131–135, (2004). DOI: 10.1039/B313493H.

[44] J. Toonder, den and P. Onck, Microfluidic manipulation with artificial/bioinspired cilia, *Trends Biotechno.*, **31**, no. 2, pp. 85–91, (2013). DOI: 10.1016/j.tibtech.2012.11.005.

[45] Z. Yang, J. K. Park, and S. Kim, Magnetically responsive elastomer–silicon hybrid surfaces for fluid and light manipulation, *Small.*, **14**, no. 2, p. 1 702 839, (2018). DOI: https://doi.org/10.1002/smll.201702839.

[46] S. Zhang, Y. Wang, P. R. Onck, and J. M. J. den Toonder, Removal of microparticles by ciliated surfaces—an experimental study, *Adv. Funct. Mater.*, **29**, no. 6, p. 1 806 434, (2019). DOI: https://doi.org/10.1002/adfm.201806434.

[47] A. T. Brimmo and M. A. Qasaimeh, Stagnation point flows in analytical chemistry and life sciences, *RSC Adv.*, **7**, no. 81, pp. 51 206–51 232, (2017).

[48] A. Deka, "Manipulation of particles in a Hele-Shaw cell using sources and sinks," Master's Thesis, TU Delft , Netherlands, (2018). DOI: http://resolver.tudelft.nl/uuid:fe2ef1cc-836a-4ad0-bbe8-c60bed1dd592.

[49] K. Bakal, "Particle manipulation using microfluidics," Master's Thesis, TU Delft , Netherlands, (2019). DOI: http://resolver.tudelft.nl/uuid:eacb9fa0-401b-4b17-97b6-f0eed6744bdf.

[50] A. Shenoy, D. Kumar, S. Hilgenfeldt, and C. M. Schroeder, Flow topology during multiplexed particle manipulation using a stokes trap, *Phys. Rev. Applied*, **12**, no. 5, p. 054 010, (2019).

[51] D. P. Taylor and G. V. Kaigala, Reconfigurable microfluidics: Real-time shaping of virtual channels through hydrodynamic forces, *Lab Chip*, **20**, no. 10, pp. 1720–1728, (2020). DOI: 10.1039/D0LC00197J.

[52] G. I. Taylor, The formation of emulsions in definable fields of flow, *Proc. Math. Phys. Eng.*, **146**, no. 858, pp. 501–523, (1934). DOI: 10.1098/rspa.1934.0169.

[53] B. J. Bentley and L. G. Leal, A computer-controlled four-roll mill for investigations of particle and drop dynamics in two-dimensional linear shear flows, *J. Fluid Mech*, **167**, pp. 219–240, (1986).

[54] M. Tanyeri, E. M. Johnson-Chavarria, and C. M. Schroeder, Hydrodynamic trap for single particles and cells, *Appl. Phys. Lett.*, **96**, no. 22, pp. 224101-1–3, (2010).

[55] T. M. Schneider, S. Mandre, and M. P. Brenner, Algorithm for a microfluidic assembly line, *Phys. Rev. Lett.*, **106**, no. 9, p. 094 503, (2011).

[56] A. Shenoy, C. V. Rao, and C. M. Schroeder, Stokes trap for multiplexed particle manipulation and assembly using fluidics, *PNAS*, **113**, pp. 3976–3981, (2016).

[57] M. Tanyeri, M. Ranka, N. Sittipolkul, and C. M. Schroeder, A microfluidic-based hydrodynamic trap: Design and implementation, *Lab Chip*, **11**, no. 10, pp. 1786–1794, (2011).

[58] M. Tanyeri and C. M. Schroeder, Manipulation and confinement of single particles using fluid flow, *Nano letters*, **13**, no. 6, pp. 2357–2364, (2013).

[59] A. Shenoy, M. Tanyeri, and C. M. Schroeder, Characterizing the performance of the hydrodynamic trap using a control-based approach, *Microfluid. Nanofluidics*, **18**, no. 5, pp. 1055–1066, (2015).

[60] C. Pozrikidis, The motion of particles in the Hele-Shaw cell, *J. Fluid Mech*, **261**, pp. 199–222, (1994).

[61] D. Kumar, A. Shenoy, S. Li, and C. M. Schroeder, Orientation control and nonlinear trajectory tracking of colloidal particles using microfluidics, *Phys. Rev. Fluids*, **4**, no. 11, p. 114 203, (2019).

[62] A. Kislaya, D. Tam, P. Veenstra, and J. Westerweel, "Particle/droplet manipulation-on-chip," *APS Division of Fluid Dynamics Meeting Abstracts*, ser. APS Meeting Abstracts, vol. 63, (2018), J06.004.

[63]   A. Kislaya, D. Tam, and J. Westerweel, "Towards virtual channels in a microfluidic device," *APS Division of Fluid Dynamics Meeting Abstracts*, ser. APS Meeting Abstracts, (2020), J06.004.

[64]   A. H. Gibson, Prof. H. S. Hele-Shaw, F.R.S, *Nature*, **147**, no. 3723, pp. 290–290, (1941). DOI: 10.1038/147290a0.

[65]   R. Lindken, M. Rossi, S. Große, and J. Westerweel, Micro-Particle Image Velocimetry (PIV): Recent developments, applications, and guidelines, *Lab Chip*, **9**, pp. 2551–67, (2009).

[66]   S. Wereley and C. Meinhart, Recent Advances in Micro-Particle Image Velocimetry, *Annual Review of Fluid Mechanics*, **42**, pp. 557–576, (2010).

[67]   R. Adrian and J. Westerweel, *Particle image velocimetry*. Cambridge University Press, (2011).

[68]   C. Meinhart, S. Wereley, and M. Gray, Volume illumination for two-dimensional particle image velocimetry, *Meas Sci Technol*, **11**, pp. 809–814, (2000).

[69]   P. Vennemann, K. K. KT, R. Lindken, B. Groenendijk, V. Stekelenburg-de, T. ten Hagen, N. Ursem, R. Poelmann, J. Westerweel, and B. Hierck, In vivo micro particle image velocimetry measurements of blood-plasma in the embryonic avian heart, *J. Biomech.*, **39**, pp. 1191–1200, (2006).

[70]   M. Olsen and R. Adrian, Out-of-focus effects on particle image visibility and correlation in microscopic particle image velocimetry, *Exp Fluids*, **29**, S166–S174, (2000).

[71]   A. Kloosterman, C. Poelma, and J. Westerweel, Flow rate estimation in large depth-of-field micro-PIV, *Exp Fluids*, **50**, pp. 1587–1599, (2011).

[72]   D. Ehyaei and K. Kiger, Quantitative velocity measurement in thin-gap Poiseuille flow, *Exp Fluids*, **55**, pp. 1–12, (2014).

[73]   F. Akbaridoust, J. Philip1, D. R. A. Hill, and I. Marusic, Simultaneous micro-PIV measurements and real-time control trapping in a cross-slot channel, *Exp Fluids*, **59**, pp. 183-1–183-17, (2018).

[74]   L. L. Green and T. D. Foster, Secondary convection in a Hele Shaw cell, *J. Fluid Mech*, **71**, pp. 675–687, (1975).

[75]   L. Sebestikova, J. D'Hernoncourt, M. J. B. Hauser, S. C. Muller, and A. D. Wit, Flow-field development during finger splitting at an exothermic chemical reaction front, *Physical Review E*, **75**, pp. 026309-1–026309-8, (2007).

[76]   C. Almarcha, P. M. J. Trevelyan, P. Grosfils, and A. D. Wit, Chemically Driven Hydrodynamic Instabilities, *Physical Review Letter*, **104**, pp. 044501-1–044501-4, (2010).

[77]   A. Vreme, F. Nadal, B. Pouligny, P. Jeandet, G. Liger-Belair, and P. Meunier, Gravitational instability due to the dissolution of carbon dioxide in a Hele-Shaw cell, *Physical Review Fluids 1*, **6**, pp. 064301-1–044501-20, (2016).

[78] S. Drost and J. Westerweel, Hele-Shaw rheometry, *J. Rheol.*, **57**, pp. 1787–1801, (2013).

[79] K.Erglis, A. Tatulcenkov, G. Kitenbergs, O. Petrichenko, F. G. Ergin, B. B. Watz, and A. Cebers, Magnetic field driven micro-convection in the Hele-Shaw cell, *J. Fluid Mech*, **714**, pp. 612–633, (2013).

[80] H. Kim, J. Lee, T.-H. Kim, and H.-Y. Kim, Spontaneous Marangoni Mixing of Miscible Liquids at a Liquid-Liquid-Air Contact Linel, *Langmuir*, **31**, pp. 8726–8731, (2015).

[81] S.-Y. Hou and H.-Y. Chu, Saffman-Taylor–like instability in a narrow gap induced by dielectric barrier discharge, *Physical Review E*, **92**, pp. 013101-1–013101-4, (2015).

[82] S. Wereley and C. Meinhart, Second-order accurate particle image velocimetry, *Exp Fluids*, **31**, pp. 258–268, (2001).

[83] M. Rossi, R. Lindken, B. P. Hierck, and J. Westerweel, Tapered microfluidic chip for the study of biochemical and mechanical response at subcellular level of endothelial cells to shear flow, *Lab Chip*, **9**, pp. 1403–1411, (2009).

[84] B. Ho and L. Leal, Inertial migration of rigid spheres in two- dimensional unidirectional flows, *J. Fluid Mech*, **65**, pp. 365–400, (1974).

[85] R. Keane and R. Adrian, Optimization of particle image velocimeters. Part 1: Double pulsed systems, *Meas Sci Technol*, **1**, pp. 1202–1215, (1990).

[86] R. Keane and R. Adrian, Theory of cross-correlation analysis of PIV images, *Appl. Sci. Res.*, **49**, pp. 191–215, (1992).

[87] J. Westerweel, On velocity gradients in PIV interrogation, *Exp Fluids*, **44**, pp. 831–842, (2008).

[88] Y. Xia and G. M. Whitesides, Replica molding with a polysiloxane mold provides this patterned microstructure, *Angew. Chem. Int. Ed.*, **37**, pp. 550–575, (1998).

[89] F. Scarano and M. Riethmuller, Advances in iterative multigrid PIV image processing, *Exp Fluids*, **29**, s51–s60, (2000).

[90] G. K. Batchelor, *An Introduction to Fluid Dynamics*, ser. Cambridge Mathematical Library. Cambridge University Press, (2000).

[91] P. K.Kundu, I. M.Cohen, and D. R.Dowling, *Fluid Mechanics*. Elsevier, (2012).

[92] J. Katz and A. Plotkin, *Low-Speed Aerodynamics*, 2nd ed., ser. Cambridge Aerospace Series. Cambridge University Press, (2001). DOI: 10.1017/CBO9780511810329.

[93] K. Ogata, *Modern Control Engineering, 5th Edition*. Pearson, (2010), pp. 161–164.

[94] C. G. Broyden, The convergence of a class of double-rank minimization algorithms 1. general considerations, *IMA J Appl Math*, **6**, no. 1, pp. 76–90, (1970). DOI: 10.1093/imamat/6.1.76.

[95]   C.-Y. Lee, C.-L. Chang, Y.-N. Wang, and L.-M. Fu, Microfluidic mixing: A review, *GCA*, **12**, no. 5, pp. 3263–3287, (2011). DOI: 10.3390/ijms12053263.

[96]   J. R. Koza, M. A. Keane, J. Yu, F. H. Bennett, and W. Mydlowec, Automatic creation of human-competitive programs and controllers by means of genetic programming, *Genet Program Evolvable Mach.*, **1**, no. 1, pp. 121–164, (2000).

[97]   B. D. Lucas and T. Kanade, "An iterative image registration technique with an application to stereo vision," *Proceedings of Imaging Understanding Workshop*, (1981), pp. 121–130.

[98]   K. Tang, K. F. Man, G. Chen, and S. Kwong, An optimal fuzzy pid controller, *IEEE Trans. Ind. Electron.*, **48**, no. 4, pp. 757–765, (2001). DOI: 10.1109/41.937407.

[99]   G. B. K, S. R. A, and R. T.K., Performance assessment of control loops involving unstable systems for set point tracking and disturbance rejection, *J Taiwan Inst Chem Eng.*, **85**, pp. 1–17, (2018). DOI: https://doi.org/10.1016/j.jtice.2018.01.024.

[100] Y. Ling, J.-M. Fullana, S. Popinet, and C. Josserand, Droplet migration in a hele–shaw cell: Effect of the lubrication film on the droplet dynamics, *Physics of Fluids*, **28**, no. 6, p. 062 001, (2016). DOI: 10.1063/1.4952398.

[101] K. Åström and T. Hägglund, *PID Controllers: Theory, Design, and Tuning*. ISA - The Instrumentation, Systems and Automation Society, (1995).

[102] S. A. Frank, "PID Design Example," *Control Theory Tutorial: Basic Concepts Illustrated by Software Examples*. Cham: Springer International Publishing, (2018), pp. 29–36. DOI: 10.1007/978-3-319-91707-8_4.

[103] K. H. Ang, G. Chong, and Y. Li, PID control system analysis, design, and technology, *IEEE Trans Control Syst Technol*, **13**, no. 4, pp. 559–576, (2005). DOI: 10.1109/TCST.2005.847331.

[104] H. Hjalmarsson, M. Gevers, S. Gunnarsson, and O. Lequin, Iterative feedback tuning: Theory and applications, *IEEE Control Syst.*, **18**, no. 4, pp. 26–41, (1998). DOI: 10.1109/37.710876.

[105] G. M, N. AS, A. CG, P. M, and G. A, Microfluidic positioning of pollen grains in lab-on-a-chip for single cell analysis, *J. Biosci. Bioeng.*, **117**, no. 4, pp. 504–11, (2014).

[106] A. S. Kashani and M. packirisamy, Efficient low shear flow-based trapping of biological entities, *Sci. Rep.*, **9**, no. 5511, pp. 1–15, (2019).

[107] M. Zhao, K. Kiger, A. Kislaya, and J. Westerweel, "Development of a velocity and concentration measurement method for CO_2 dissolution in brine within a Hele-Shaw cell," *APS Division of Fluid Dynamics Meeting Abstracts*, ser. APS Meeting Abstracts, (2019), Q11.003.

[108] L. Grüne and J. Pannek, "Nonlinear model predictive control," *Nonlinear Model Predictive Control: Theory and Algorithms*. London: Springer London, (2011), pp. 43–66. DOI: 10.1007/978-0-85729-501-9_3.

ACKNOWLEDGEMENTS

As I write the concluding sections of my thesis, I can admit with certainty that writing this thesis was an engaging, enjoyable, and enriching experience for me. Writing the acknowledgment is a reminder that this beautiful journey is coming to an end. I'll cherish the numerous highs of small achievements and remember the testing phases of trial and error throughout these four years of PhD. The experience, all over, taught me various professional and personal skills and I have seen myself evolve. Although I am the author of this thesis, it wouldn't have been possible without the contribution of and motivation provided by many people at all times.

Personally, I believe that any achievement in this world can be attributed to just three things: willingness of the individual, support of the ones who believe in the individual and resources made available to the individual by the ecosystem. In all three, I think I have been rather lucky. Choosing to do my PhD from this university ensured that my willingness was always fuelled in the right direction and I had all the necessary resources available at all times. Today, I want to thank each individual at the university, the lab, and the ever-encouraging atmosphere of this country that enables foreign nationals like me to achieve their dreams and always feel at home.

I would like to express my gratitude to my promotor, **Jerry Westerweel**. I still remember the first time I met you in the Laboratory for Aero- & HydroDynamics, and I was nearly star-struck but more determined about what I wanted to do. During my master's, I wished to do a PhD in experimental fluid mechanics and always wanted to work with you. I cannot emphasize enough that having you as a supervisor was indeed a dream-come-true. After 4 years, I can say that I had the same best experience as I had imagined. Your expertise and vision were invaluable in formulating the research questions and the methodology. You gave me the freedom to complete this work the way I thought was best, it is a luxury that not many PhD students enjoy and I am truly grateful to you for that. Your insightful feedback pushed me to sharpen my thinking and improved my work each time. That you always valued active communication and always tried to find time to answer my questions empowered me to deliver better. Your constant support and encouragement in finishing my experiments during the pandemic were a big driver in shaping the outcome of my experiments when times were tough. With multiple professional learnings from you, I have also been fortunate to learn several personal skills from you including conviction in one's capabilities and finding motivation even during the most chaotic days. Thank you, for all of it.

A big thank you to my second promotor and daily supervisor, **Daniel Tam**, whose enthusiasm for fluid mechanics and level of perfectionism is admirable. I have to admit that I used to dread our weekly meetings because after the meeting

it always felt like I could have done more than what I could produce in a week. But in retrospect, I believe that it pushed me to try a lot of different things, and in the end, the final product was worth the struggle. You taught me the most crucial aspect of research: defining the problem. With each of our interactions, I learnt something new that I could implement in my research. Thank you, Daniel.

A special thank you also goes to **Christian**, my early interactions with you during my master's thesis strengthened my inclination to do a PhD. You recognized my potential through our various interactions, which eventually helped me to get a PhD position in the Laboratory for Aero- & HydroDynamics.

I am very thankful to Shell Technology center Amsterdam, for providing funds for the research project, especially **Peter Veenstra**, who had a very clear practical application in mind for this project but at the same time was very open in pursuing different fundamental ideas which will eventually help in the future for such practical applications. This approach of yours is both liberating and enabling for all young researchers and I have definitely benefited from this. Thank you for all your support.

I would also like to thank **Prof. dr. ir. C. R. Kleijn**, **Prof. dr. ir. J. M. J. den Toonder**, **Prof. dr. ir. R.G.H. Lammertink**, **Dr. T. M. Schneider**, **Ir. P. Veenstra** for taking time out to be my doctoral defense committee members, critically evaluating my work, and approving my thesis. Your inputs are extremely valuable.

I'm extremely grateful to **Aniket** for working together on the framework of the PID controller and writing the LabView code for the feedback loop. Your help was instrumental in the closed-loop controller setup which is the backbone of the experiments reported in Chapter 4 of this thesis. I also want to thank **Antaran** and **Kalpit** whom I supervised and guided during my Ph.D and in turn learnt a lot through our discussions. I am glad that their M.Sc. research helped them to reach their goal of getting a Ph.D. themselves. I would also like to extend my deepest gratitude to **Prof. Kenneth Kiger**, who supervised and allowed me to work as a visiting researcher at the University of Maryland. Special thanks to **Mengye**, **Chang**, **Martin**, **Elaine**, **Bijoya**, **Diane**, and **Jennifer** who made me feel at home throughout my stay and showed me around the Washington D.C, and Maryland area. It was truly a culturally and intellectually enriching experience and I'll cherish it forever.

I would also like to extend my deepest gratitude to **Caroline**. Thank you for being the best secretary I've ever met. Your remarkable professionalism made the administrative work easy for all the members in the lab. Especially, for the international lab members. I already miss our fun conversations.

I'm deeply indebted to Edwin, Jasper, and Jan for their help in the experimental work. **Edwin**, for some reason all the cameras and the DAVIS software in our department are very loyal to you. I have faced trouble with the cameras multiple times but they simply work fine when you're around. It's like sorcery! **Jasper**, your precision and detailing in building test equipment always boggles my mind. I appreciate that you were always able to squeeze some time into your busy schedule to build some device ideas which I used to come up with. **Jan**, I greatly

acknowledge your help with LabVIEW for the pressure pump and high voltage electro-osmotic experiments to name a few. The thing which amazes me the most about you is your passion and enthusiasm to learn new things. I hope I can replicate the same level of excitement for learning new things throughout my career.

Thank you, **Amitosh**, **Andries**, **Angeliki**, **Arnoud**, **Bidhan**, **Bob**, **Caroline**, **Christian**, **Edwin**, **Ellert**, **Ernst Jan**, **Florian**, **Gem**, **Gerrit**, **Gosse**, **Göktürk**, **Greta**, **Guillermo**, **Haoyu Li**, **Henk**, **Jan**, **Jasper**, **John**, **Junaid**, **Koen**, **Lina**, **Luuk**, **Manu**, **Mark**, **Mathieu**, **Maurice**, **Melika**, **Özge**, **Parviz**, **Pedro**, **Ruud**, **Saad**, **Sören**, **Sudarshan**, **Swaraj**, **Tariq**, **Teng**, **Udhav**, **Willian**, **Wim-Paul**, **Wout**, **Wouter**, **Yavuz**, and **Yuk Man** for your contributions to my process of learning. I also had the privilege to share office with Greta, Henk, Ernst Jan, Wout, and Yavuz, and our post-5 p.m. catch-ups will remain memorable.

I am very thankful to **Beto**, **Bea**, **Swaraj**, **Tanmay**, **Michel**, **Shreyash**, **Amantrita**, **Robin**, **Sam**, **Toyah**, **Maria**, **Akash**, **Aditya**, **Rahul**, **Iha**, and **Antariksh** for their constant support and happy distractions to rest my mind outside of my research. Many thanks to Abhiroop for his helpful advice as a friend and a researcher in the last four years.

Being a part of the 3mE Ph.D. council member, gave me exposure to the university's way of working and an opportunity to meet so many fellow PhDs from the 3mE faculty. **Mascha**, thank you for chairing our meetings and voicing our concerns, thoughts and suggestions to the higher management of TU Delft, especially during covid times. The meetings on the first and last Thursday of every month with **Vilborg**, **Pieter**, **Bart**, **Eline**, **Zongcheng**, **Abhilash**, **Andrea**, **HongPeng**, **Alina**, **Padmaja**, and **Costanza**, were enjoyable and a nice break from the rigour of work.

This acknowledgment would not be complete without mentioning the pain-staking efforts and patience of my family. No words are adequate enough to express my indebtedness to **Papa**, **Mummy**, and **Bhaiya** for their support, blessings, and good wishes. I know Papa Mummy that it was a big decision for you to send me for a master's in the Netherlands, a big thank you to Bhaiya who convinced them that this will be good for my career. You all were very supportive of my choices. I owe this thesis to my family, who always stood by me and provided strength in pursuing this.

The year 2021 was perhaps most difficult, as they say it is darkest before dawn. Writing the dissertation while working on a full-time job was mentally and physically tiring. Working from home during the covid time was a silver lining for me (at least I tend to think this way) because without it I would have never been able to switch between writing my thesis and learning at the new job. Juggling between tasks, I found myself working most hours of the day without any breaks for six straight months. During this tough time, only a few people were around me, who saw my day-to-day struggle and gave me the strength to keep going. I express my deep sense of gratitude to **Krishti**, for her understanding, profound belief in my work, unparallel support, and patience that cannot be underestimated.

You have been my anchor throughout this journey, continuously and consistently motivating me. Even on the most difficult days, your belief in me helped me write the journal and thesis. I have learned much from you but the most important of all is that every day is a new beginning, a new chance to dream, a new chance to try and a new chance to achieve the goal. Thank you for being there.

It all seems worth the feeling of satisfaction that I'm experiencing in this moment as I wind up one of the most engaging, rewarding, transforming, challenging and the least to say, fulfilling chapter of my life. Thank you one and all for letting me chart my path and for constantly walking by my side when the destination seemed both far and unreal. My thesis ends here but the learning and discovery will continue for life and I shall always uphold my responsibility to contribute back to the world of research throughout my life.

Ankur Kislaya
Delft, April 2022

Ankur Kislaya

| 10-July-1992 | **Born in Ranchi, India** |

2008-2014	**B. E. Aeronautical Engineering**
	Dayananda Sagar College of Engineering, Bengaluru, India
	Affiliated to Visvesvaraya Technological University, Belagavi, India

| 2014-2016 | **M. Sc. Aerospace Engineering** |
| | Delft University of Technology, Delft, The Netherlands |

Thesis:	Estimation and reduction of peak-locking errors in PIV measurements
Supervisor:	Dr. Andrea Sciacchitano
Research Internship:	a-priori error estimation of Particle Image Velcoimetry measurements
Supervisor:	Dr. ir. Bart van Rooijen

| 2017-2021 | **Ph. D. Mechanical Engineering** |
| | Delft University of Technology, Delft, The Netherlands |

Thesis:	Particle Manipulation-on-chip
Promotor:	Prof. dr. ir. J. Westerweel
	Dr. Daniel S. W. Tam

| 2021 - Present | **Design Engineer, on-product Overlay Control group** |
| | ASML, Veldhoven, The Netherlands |

LIST OF PUBLICATIONS

JOURNAL PUBLICATIONS

[1] A. Kislaya, A.A. Samant, P. Veenstra, D.S.W. Tam, J. Westerweel. "Particle manipulation using programmable hydrodynamic forces." *Proceedings of the National Academy of Sciences of the United States of America (PNAS)*, *in submission*

[2] A. Junaid, R. Zwier, A. Kislaya, W. Stam, J. van Gils, B. Trietsch, J. Westerweel, A. Mashaghi, A.J. van Zonneveld, T. Hankemeier. "An integrated microvessels-on-a-chip platform for automated multi-channel perfusion and continual in situ oxygen monitoring", *to be submitted*

[3] A. Kislaya, A. Deka, P. Veenstra, D.S.W. Tam, J. Westerweel. "Psi-PIV: A novel framework to study unsteady microfluidic flows." *Experiments in Fluids*, Volume 61, Number 2, 2020 .

[4] W.J. Geelhoed, K.E.A. van der Bogt, T.C. Rothuizen, F.F.R. Damanik, J.F. Hamming, C.D. Mota, M.S. van Agen, H.C.de Boer, M.Tobón Restrepo, B. Hinz, A. Kislaya, C. Poelma, A.J. van Zonneveld, T.J. Rabelink, L. Moroni, J.I. Rotmans. "A novel method for engineering autologous non-thrombogenic in situ tissue-engineered blood vessels for arteriovenous grafting". *Biomaterials*, Volume 229, 2020.

[5] A. Kislaya and A. Sciacchitano. "Peak-locking error reduction by birefringent optical diffusers." *Measurement Science and Technology*, Volume 29, Number 2, 2018.

SELECTED CONFERENCE CONTRIBUTIONS

[1] A. Kislaya, D.S.W. Tam, J. Westerweel. "Towards virtual channels in a microfluidic device". *American Physical Society (APS-DFD)*, November 2020, Chicago, USA.

[2] A. Kislaya, D.S.W. Tam, J. Westerweel. "Particle manipulation using programmable hydrodynamic forces". *µTAS 2020 24th International Coference on Miniaturized System for Chemistry and Life Sciences*, October 2020, Palm Springs, USA.

[3] M. Zhao, K. Kiger, A. Kislaya, J. Westerweel. "Development of a velocity and concentration measurement method for CO_2 dissolution in brine within a Hele-Shaw cell". *American Physical Society (APS-DFD)*, November 2019 Seattle, USA.

[4] A. Kislaya, D.S.W. Tam, P. Veenstra, J. Westerweel. "Particle/droplet manipulation-on-chip". *American Physical Society (APS-DFD)*, November 2018, Atlanta, USA.

[5] A. Kislaya, A. Deka, P. Veenstra, D.S.W. Tam, J. Westerweel. Psi-PIV: A novel framework to study unsteady microfluidic flows. *LXLASER2018: 19th International Symposium on the Application of Laser and Imaging Techniques to Fluid Mechanics*, July 2018, Lisbon, Portugal.